GO-VIKING

Research and Innovation Action (RIA)

This project has received funding from the Euratom research and innovation programme 2021-2025 under Grant Agreement No 101059603

Start date : 2022-06-01 Duration : 48 Months

Development and implementation of fastrunning FSI methods

Authors : Dr. Alexander VAN ZUIJLEN (TUD), Alexander van Zuijlen (TU Delft), Kevin Zwijsen (NRG), Yuliia Filonova (IPP), Yaroslav Dubyk (IPP), Angel Papukchiev (GRS)

GO-VIKING - Contract Number: 101059603

Project officer: Angelgiorgio IORIZZO

Document title	Development and implementation of fastrunning FSI methods
Author(s)	Dr. Alexander VAN ZUIJLEN, Alexander van Zuijlen (TU Delft), Kevin Zwijsen (NRG), Yuliia Filonova (IPP), Yaroslav Dubyk (IPP), Angel Papukchiev (GRS)
Number of pages	86
Document type	Deliverable
Work Package	WP5
Document number	D5.1
Issued by	TUD
Date of completion	2024-10-18 11:29:47
Dissemination level	Public

Summary

For an accurate prediction of the impact of flow induced vibration in nuclear power generation, computational methodologies are necessary that can simulate the interaction between fluids and structures. Within different components of the nuclear power generation system, interaction effects like turbulence induced vibration (mostly for axial flow cases) and flow/vortex induced vibration (mostly for cross flow cases) in single rod and rod-bundle configurations occur. Simulation of such cases using direct CFD-FEM coupling approaches with high fidelity models may provide an accurate prediction, but at a prohibitive computational cost. In this work package, fast-running methods are identified that improve computational speed for such cases by reducing computational complexity. Each of the methods described in this report aims to reduce the computational complexity by simplifying a specific part of the flow induced vibration problem. Two methods target in particular the effect of turbulence and turbulence pressure fluctuations: by introducing a synthetic turbulence model, the goal is to retrieve turbulence pressure fluctuations to similar accuracy as LES/DNS but at a much lower computational cost. Two levels of simplification are investigated: 1) considers the anisotropy of the Reynolds stresses and solves a Poisson equation to reconstruct pressure fluctuations from the synthetic turbulence velocity fluctuations, 2) uses an algebraic expression to correlate pressure fluctuations directly to the synthetic turbulence velocity fluctuations. Two other approaches use the decomposition of the structure dynamics into decoupled modes to: 1) simplify the fluid-structure coupling by introducing a reduced order model of the structure directly into the CFD solver, and 2) building a linear fluid response model for a subset of modal deformation shapes to replace the CFD solver. The theoretical approach of these fast-running methods is documented, and some (initial) validation tests conducted.

Approval

Date	By
2024-10-18 11:38:36	Dr. Papukchiev ANGEL (GRS)
2024-10-18 11:41:05	Dr. Papukchiev ANGEL (GRS)

D5.1 Development of fast-running FSI methods

Version N°1
May / 2024

Alexander van Zuijlen[1], Kevin Zwijsen[2], Yuliia Filonova[3], Yaroslav Dubyk[3], Angel Papukchiev[4]

[1]Delft University of Technology, Delft, The Netherlands
[2]Nuclear research & consultancy Group (NRG), Petten, The Netherlands
[3]IPP Centre, Kiev, Ukraine
[4]Gesellschaft für Anlagen- und Reaktorsicherheit (GRS) gGmbH, Garching, Germany

Funded by
the European Union

Disclaimer

Funded by the European Union. Views and opinions expressed are however those of the author(s) only and do not necessarily reflect those of the European Union or European Atomic Energy Community. Neither the European Union nor the granting authority can be held responsible for them.

Document information

Grant Agreement / Proposal ID	101060826
Project Title	Gathering expertise On Vibration ImpaKt In Nuclear power Generation
Project Acronym	GO-VIKING
Scientific Coordinator	Angel Papukchiev, mailto:angel.papukchiev@grs.de, GRS Kevin Zwijsen, mailto: zwijsen@nrg.eu, NRG
Project starting date (duration)	1st June 2022 – 31st May 2026 (48 Months)
Related Work Package	WP5
Related Task(s)	T5.1: Fast-running FSI methods for FIV
Lead Organisation	TU Delft
Contributing Partner(s)	NRG, GRS, IPP
Due Date	30-06-2024
Submission Date	18-10-2024
Dissemination level	PU

History

Date	Version	Submitted by	Reviewed by	Comments
18-10-2024	1.0	Alexander van Zuijle	Angel Papukchiev, Kevin Zwijsen	

Table of contents

List of figures

List of tables

Abbreviations and Acronyms

Acronym	description
AniPFM	Anisotropic Pressure Fluctuation Model
CFD	Computational fluid dynamics
DES	Detached eddy simulation
DNS	Direct numerical simulation
FEM	Finite element method
FOM	Full-order model
GO-VIKING	Gathering expertise On Vibration ImpaKt In Nuclear power Generation
WP	Work package
LES	Large eddy simulation
MOR	Model order reduction
PFM	Pressure fluctuation model
PWR	Pressurized water reactor
ROM	Reduced-order model
SAS	Scale adaptive simulation
SRS	Scale-resolving simulations
TIV	Turbulence-Induced Vibrations
URANS	Unsteady Reynolds-Averaged Navier-Stokes

Funded by
the European Union

Summary

For an accurate prediction of the impact of flow induced vibration in nuclear power generation, computational methodologies are necessary that can simulate the interaction between fluids and structures. Within different components of the nuclear power generation system, interaction effects like turbulence induced vibration (mostly for axial flow cases) and flow/vortex induced vibration (mostly for cross flow cases) in single rod and rod-bundle configurations occur. Simulation of such cases using direct CFD-FEM coupling approaches with high fidelity models may provide an accurate prediction, but at a prohibitive computational cost.

In this work package, fast-running methods are identified that improve computational speed for such cases by reducing computational complexity. Each of the methods described in this report aims to reduce the computational complexity by simplifying a specific part of the flow induced vibration problem. Two methods target in particular the effect of turbulence and turbulence pressure fluctuations: by introducing a synthetic turbulence model, the goal is to retrieve turbulence pressure fluctuations to similar accuracy as LES/DNS but at a much lower computational cost. Two levels of simplification are investigated: 1) considers the anisotropy of the Reynolds stresses and solves a Poisson equation to reconstruct pressure fluctuations from the synthetic turbulence velocity fluctuations, 2) uses an algebraic expression to correlate pressure fluctuations directly to the synthetic turbulence velocity fluctuations. Two other approaches use the decomposition of the structure dynamics into decoupled modes to: 1) simplify the fluid-structure coupling by introducing a reduced order model of the structure directly into the CFD solver, and 2) building a linear fluid response model for a subset of modal deformation shapes to replace the CFD solver.

The theoretical approach of these fast-running methods is documented, and some (initial) validation tests conducted.

Keywords

Synthetic turbulence, turbulence induced vibration, turbulence pressure fluctuation model, reduced order model, flow induced vibration, fluid-structure interaction

1. Anisotropic Pressure Fluctuation Model by NRG

This chapter presents the fast-running FSI model under development by the Nuclear Research & consultancy Group (NRG), in collaboration with the Delft University of Technology (TUD). It presents details of the model, as well as first validation results, both for pure fluid-flow cases and an FSI case.

1.1 Introduction

In the fuel assemblies, the flow is in axial direction and the driving FIV mechanism is Turbulence-Induced Vibrations (TIV), as the vibrations of the fuel rods are driven by the local, small-scale, turbulent velocity and pressure fluctuations. These fluctuations can numerically be resolved by, for example, the use of Large-Eddy Simulations (LES) or Direct Numerical Simulations (DNS). The drawback of these simulations though is that they require a large amount of computational power and time, and hence cannot be applied to most industrial applications. Cheaper numerical tools, such as those based on the Unsteady Reynolds-Averaged Navier-Stokes (URANS), which are widely used in the industry, do not resolve the fluctuations causing the structural vibrations.

To overcome this, the Nuclear Research & consultancy Group (NRG) in the Netherlands has been working on the development of the Pressure Fluctuation Model (PFM) [1], [2]. This model makes use of local average velocity and turbulence fields to create instantaneous velocity fluctuations. With these velocity fluctuations, the pressure fluctuations can be determined. These, in turn, are added to the averaged pressure and fed to the structural solver as boundary conditions. This combined URANS-PFM model has been tested in a selected number of FIV cases and from comparison to experimental data it was found that the PFM predicts vibration amplitudes in the same order of magnitude [2]. However, from the numerical tests it was also found that the PFM still has some shortcomings.

To address these shortcomings, an improved pressure fluctuation model, called Anisotropic Pressure Fluctuation Model (AniPFM), has been created. The new model tackles several limiting assumptions of the PFM, such as that of isotropic turbulence and the method of time correlation used in PFM. With these extensions to the PFM, the AniPFM increases the accuracy in the prediction of vibration amplitudes through FIV-simulations of TIV. This chapter presents this new AniPFM. In the next Section, the new AniPFM is described in detail. Subsequently, in Section 1.3, the numerical framework, in which AniPFM is implemented and which is used to simulate flow-induced vibration problems is discussed. Subsequently, in Section 1.4 flow-only simulations with AniPFM are described, and results are compared with experimental and numerical reference date. In Section 1.5, a first FIV test case is presented, with results compared to available experimental data, and to other available numerical results. Finally, in Section 1.5, conclusions and future work are listed.

1.2 Anisotropic Pressure Fluctuation Model

In this chapter, the new AniPFM is discussed. The name is derived from the fact that this model is able to reproduce anisotropic Reynolds stresses. It is based on the formulation of the PFM as presented by Kottapalli et al. [2], though major modifications have been made

to incorporate anisotropy and accurate time correlation, using, amongst others, approaches from Billson et al. [3], and Shur et al. [4]. First, the generation of velocity fluctuations is discussed, including the separate components and steps needed to create them. After this, the generation of the pressure fluctuations is discussed. Finally, the numerical framework in which the AniPFM is implemented and which is used to simulate FIV problems is presented.

1.2.1 Dimensionless velocity fluctuations

The first step in generating velocity fluctuations that are a function of space and time and with which an anisotropic turbulent velocity field can be reconstructed is to construct dimensionless velocity fluctuations that are solely a function of space. These dimensionless fluctuations $\boldsymbol{w}_t(x)$ are created by a Fourier decomposition as follows, similarly to what is done by Shur et al. [4]:

$$\boldsymbol{w}_t(x) = \sqrt{6}\sum_{n}^{N}\sqrt{q_n}[\boldsymbol{\sigma}_n \cos\left(\boldsymbol{k}_n \cdot \boldsymbol{x} + \varphi_n\right)], \tag{1}$$

here, q_n is the mode amplitude, $\boldsymbol{\sigma}_n$ is the direction vector, $\boldsymbol{k}_n$ is the wavenumber vector, and φ_n is a random phase shift with a uniform distribution. The subscript n denotes the n-th Fourier mode, with in total *N* modes.

1.2.1.1 Wavenumber range

There are three important parts to create a proper Fourier decomposition of the dimensionless velocity fluctuations, viz. (a) the choice of the range and distribution of the *N* modes used, (b) the specification of the amplitude of each mode, which represents the energy contained in that mode, and (c) setting the direction of each mode. For the third part, it requires specifying a starting mode k_{start}, corresponding to the first mode, and an end mode k_{end}, which is mode *N*. The smallest wavenumber k_{start} corresponds to the largest eddy length scale *L* in the domain, for which a conservative estimate can be found from the following equation:

$$k_{start} = \frac{\epsilon}{\max(\|\boldsymbol{u}\|)}, \tag{2}$$

with ϵ the energy dissipation rate and $\boldsymbol{u}$ the URANS velocity. Some other considerations must also be taken in account though in order to properly set k_{start}. First, the starting wavenumber must be lower than the wavenumber with the maximum energy density k_e. Furthermore, geometrical considerations must also be taken into account. For this, the user can input a user length scale l_{user}, which denotes the maximum length that can be captured given the geometry of the problem. For example, in turbulent channel flow the maximum wavelength in the wall-normal direction is equal to the channel height. Taken these considerations into account, the following expression is used for k_{start}:

$$k_{start} = \max\left[\min\left(k_{start}, \frac{1}{2}k_e\right), \frac{2\pi}{l_{user}}\right]. \tag{3}$$

As for k_{end}, a cut-off wavenumber is used

$$k_{end} = \frac{3}{2} k_{cut}, \tag{4}$$

with $k_{cut} = \frac{2\pi}{l_{cut}}$ and l_{cut} a user-defined cut-off length. Several expressions for this cut-off length were investigated, such as having it depend on the local cell size, as smaller waves would not be accurately resolved by the model. However, it was found that the cut-off length as defined by Shur et al. [4] gives the most accurate results:

$$l_{cut} = 2 \min\left[\max\left(h_y, h_z, 0.3h_{max}\right) + 0.1d_w, h_{max}\right], \tag{5}$$

with h_y and h_z local cell sizes in spanwise and wall normal direction, respectively, h_{max} the maximum of the three local cell sizes, and d_w the distance to the wall. Given the wavenumber space from k_{start} to k_{end}, the space is divided in *N* intervals, with *N +1* edge wavenumbers. These edge-wavenumbers are used to define Δk_n. The edge-wavenumbers are logarithmically distributed.

1.2.1.2 Turbulent kinetic energy spectrum

The mode amplitude q_n specifies the amount of energy contained in that mode. Similarly to the old PFM, it is defined by a modified Von-Kármán energy spectrum $E(k)$. Though since for the AniPFM dimensionless velocity fluctuations are needed, the energy per mode is normalized in the following way:

$$q_n = \frac{E_k(k_n)\Delta k_n}{\sum_n^N E_k(k_n)\Delta k_n}, \tag{6}$$

where $E_k(k_n)$ is the modified Von-Kármán energy spectrum evaluated at k_n. This spectrum is given by the expression below:

$$E(K) = \frac{(k/k_e)^4}{[1 + 2.4((k/k_e)^2)]^{17/6}} \exp\left(-\left(12\frac{k}{k_\eta}\right)^2\right) f_{cut}, \tag{7}$$

where k_e is the earlier mentioned wavenumber at which the energy spectrum has its maximum, and k_η is the Kolmogorov wavenumber. This spectrum is very similar to the one used in the old PFM, however, a big difference is that now the constant *A* found in the previously used expression for the spectrum is no longer necessary, as the value for q_n is scaled by normalization. Because of this, the integral used to determine this constant *A* does not have to be evaluated, which reduces the total computational time and the complexity of the model.

The modified Von Kármán spectrum is multiplied by a cut-off filter f_{cut}. Without this cut-off filter, the spectrum continues until the Kolmogorov wavenumber. However, typically the mesh cannot resolve wavenumbers that far; otherwise, it would be more favorable to perform a DNS. Since the input spectrum would not be fully resolved, an aliasing effect can be found in the reconstruction of the energy spectrum. To counteract this, a cut-off filter

is used, which improves the reconstructed energy spectrum. The used expression in AniPFM for the cut-off filter is [4]:

$$f_{cut} = \exp\left(-\left[\frac{4\max(k - 0.9k_{cut}, 0)}{k_{cut}}\right]^3\right), \tag{8}$$

with k_{cut} as given in Section 1.2.1.1.

1.2.1.3 Direction vector

The final part needed for a proper Fourier decomposition of the dimensionless velocity fluctuations is the specification of the wavenumber vector and its direction vector. For the former, AniPFM uses the same definition as previously used in the old PFM, see also Figure 1:

$$\boldsymbol{k}_n = k_n[\sin\theta_n \cos\psi_n\,, \sin\theta_n \sin\psi_n\,, \cos\theta_n\,], \tag{9}$$

where θ_n, ψ_n and φ_n are random variables with distributions given by:

$$P(\psi_n) = \frac{1}{\pi}, \quad P(\varphi_n) = \frac{1}{2\pi}, \quad P(\theta_n) = \frac{1}{2}\sin(\theta_n)\,. \tag{10}$$

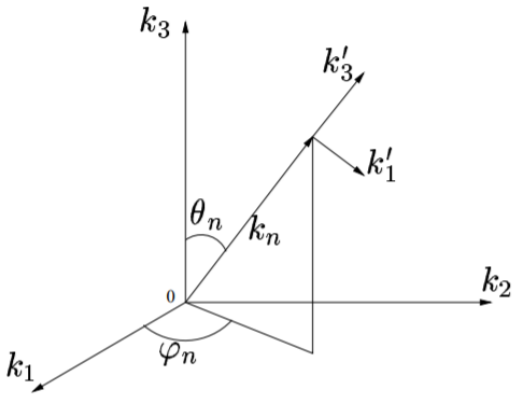

Figure 1. Wave vector geometry of the n-th Fourier mode [3].

The wavenumber direction vector is determined from the wavenumber vector. Based on continuity, it can be found that $\boldsymbol{k}_n \cdot \boldsymbol{\sigma}_n = 0$. To achieve this, $\boldsymbol{\sigma}_n$ is defined as the normalised cross-product between a random vector $\boldsymbol{\zeta}_n$, and the wavenumber vector:

$$\boldsymbol{\sigma}_n = \frac{\boldsymbol{\zeta}_n \times \boldsymbol{k}_n}{|\boldsymbol{\zeta}_n \times \boldsymbol{k}_n|}. \tag{11}$$

Since the dot-product of a vector with the cross product of the same vector is always equal to zero, the continuity condition is met.

1.2.2 Time correlation

The second step in generating the desired space-time dependent velocity fluctuations is implementing proper time correlation in the dimensionless and purely space-dependent

velocity fluctuations of Section 1.2.1. Two phenomena contribute to the time correlation of the velocity field, namely the convection of the turbulent eddies and the decorrelation due to the production and dissipation terms. To introduce this time dependency, a two-step method similar to Billson et al. [3] is used:

$$\frac{\partial \boldsymbol{v}_t^{m-1}}{\partial t} + U_j \frac{\partial \boldsymbol{v}_t^{m-1}}{\partial x_j} = 0. \tag{12}$$

$$\boldsymbol{v}_t^m(\boldsymbol{x}, t) = a\boldsymbol{v}_t^{m-1}(\boldsymbol{x}) + b\boldsymbol{w}_t^m(\boldsymbol{x}). \tag{13}$$

Here, $\boldsymbol{v}_t^{m-1}$ are the non-dimensional velocity fluctuations generated at time step *m-1*, and U_j is the Reynolds-averaged velocity as produced by URANS. In the first step, i.e. Eq. (12), the dimensionless velocity fluctuations are convected with the URANS velocity. Then, in the second step, a new solution $\boldsymbol{v}_t^m(\boldsymbol{x}, t)$ is calculated from a combination of the (convected) previous solution $\boldsymbol{v}_t^{m-1}(\boldsymbol{x})$, and a newly generated field $\boldsymbol{w}_t^m(\boldsymbol{x})$. The coefficients *a* and *b* are defined by:

$$a = e^{-f_\tau \Delta t/\tau}, \quad b = \sqrt{1 - a^2}, \tag{14}$$

with τ the dissipation timescale determined from the URANS simulation, and f_τ a modification factor for fine-tuning the correlation. In line with [3], a value of f_τ = 17 is initially used. Tests showed that this value gives a satisfactory correlation in the simulations of interest.

1.2.3 Scaling

The third and final step in generating velocity fluctuations is to scale the space-time dependent velocity fluctuations of Section 1.2.2 such that they replicate the desired Reynolds stresses and hence introduce the desired anisotropy. The final velocity fluctuations $\boldsymbol{u}_t(\boldsymbol{x}, t)$ are constructed from non-dimensional isotropic fluctuations $\boldsymbol{v}_t(\boldsymbol{x}, t)$ through the following expression:

$$\boldsymbol{u}_t(\boldsymbol{x}, t) = a_{ij}\boldsymbol{v}_t(\boldsymbol{x}, t), \tag{15}$$

With a_{ij} the Cholesky decomposition of the Reynolds stress tensor *R*, given by:

$$a_{ij} = \begin{bmatrix} \sqrt{R_{11}} & 0 & 0 \\ \dfrac{R_{21}}{a_{11}} & \sqrt{R_{22} - a_{21}^2} & 0 \\ \dfrac{R_{31}}{a_{11}} & \dfrac{(R_{32} - a_{31}a_{21})}{a_{22}} & \sqrt{R_{33} - a_{31}^2 - a_{32}^2} \end{bmatrix}. \tag{16}$$

For the Cholesky decomposition *a*, it follows that $a^T a = R$. Thus, if $\langle \boldsymbol{v}_t(\boldsymbol{x}, t)^2 \rangle = \delta_{ij}$, it follows that $\langle \boldsymbol{u}_t(\boldsymbol{x}, t)^2 \rangle$ is the Reynolds stress tensor. From this it can be concluded that $\boldsymbol{v}_t(\boldsymbol{x}, t)$ must indeed be isotropic, and the squared-averaged components must be equal to unity.

With this method, the AniPFM can reconstruct anisotropic Reynolds stresses. For flows with a constant pressure gradient, such as channel flows, linear eddy viscosity models show isotropic Reynolds stresses. In order to improve the accuracy of these models, a correction is used to transform the isotropic tensor into an anisotropic tensor, based on the nonlinear eddy viscosity model of Wilcox [5]:

$$\overline{u'u'} = \frac{8}{9}k, \quad \overline{v'v'} = \frac{4}{9}k, \quad \overline{w'w'} = \frac{6}{9}k. \tag{17}$$

1.2.4 Pressure fluctuations

With the three steps outlined in the previous sections, the desired space-time dependent velocity fluctuations are created. The velocity fluctuations require as input the turbulent kinetic energy and the turbulent dissipation rate. These are obtained from URANS. As the AniPFM must model the pressure fluctuations, it is necessary to derive how they relate to the generated velocity fluctuations. This dependence is derived in a similar way as done for the previous PFM.

First, in the incompressible momentum equation, the Reynolds decomposition of the velocity $\boldsymbol{u} = \bar{\boldsymbol{u}} + \boldsymbol{u}'$ and pressure $p = \bar{p} + p'$ is substituted. Then, the averaged momentum equation is subtracted, and the divergence operator is applied. This results in the following Poisson equation for the pressure fluctuations:

$$\frac{\partial^2 p'}{\partial x_i \partial x_i} = -\rho_f \left[2\frac{\partial \bar{u}_i}{\partial x_j}\frac{\partial u'_j}{\partial x_i} + \frac{\partial^2}{\partial x_i \partial x_j}\left(u'_i u_j{}' - \overline{u'_i u_j{}'}\right)\right]. \tag{18}$$

From this equation, it is evident that the pressure fluctuations only depend on the mean velocity $\bar{u}_i$ and the Reynolds stresses $\overline{u'_i u_j{}'}$, which can both be obtained from the URANS solution, and the modeled velocity fluctuations u'_i. Hence, all necessary ingredients are in place to generate the desired pressure fluctuations and to perform FIV simulations using URANS in combination with the Anisotropic Pressure Fluctuation Model.

1.2.5 Model overview

The previous sections outlined the necessary steps needed to generate the velocity fluctuations, and with those as input, the desired pressure fluctuations. In Figure 2, the full model is summarized. First the non-dimensional velocity fluctuations are calculated, based on the energy spectrum. Then the time correlation is performed. After this, the velocity fluctuations are computed by scaling with the Cholesky tensor. Finally, p' can be computed.

1.3 Computational Framework

AniPFM is implemented in the finite volume OpenFOAM framework, which is also used to solve for the governing fluid equations. The URANS equations are discretized in space with a PIMPLE algorithm which is a combination of the classical PISO and SIMPLE algorithms. The consistent second-order backward difference scheme (BDF2) developed for moving grids is used to integrate the equations in time. The mean pressure field resulting from the

URANS solver is superimposed with the pressure fluctuations field coming out of AniPFM and subsequently passed on to the solid solver as boundary conditions.

The governing equations for the solid problem are solved by means of the finite element approach implemented in the library Deal.II [6]. In particular, the linear finite element approximation is used to discretize the governing equations in space, and the Theta-method is used to integrate the structural equations in time. In all the cases reported in this work, the value $\theta = 0.6$ is used for the time integration of the structural problem.

The fluid and solid solvers are coupled through the preCICE library [7] for solving Fluid-Structure Interaction (FSI) problems. Due to the fact that the fluid and solid meshes are generally not conforming at the fluid-structure interface, forces and displacements must be mapped from one grid to the other. To this purpose, radial basis functions implemented in preCICE are used to map the displacements from the solid to the fluid interface in a consistent way, and to map the forces from the fluid to the solid interface in a conservative way.

A partitioned, parallel implicit coupling solver is used to solve the FSI problem. In implicit approaches, the flow and structural problems are solved iteratively until convergence of the FSI problem is satisfied within one time step. Here, convergence means that the equality of displacements and stresses is guaranteed up to a certain tolerance. For all simulations reported here, the interface quasi-Newton technique with an approximation for the inverse of the Jacobian from a least-squares model (IQN-ILS) of [8] is used as an acceleration technique for convergence. This method is proved to be more robust than Aitken's under-relaxation methods for strongly coupled problems.

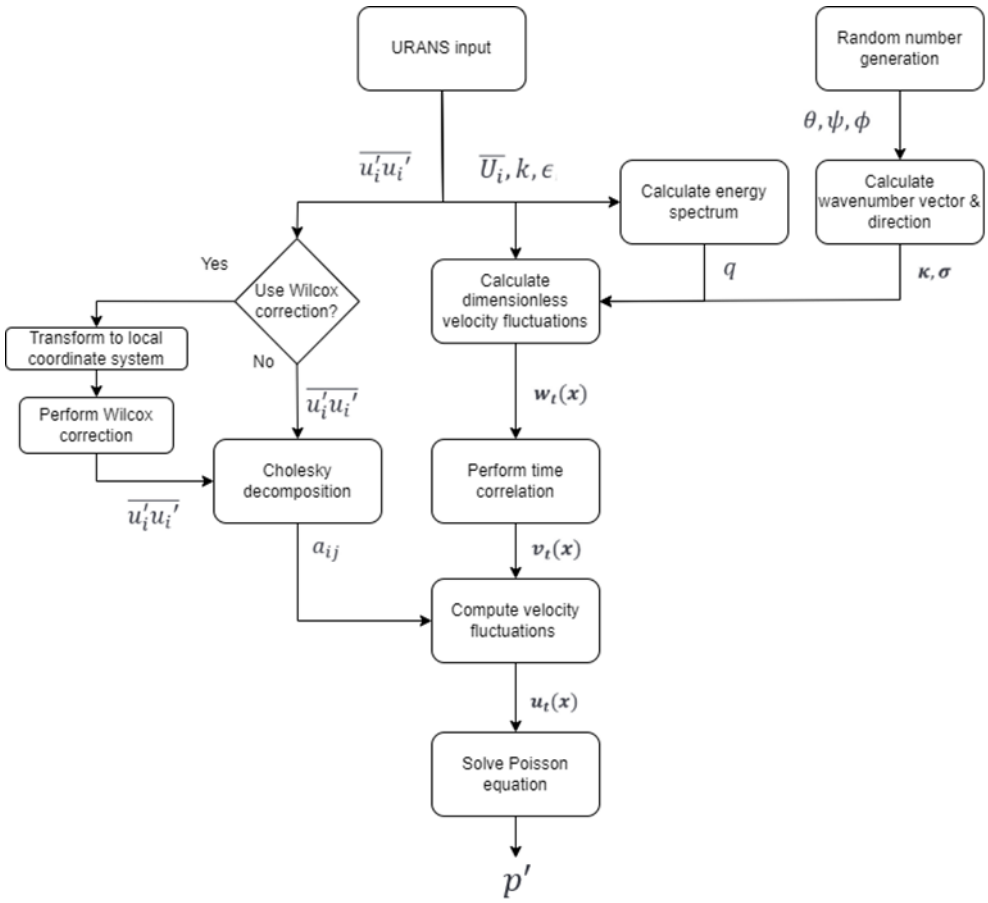

Figure 2: A flow-chart of the different computational steps of the proposed AniPFM.

1.4 AniPFM Fluid-Only Validation

Two fluid-only cases were simulated, in order to validate the AniPFM in terms of velocity and pressure fluctuation statistics. First, a Homogeneous Isotropic Turbulent (HIT) box was simulated, which was used to verify the AniPFM in isotropic conditions, since an isotropic energy spectrum was used as input. Second, a Turbulent Channel Flow (TCF) was simulated, with the purpose of testing the accuracy of the AniPFM versus the PFM in anisotropic turbulence. The setup of these two cases is discussed in this section. The AniPFM is implemented in OpenFOAM 8, and thus all subsequent simulations have been performed with the same software.

1.4.1 Homogeneous isotropic turbulent box

For the HIT validation case, two different simulations will be done. One replicating the experiment of Comte-Bellot & Corrsin [9], and one replicating the DNS of Gotoh et al. [10]. First, the methodology for both cases is discussed. After this, the results for both cases are elaborated upon. Both cases have slightly different purposes. First, the Comte-Bellot & Corrsin experiment gives data of the three-dimensional energy spectrum, as well as data on the time-correlation of the axial velocity. The energy spectrum data will be used to verify that the PFM indeed can replicate an isotropic energy spectrum. Next to this, the ability of the AniPFM to replicate the actual time correlation is tested. Several parameters of the

AniPFM will be varied such that the influence of these parameters can be evaluated. The DNS of Gotoh et al. contains data of the nondimensional energy and pressure spectrum for several Reynolds numbers Re_λ, where λ is the Taylor microscale. This data will be used to validate the implementation of the calculations of the pressure fluctuations for several Reynolds numbers.

1.4.1.1 Simulation Setup

A box of $L \times L \times L$ is created, which is discretized by a cartesian mesh of $N \times N \times N$ cells. All boundaries are periodic, and the domain has a zero-mean velocity. There are no source terms, thus the turbulence in the box will decay over time. In Table 1, the details of the replicated set-up of the experiment of Comte-Bellot and Corrsin and the DNS of Gotoh and Fukayama are shown. The latter was specified in dimensionless numbers. For validation of AniPFM, the simulation with $Re_\lambda = 284$ of Gotoh and Fukayama is replicated.

Table 1: Details of the simulation replicating Comte- Bellot and Corrsin and Gotoh and Fukayama at $Re_\lambda = 284$

	Comte-Bellot and Corrsin [9]	Gotoh and Fukayama [10]
Turbulence model	$k - \varepsilon$	$k - \varepsilon$
Initial *k* [m²/s²]	0.4740	0.012568
Initial ε [m²/s³]	0.07393	0.01377
Initial *U* [m/s]	0	0
Initial p [Pa]	0	0
ν [m²/s]	1.5e-5	1.5e-5
Time step [s]	0.001	0.001
Duration [s]	0.874	0.001

1.4.1.2 Results

In Figure 3, the simulated velocity fluctuations of the HIT box of Comte-Bellot Corrsin are shown, with a mesh size of N = 128. The velocity fluctuations on the left are from the AniPFM, whereas the results on the right are simulated through means of a Large-Eddy Simulation [11]. From Figure 5, it was concluded that the AniPFM can qualitatively reconstruct similar flow structures as high-resolution methods.

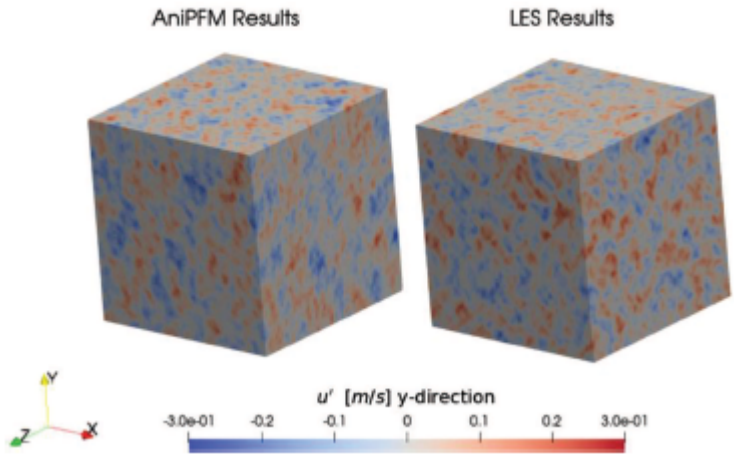

Figure 3: The instantaneous velocity fluctuations of the AniPFM, compared to LES results.

In Figure 4, the energy spectra generated by both the AniPFM and the PFM of Kottapalli et al. [1] are compared to the experimental spectrum of Comte-Bellot & Corrsin. The AniPFM results show a very good resemblance with respect to the experimental results, right up to the cut-off wavenumber. Compared to the results of the PFM, the peak of the energy spectrum is better predicted, and there is no unphysical accumulation of energy near the cut-off wavenumber. The latter difference is due to the fact that a cut-off filter is used in the AniPFM, which makes sure that the unresolved energy is not redistributed over the resolved part of the spectrum.

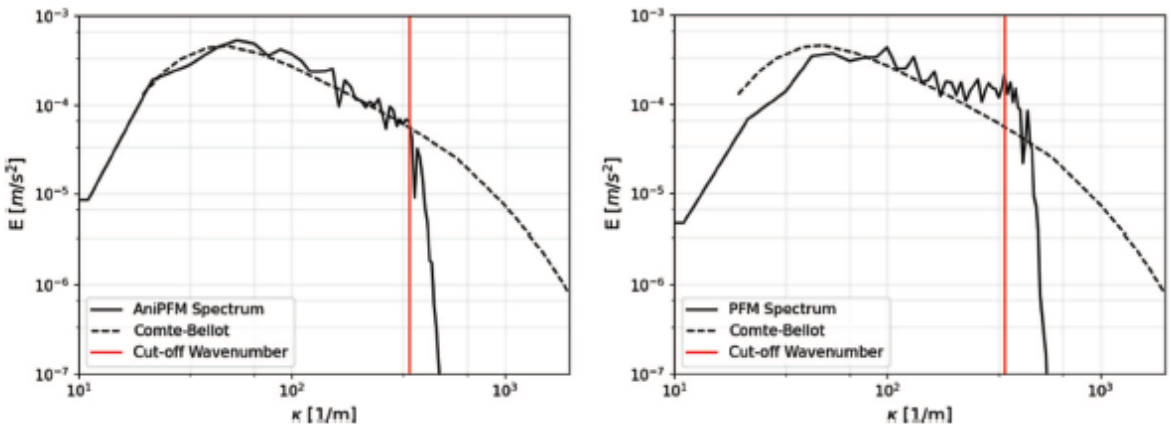

Figure 4: The energy spectrum of the new AniPFM (left) and the old PFM (right), compared to the experimental values of Comte-Bellot and Corrsin [9].

The time correlation of the velocity and pressure fluctuations is of great importance for the application to FSI simulations of nuclear fuel rods. This is because the pressure fluctuations that have a frequency close to the eigenfrequency of the fuel rod are expected to have the largest influence on the excitation of the fuel rods. Thus, it is important to model the distribution of the pressure fluctuations over the frequency domain correctly. For this reason, the time correlation is investigated. From the experiment of Comte-Bellot &

Corrsin, the correlation of the velocity fluctuations in the x-direction are known, these are compared to the time correlation of the velocity fluctuations of the PFM and the AniPFM.

As can be seen in Figure 5, the PFM shows a much faster decorrelation than the experiment by Comte-Bellot & Corrsin, and the AniPFM. This is due to the fact that the PFM uses a convection velocity not based on the mean velocity, but rather on the wavenumber and the dissipation rate. Because of this, the convection velocity for each mode is not directly dependent on the mean velocity. As can be seen, this can lead to a fast decorrelation in the velocity fluctuations. Regarding the AniPFM, a much better approximation is shown, which a maximum error of 11.8%. This verifies that using an exponential relation for the correlation is an improvement over the previous method, for isotropic turbulence.

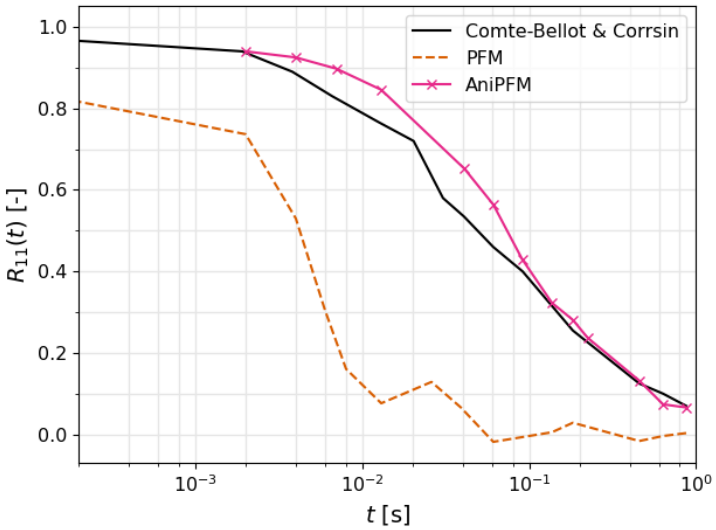

Figure 5: Comparison of the velocity time correlation between the PFM, AniPFM, and the experimental data from Comte-Bellot & Corrsin [9].

The variable that is passed from the AniPFM to the structural solver is p′, so it is of utmost importance that it is verified that this can be replicated correctly. For this reason, the pressure spectrum is evaluated, and compared to both the results of the previous PFM, and to DNS results of Gotoh et al. [10]. The results for both the old PFM and the new AniPFM are shown in Figure 6. As can be seen, both models show a similar result w.r.t. the DNS data from Gotoh et al. The old PFM shows a small underprediction, while the AniPFM shows a slight overprediction.

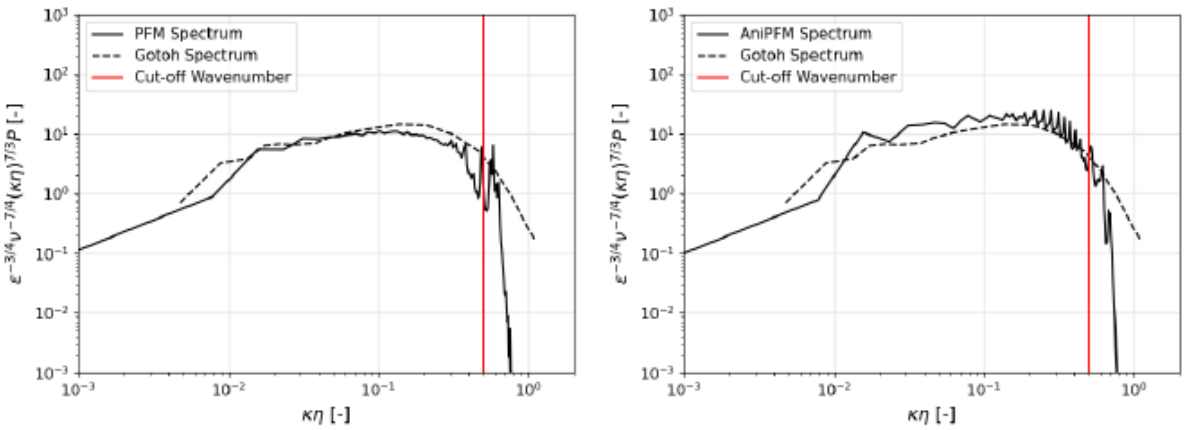

(a) PFM (b) AniPFM.

Figure 6: The reproduction of the pressure spectrum of PFM (left) and AniPFM (right), versus the spectrum from Gotoh et al. [Figure 6].

1.4.2 Turbulent Channel Flow

In this section, the simulations of a turbulent channel flow are discussed. The results of the TCF are compared to the DNS results of Abe et al. [12], who performed a DNS simulation at several Reynolds numbers. The highest Reynolds number was equal to $Re_\tau = 640$, thus this Reynolds number is used for comparison. The DNS of Abe et al. was chosen, as from this simulation, information was available about the mean flow characteristics along the wall-normal direction, such as the mean velocity and Reynolds stresses. It also contained spectral data about the pressure and velocity components, both near the wall and closer to the bulk of the flow.

The TCF case is used to verify several aspects of the AniPFM. Errors in the prediction of the pressure fluctuations can be introduced from several sources, here the effect of each source is discussed. The different sources of errors are the modelling error, the discretization error, and finally the input error. Furthermore, due to the fact that random numbers are used to construct the wavenumber and direction vector, an uncertainty in the results is introduced. It was also observed that the RMS pressure fluctuations changed slightly over time, introducing another uncertainty. After assessing these errors and uncertainties, the modelling choices are further investigated by evaluating the effects of certain individual model choices.

1.4.2.1 Simulation Setup

In TCF, the flow between two infinitely long and wide stationary plates is simulated. The simulation domain used is equal to $6\delta \times 2\delta \times 3\delta$, where δ is the mid-channel height, see Figure 7 left. The mesh has a size of $N_x \times N_y \times N_z$ cells, which are kept as variables. The mesh distribution is uniform in the stream- and spanwise-direction, and it is geometrically expanding to the mid-channel plane in the wall-normal direction. The mesh in the wall-normal direction is configured such that $y^+ \approx 1$ for the first grid cell from the wall. An example mesh is shown in the right of Figure 7. Simulations were performed with the $k-$

ω *SST* turbulence model, along with the Wilcox correction. However, for several simulations, no URANS calculation was done, but rather the mean flow properties of the DNS of Abe et al. were used as an input to the AniPFM. This was used to isolate any errors that originate due to the AniPFM, and not due to the input.

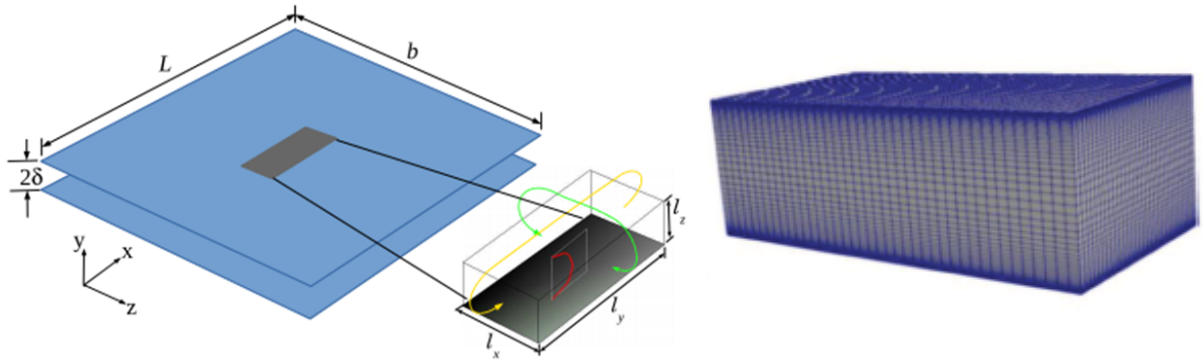

Figure 7: Domain (left) and example mesh (right) used for the TCF simulations.

1.4.2.2 Results

While quantitative results such as root-mean-squared values and pressure spectra are absolutely necessary for evaluating the effectiveness of the AniPFM, qualitative results are as important. Without qualitative results, statistics such as mean or mean-squared values can sometimes be misleading. For this reason, the Root-Mean Square (RMS) pressure and velocity fluctuations are shown in Figure 8. It can be seen that mainly at the top wall the RMS pressure fluctuations have a large magnitude, in the mid of the channel the fluctuations are much closer to zero. This is due to the fact that the highest velocity and Reynolds stress gradients are near the wall. For the RMS velocity fluctuations, it is clear that near the wall, the magnitudes are larger than in the midchannel, but at the wall they are exactly zero. This is due to the no-slip condition. Also, the RMS values are almost constant over the span and streamwise direction, with only small variations in these directions. This was as expected, as the channel flow case is supposed to be homogeneous in these directions. Since this is also the case for the AniPFM results, it is justified to collapse this data to a single profile as function of the wall-normal direction, which is done for the subsequent results.

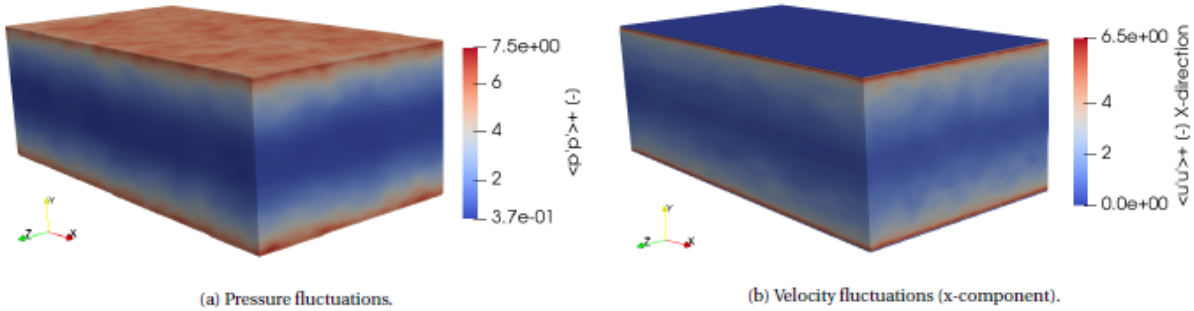

(a) Pressure fluctuations.

(b) Velocity fluctuations (x-component).

Figure 8: The mean squared pressure and velocity fluctuations, taken fromAniPFM.

For the turbulent channel flow, there are several sources of errors that cause a discrepancy between the AniPFM results and experimental/DNS data. Therefore, it is important that

each source is carefully evaluated. There exists an uncertainty range in the results of the AniPFM, which is due to the random numbers that are used throughout the simulation. For the chosen temporal correlation scheme, the random numbers gave an uncertainty range of 0.±25% for p'_{RMS}, for a confidence interval of 95.4%. The number of modes did not seem to have a large effect on p'_{RMS}, however, with a lower number of modes, the uncertainty went up, as fewer random numbers were used per iteration. For the presented simulations, 1024 wave number modes were used.

The amount of energy that is resolved by the AniPFM depends on the fineness of the mesh. There is no sub-grid model that models the effect of unresolved velocity fluctuations on the pressure fluctuations. Thus, the statistics of the pressure fluctuations only converge if a large part of the velocity fluctuations is resolved. Since p'_{RMS} is the quantity of interest, this quantity is evaluated for several meshes. This is shown in Figure 9, in which the results were obtained using the $k-\omega\,SST$ turbulence model, together with the Wilcox correction. It can be seen that the meshes converge to a final solution when using finer meshes. At the second finest mesh, the results near the wall are within the given uncertainty range, thus deeming the solution converged.

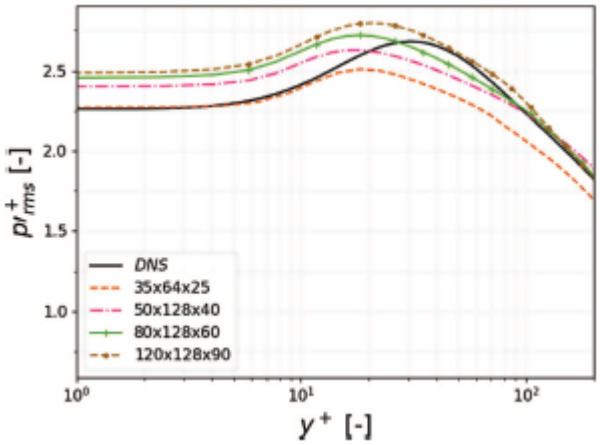

Figure 9: The root-mean-squared pressure fluctuations along the wall-normal coordinate for various meshes, versus the DNS results of Abe et al. [12].

The modelling error was found by performing a simulation of the turbulent channel flow on the finest mesh from Figure 9, but with the RANS input variables $(k, \varepsilon, \overline{u_i}, \overline{u'_i u'_j})$ taken from DNS data. The replicated Reynolds stresses and p'_{RMS} are shown in Figure 10 left. The Reynolds stresses are very closely approximated. The small under-estimation is because the velocity fluctuations are not fully resolved. Nevertheless, it was found that these unresolved fluctuations had no effect on p'_{RMS}. From Figure 10 (right), it can be seen that near the midchannel plane, the AniPFM very closely approximates p'_{RMS}. This is because here the isotropic energy spectrum very closely approximates the actual energy spectrum. Near the wall, the energy spectrum is not approximated as accurately, due to the larger anisotropy in the flow. Thus, a larger discrepancy in p'_{RMS} was found near the wall, with a maximum error of 4.4%.

Funded by
the European Union

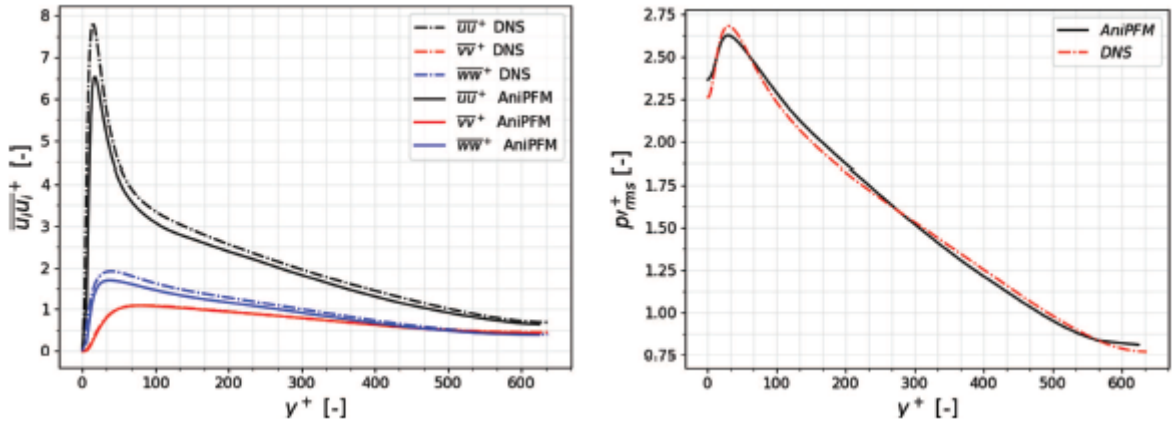

Figure 10: The Reynolds stress profiles (left) and the RMS pressure fluctuations (right) along the wall-normal coordinate, versus the DNS results of Abe et al. [12]. DNS data is used as input.

1.5 FSI validation case

In the previous chapter, results of two fluid-only test cases that were performed to assess the performance of the AniPFM were presented. These two test cases were that of a homogeneous isotropic turbulent box, and of a turbulent channel flow. Velocity and pressure fluctuations statistics were compared to experimental data, and an improvement compared to the old PFM was found. A next step is to assess the performance of AniPFM in a test case involving FIV. To this end, the flexible brass beam experiment in turbulent water flow, performed by Chen & Wambsganss was selected [13]. This experiment was chosen because it closely mimics turbulence-induced vibrations found in nuclear reactors, and because it has been used in the past by others as a validation case for FSI problems with applications to nuclear fuel rods [2], [14], [15] .

The current chapter first gives a short description of the experiment, followed by the simulation setup used to perform the numerical calculations. Subsequently, results are presented, first of some pure AniPFM simulations, followed by AniPFM FSI simulations.

1.5.1 Experiment

The experiment consists of a flexible brass beam enclosed in a rigid steel cylinder, and that it is clamped on both sides. The discretized geometry as used by Kottapalli et al. [2] is shown in Figure 11. The diameter of the brass beam is D_c = 0.0127 m, the enclosing cylinder has a diameter of D_o = 0.0254 m, and the beam has a length of L = 1.19 m. This gives an L/D-ratio of 93.7. The level of turbulent intensity and the turbulent length scale at the inlet of the domain were not reported by [13]. Several studies [2, 14, 15] assumed a turbulence intensity of 5% and a turbulent length scale of 0.1 cm. The experiment was conducted for various mean inlet velocities, in the range of 8-33 m/s. This gives a range of Reynolds numbers from 101,600 - 419,100. The rod has a density of 8400 kg/m^3, giving a density ratio of $\rho_s/\rho_l = 8.4$. The experimental Poisson ratio was not reported, but a nominal value of 0.33 was taken, based on previous simulations [2]. Finally, a Young's modulus of E = 107 GPa was specified. The experiment established both data about the modal frequencies for several flow cases, and the root-mean-squared vibration amplitudes.

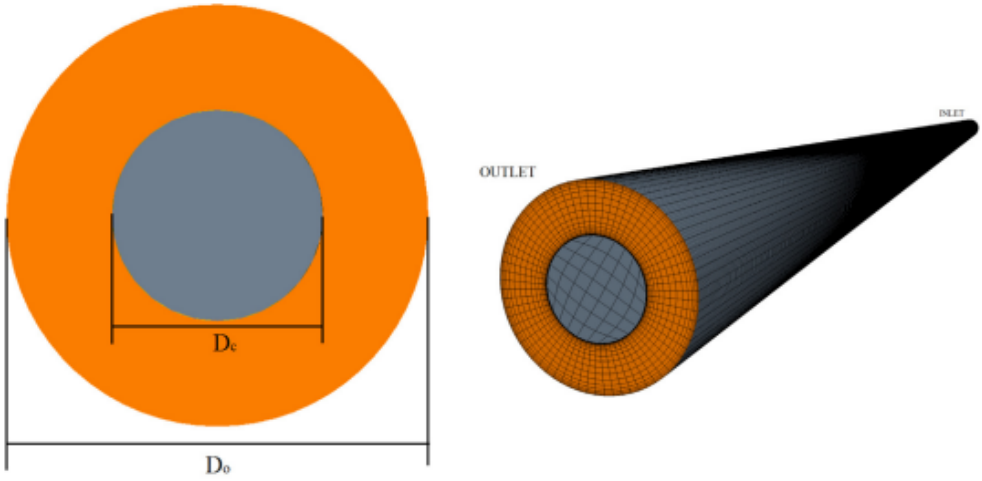

Figure 11: Discretized geometry of Kottapalli et al. [2], representing the experiment of Chen &Wambsganss [13].

1.5.2 Simulation setup

The configuration is set up such that the geometry mimics the experiment. For the simulations, a uniform inlet velocity is used, along with a turbulence intensity of 5% and a turbulent length scale of 0.1 cm. From preliminary tests, it was determined that these values do not have a large effect on the results. The flow is fully developed for the majority (roughly 90%) of the domain, and in this part, the kinetic energy profiles and pressure fluctuations are independent of the inlet conditions. Only near the inlet is a variation noticeable; however, the impact of this region on the structural vibration is hypothesized to be considerably less than that of the developed flow region of the domain.

The outer steel cylinder is kept rigid, whereas the inner brass beam is modelled as a moving wall. The brass beam is clamped at both ends, and it is assumed that the beam can be modelled with a linear elastic solver. For this, the relative displacements must be $A_{rms}/L \ll 1$, which can be found to be true based on the displacement values from the experiment. For the CFD side, URANS is used with the k – ω SST model.

The simulations are resolved up to the wall, which means that fine grids are necessary. An example of a mesh is shown in Figure 12, along with the used axis convention. Several fluid meshes are used to compare the results to the experiment and the simulations from previous papers. In these meshes, the axial and radial elements are varied to study its effects. The discretization in the tangential direction is fixed to 40 cells, which was found to be sufficient from a preliminary mesh study of pure CFD calculations. For the structural mesh, quadratic elements are used. From a preliminary mesh study, it was found that the results were converged for a structural mesh that has 25 elements in the x-y plane, and 50 elements in the axial direction. For both the solid and the fluid models, a second-order time scheme is used.

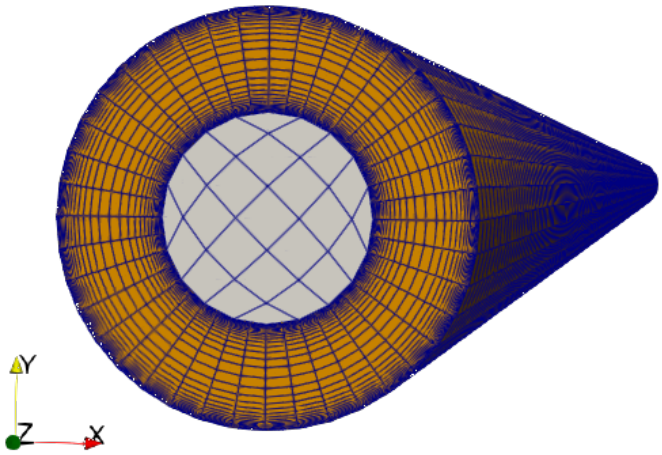

Figure 12: Discretized geometry of the brass beam case.

1.5.3 URANS FSI simulation

Before performing the AniPFM FSI simulation, a free vibration with flowing water URANS-only (without AniPFM) FSI simulation is performed for an inlet velocity of 10 m/s. This calculation serves as validation of the set-up, i.e., of the mapping method, the structural mesh and boundary conditions, and the coupling algorithm, are correct. For this calculation, the brass beam is subjected to an external load in a form of an initial distributed force for 0.015 s. This is the excitation mechanism, because with a pure URANS-approach, only the mean flow is resolved, without any pressure fluctuations responsible for inducing the vibrations.

The behaviour of an oscillating beam is known, and it can be represented with an exponentially damped sinusoid. In order to retrieve the natural frequency and the damping ratio, the displacements obtained from the FSI simulation are fitted to the function:

$$D(t) = A \cdot e^{-\lambda t} \cdot \cos(\omega t - \varphi) + \psi\,. \tag{19}$$

From this expression, the natural frequency f and damping ratio ζ can be obtained through:

$$f = \frac{2\pi}{\omega}, \qquad \zeta = \frac{\lambda}{\sqrt{\lambda^2 + \omega^2}}. \tag{20}$$

The displacement of the centre of the brass beam at z = 0.595 m is shown in Figure 13. As can be seen, it indeed follows the exponentially damped sinusoid shape. The function shows to be an excellent fit, with the largest relative standard deviation of any fitting parameter being 0.044%.

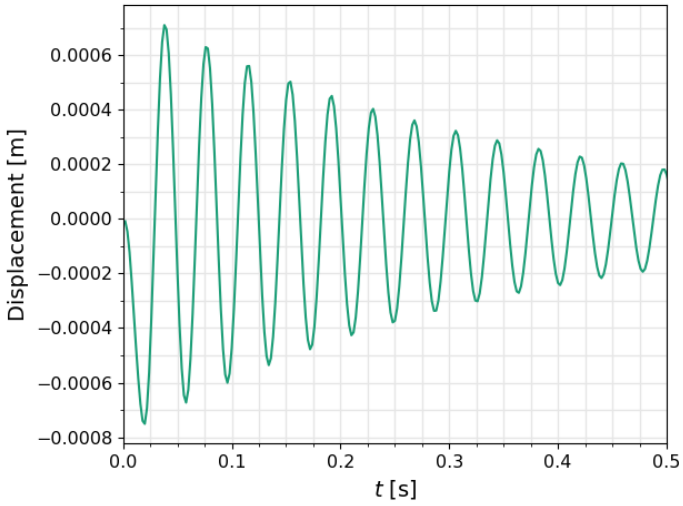

Figure 13: The displacement at mid-beam, for 0.5 s of simulated time.

In Figure 14, the fundamental natural frequency (left) and damping ratio (right) is compared with the experiment of Chen & Wambsganss [13], as well as other simulations taken from literature [2, 14, 15]. Note that from [14], the non-pre-stressed data is taken, in order to ensure a fair comparison. Furthermore, the experimental data from [13] is denoted by the green dots, whereas the line shows the theoretical results.

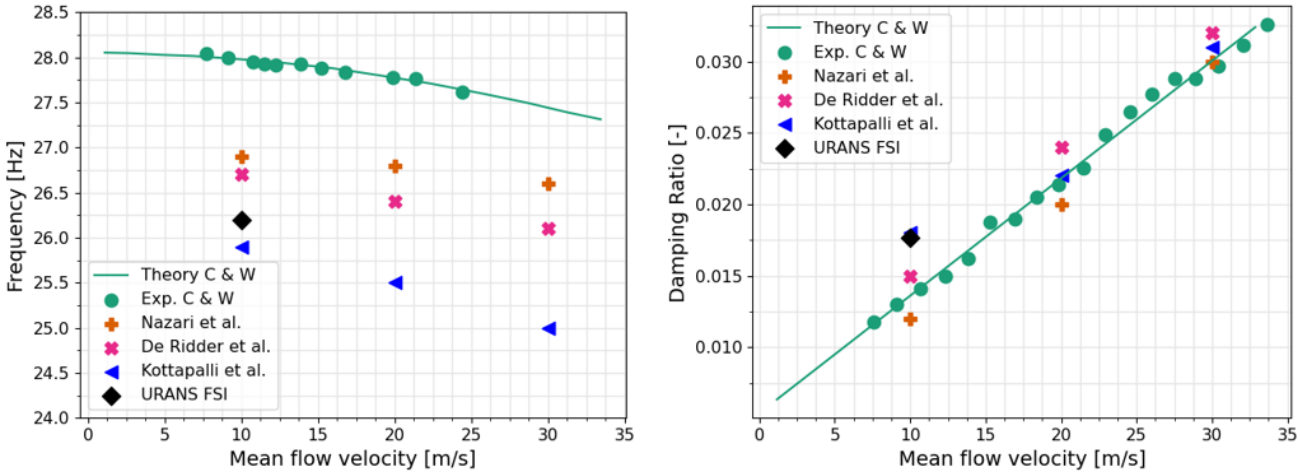

Figure 14: The calculated frequencies (left) and damping ratios (right) of the current work, compared to various simulations as well as experimental results [2, 13-15].

As can be seen from Figure 14, the frequency is in close agreement with the experiments and the other simulations. There is an error of 5.7% w.r.t. the analytical value, and an error of 5.4% w.r.t. the closest experimental value. The results are comparable to other published results. As for the damping ratio, it was found that the results are similar to those of Kottapalli et al. [2], but it shows a large error of 28.6 % with respect to the experiment of Chen & Wambsganss. It is believed that this is caused by the software packages used for the FIV simulations, as in other cases in which OpenFOAM – preCICE – Deal.II framework was used, also an overestimation in damping ratio compared with simulations done in STAR-CCM+ was found [16].

1.5.4 AniPFM FSI simulation

From the previous results, it was found that the general FSI set-up is in line with previously published results and thus that the model setup can be used for FSI simulations involving AniPFM. In this section, the Root-Mean Square (RMS) amplitudes obtained using the AniPFM FSI simulation are compared to those of the experiment by Chen & Wambsganss [13], in order to investigate the accuracy of the AniPFM. Simulations were performed at 10, 15, and 20 m/s. Note that not the same mesh is used in each simulation, but an equivalent mesh such that $y^+ = 1$ for all simulations. The maximum number of cells used in the simulations remains below the 1M though.

The results for the various flow velocities are shown in Figure 15. Here, again the dots indicate the experimental values of Chen & Wambsganss [13], whereas the line indicates the values calculated by their analytical model. The error bars again note the 95% confidence interval over the last 20 flow-through times. The results of the simulations using different initial seed numbers for generating random numbers are shown at 10 m/s. Although the effect of different seed numbers was not tested for higher velocities, the results at 10 m/s should give an indication of the uncertainty that higher flow velocities would experience as well. Note that the results of Nazari et al. [15] are not included, as they are one order of magnitude larger than all other data points.

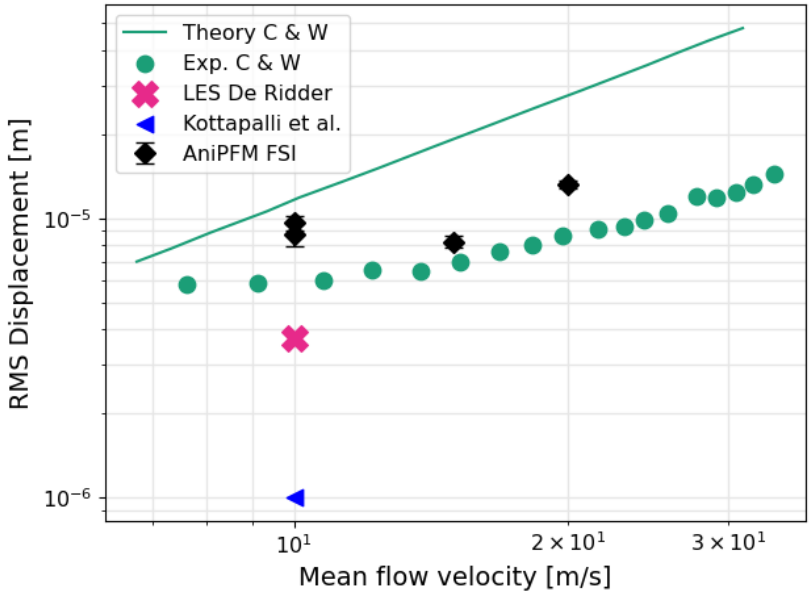

Figure 15: The RMS vibration amplitudes of the brass beam of the current work, compared to various simulations as well as experimental results [2, 13, 14].

The AniPFM shows a clear overestimation of the RMS amplitude, whereas the results of Kottapalli et al. [2] and De Ridder et al. [14] show an underestimation. Note that the simulation performed by De Ridder is a pure LES simulation, not an FSI simulation. The RMS amplitude was obtained using the force frequency spectrum as input of the theoretical model of Chen & Wambsganss [13]. The results of Kottapalli et al. [2] are obtained with a

URANS FSI methodology combined with a pressure fluctuation model, similar to the method presented in this paper.

Looking at relative errors, AniPFM over-predicts the RMS displacement by about 30-40 %, which is similar in magnitude to that of De Ridder et al. [14]. The relative error obtained by PFM is much larger though. Hence, from these first FIV simulations using AniPFM, it can be concluded that the use of the proposed AniPFM has shown an improvement in the prediction of the root mean-squared amplitude, compared to the previous pressure fluctuation model proposed by Kottapalli et al. [2]. Although the AniPFM showed a similar error w.r.t. the RMS amplitude as the large-eddy simulation of De Ridder et al. at 10 m/s, due to lack of data at other mean flow velocities, no conclusions can be made about the general accuracy of the AniPFM versus large-eddy simulations. Applying AniPFM to further test cases should give a more detailed indication of the performance of AniPFM compared to other available numerical tools and methods for simulating turbulence-induced vibrations.

1.6 Conclusions and future work

In this Chapter, a new pressure fluctuation model, called AniPFM is described. This model allows for the prediction of pressure fluctuations when using a URANS approach, which can be useful in particular for turbulence-induced vibration prediction. Several aspects of the AniPFM were adjusted with respect to the previous PFM of Kottapalli et al., namely the energy spectrum cut-off filter, the replication of anisotropic Reynolds stresses, and the method for time correlation.

After presenting the model and used computational framework, AniPFM was validated for pure flow-only cases, comparing velocity and pressure fluctuations statistics with available experimental data. This was done for both a Homogeneous Isotropic Box and a Turbulence Channel flow. With satisfactory results found when comparing with reference experimental and numerical data, attention was switched to a first application to an FIV test case. The test case under consideration is that of a flexible brass beam in turbulent water, as performed by Chen & Wambsganss in 1975. Results for URANS FSI simulations showed a good match for the natural frequency with the experimental one, though an over-prediction in the damping ratio. This latter is in line with what was observed previously with the numerical framework used. Next, results for FSI simulations involving AniPFM were compared with experimental data and other numerical results. Differences in RMS amplitudes of about 30-40% were found, which is a significant improvement from the previous PFM.

Future work will be aimed at testing AniPFM on other test cases. Moreover, further development of the model is foreseen, such as the testing the sensitivity of the model on some of the model parameters.

2. Implementation of the ANSYS Model Order Reduction for fast-running FSI simulations

Large cost reduction in a FSI simulation in terms of computational time can be achieved with reduced-order models for the fluid domain. This results from the fact that in a FSI simulation the CFD part is significantly more expensive than the structural one. Therefore, almost all fast-running models in GO-VIKING's WP5 are focused on the development and implementation of fluid-based ROMs. It is still worth investigating the savings in computational time when the model reduction is based on the structural part of the computational domain. This chapter first shortly introduces the Model order Reduction (MOR) approach, developed by ANSYS [17], then provides information on how to implement this and finally shows comparative results between reduced- and full-order model for a simplified test case.

2.1 Introduction to ANSYS MOR

2.1.1 The Method of Superposition

The Method of Superposition is a linear system method stating that in a linear system, the net response at each point of interest is the sum of the responses from each individual input acting alone. In structural mechanics, the Method of Superposition is utilized to solve static problems by dividing them into simpler parts. Each of the parts is then individually solved, by considering a single load at one time only. The individual solutions are then combined (superimposed) in one final solution that takes into account the overall effect of the original load.

For linearly elastic structures, the load P and the deformation δ are related through the stiffness K, as shown in Figure 16:

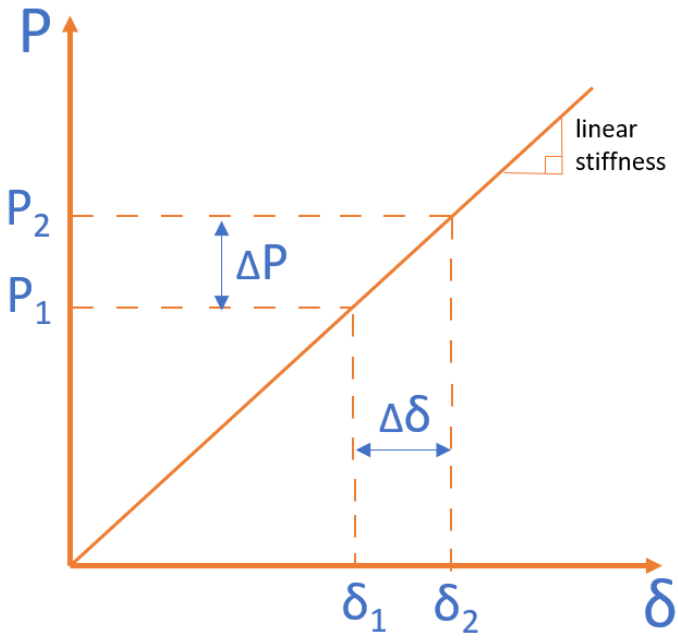

Figure 16: A typical load-deformation diagram of linear materials

For the first load applied on the structure:

$$P_1 = K\delta_1 \tag{21}$$

If ΔP had been applied instead, then:

$$\Delta P = K\Delta\delta \tag{22}$$

To obtain the total load applied on the structure as well as its deformation, both equations should be added:

$$P_1 + \Delta P = K\delta_1 + K\Delta\delta = K(\delta_1 + \Delta\delta) \tag{23}$$

Then the following equations can be derived from the diagram in Figure 16:

$$P_1 = P_2 + \Delta P, \qquad \delta_2 = \delta_1 + \Delta\delta$$

The expected and obvious result is:

$$P_2 = K\delta_2 \tag{24}$$

All this leads to the following conclusions:

- Deformation caused by a load can be added to the deformation caused by another load in order to obtain the resulting deformation from the application of both loads on the structure.

- The order in which the loads are applied on the structure does not play a role.

- It is possible to add or subtract loads that act on a structure.

These conclusions hold as long as the material behavior is linear, e.g. the structure is linearly elastic. In cases with plastic deformations the Method of Superposition cannot be applied. Plastic deformation is the ability of a solid material to undergo permanent deformation, which is a non-reversible shape change as a result of the applied loads. Further, this method is valid as long as the structures undergo small deformations.

2.1.2 ANSYS MOR

The ANSYS MOR approach was developed by ANSYS with the objective to describe the static or dynamic responses of the mechanical system in a fast and accurate way [17].

ANSYS MOR was coupled to the CFD program ANSYS CFX. It is based on the mode-superposition method, which uses the natural frequencies and mode shapes generated from a modal analysis to characterize the dynamic response of a structure to transient or steady harmonic excitations [18]. With this method, the dynamic response of a structure can be approximated by a superposition of a particular number of its eigenmodes.

First, the general equations of motion are expressed as:

$$[M]\{\ddot{u}\} + C\{\dot{u}\} + [K]\{u\} = \{F\} \qquad (25)$$

where [M] is the structural mass matrix, [C] the structural damping matrix, [K] the structural stiffness matrix, $\{\ddot{u}\}$ the nodal acceleration vector, $\{\dot{u}\}$ the nodal velocity vector, $\{u\}$ the nodal displacement vector and $\{F\}$ the time-varying load vector. The time-varying load vector is defined as:

$$\{F\} = \{F_{nd}\} + s\{F^s\} \qquad (26)$$

where $\{F_{nd}\}$ represents the time-varying nodal forces, $\{F^s\}$ - the load vector, computed with a modal analysis; and s - the load vector scale factor. The nodal force F_i can be expressed as:

$$F_i = \int \Phi_i^T \vec{n} p_i da \qquad (27)$$

where Φ_i^T is a typical mode shape, $\vec{n}$ is the normal vector and p_i is the pressure of i^{th} node. The nodal displacement vector can be defined with a set of modal coordinates y_i as:

$$\{u\} = \sum_{i=1}^{n} \{\Phi_i\} y_i \qquad (28)$$

where $\{\Phi_i\}$ is the i^{th} mode shape, and n is the number of modes to be considered.

After several substitutions and further mathematical operations, the equation of motion of the modal coordinates is obtained:

$$\ddot{y}_i + 2\omega_i \xi_i \dot{y}_i + \omega_i^2 y_i = f_i \qquad (29)$$

where ξ_i is the fraction of critical damping for mode i and ω_i is its angular frequency.

Since *i* represents any mode, Eq. (29) denotes *n* uncoupled equations in the *n* unknowns y_i. The advantage of the uncoupled system is that all the computationally expensive matrix algebra has been done in the eigensolver, and long transients may be analyzed inexpensively in modal coordinates with Eq. (28). The y_i are converted back into geometric displacements (the system response to the loading) by using Eq. (28). That is, the individual modal responses are superimposed to obtain the actual response, and hence the name "mode-superposition" [18].

Equation (5) represents a reduced mechanical system and is implemented in ANSYS CFX - MOR code. Since it is a simplification of the mechanical system it is important to remember that FSI simulations with ANSYS CFX - MOR are subject to some restrictions. The approach is valid for cases with linear dynamics and this implies moderate

displacements, small strains, linear contacts and linear material behavior (no plasticity) [17].

2.2 Implementation of ANSYS CFX-MOR for a simplified test case

A simple test case was generated with the aim to implement the ANSYS MOR approach and compare it with the a full-order model (FOM), which is the coupled code ANSYS CFX – Mechanical.

2.2.1 Case setup

In the proposed test case, water at 25 °C flows across one cylinder in a narrow rectangular flow channel. As a result of the occurring vortex shedding phenomena, the cylinder starts to vibrate. Figure 17 shows the geometry of the case setup. The channel is 200 mm high, 30 mm wide and 70 mm long. The cylinder is 198 mm high and has a diameter of 7 mm. In the upper part of the cylinder monitor points are put to track its displacement in two (lift and drag) directions. The cylinder is firmly fixed in the bottom plate, while its top end is free: the latter is just 2 mm below the top channel wall and the cylinder wall about 10 mm away from the channel side walls.

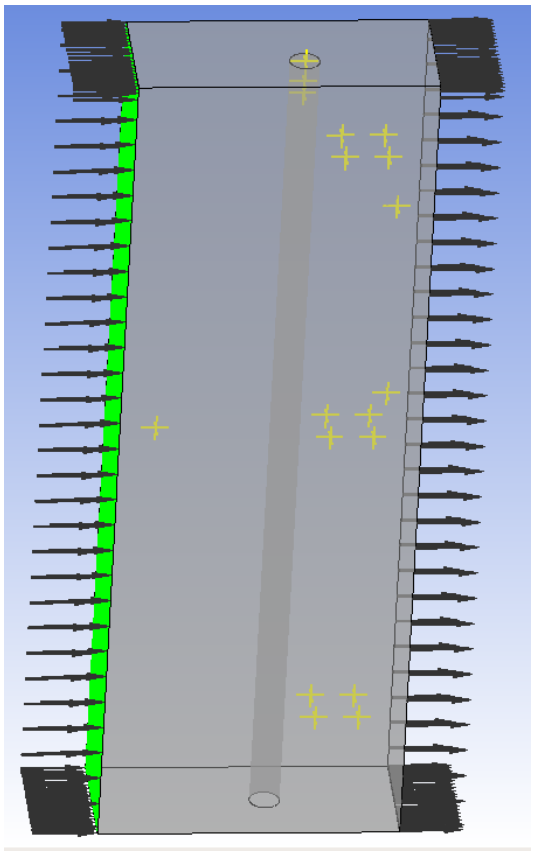

Figure 17: Narrow rectangular channel with cylinder inside exposed to a cross-flow.

2.2.2 Generation of the mechanical model and modal analysis

The geometry of the cylinder was imported in Mechanical. A tetrahedral mesh, consisting of approx. 0.2 M elements in total was generated. Figure 18 shows the numerical mesh of the first cylinder. *DISPLACEMENT* boundary conditions were used for the bottom end of the cylinder. This is not allowed to move, while no extra boundary conditions were applied at its top end, since this should freely move and experience the largest displacements, resulting from the vortex-shedding phenomenon. The material properties, provided by CEA for the AMOVI experiment, were used in this theoretical test case: the density of stainless tube is 8300 kg/m^3, the elasticity is 200 GPa and the Poisson ratio is 0.3.

With this configuration, a modal analysis was performed to calculate the eigenfrequency of the structure. The calculated first fundamental frequency of the cylinder is 113 Hz. For the validation of FSI simulations with ANSYS MOR the good agreement between simulation and measured experiment for the fundamental vibration frequency is of great importance. One should not expect to generate accurate results with the reduced order model if the first fundamental vibration frequency is not matching well the measured value.

It was decided to perform the modal analysis for the first six modes of vibration. In this particular case, the first vibration mode plays the most important role. Table 2 presents the calculated eigenfrequencies for the first six modes. Figure 19 shows the cylinder mode shapes for the first six vibration modes.

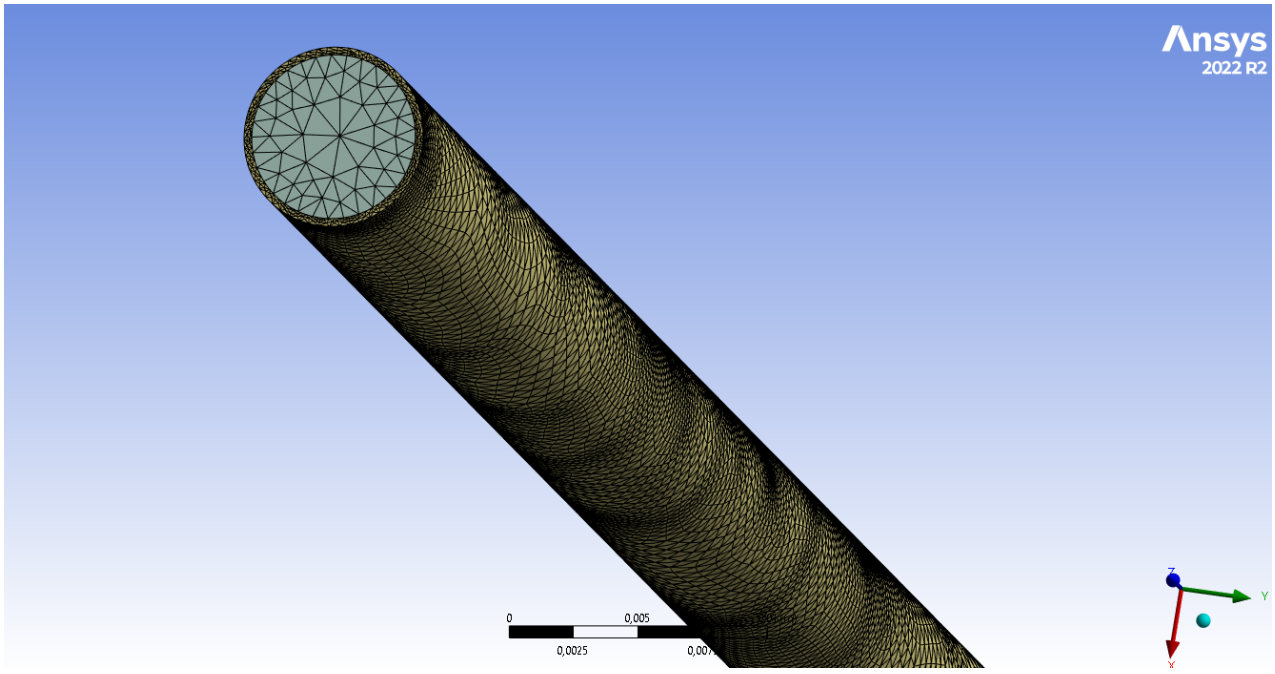

Figure 18: Tetrahedral mesh of the cylinder, generated in Mechanical

Table 2: Fundamental vibration frequencies of the cylinder

Mode	Frequency, [Hz]

First	113.01
Second	113.02
Third	856.19
Fourth	856.31
Fifth	2524.6
Sixth	2524.9

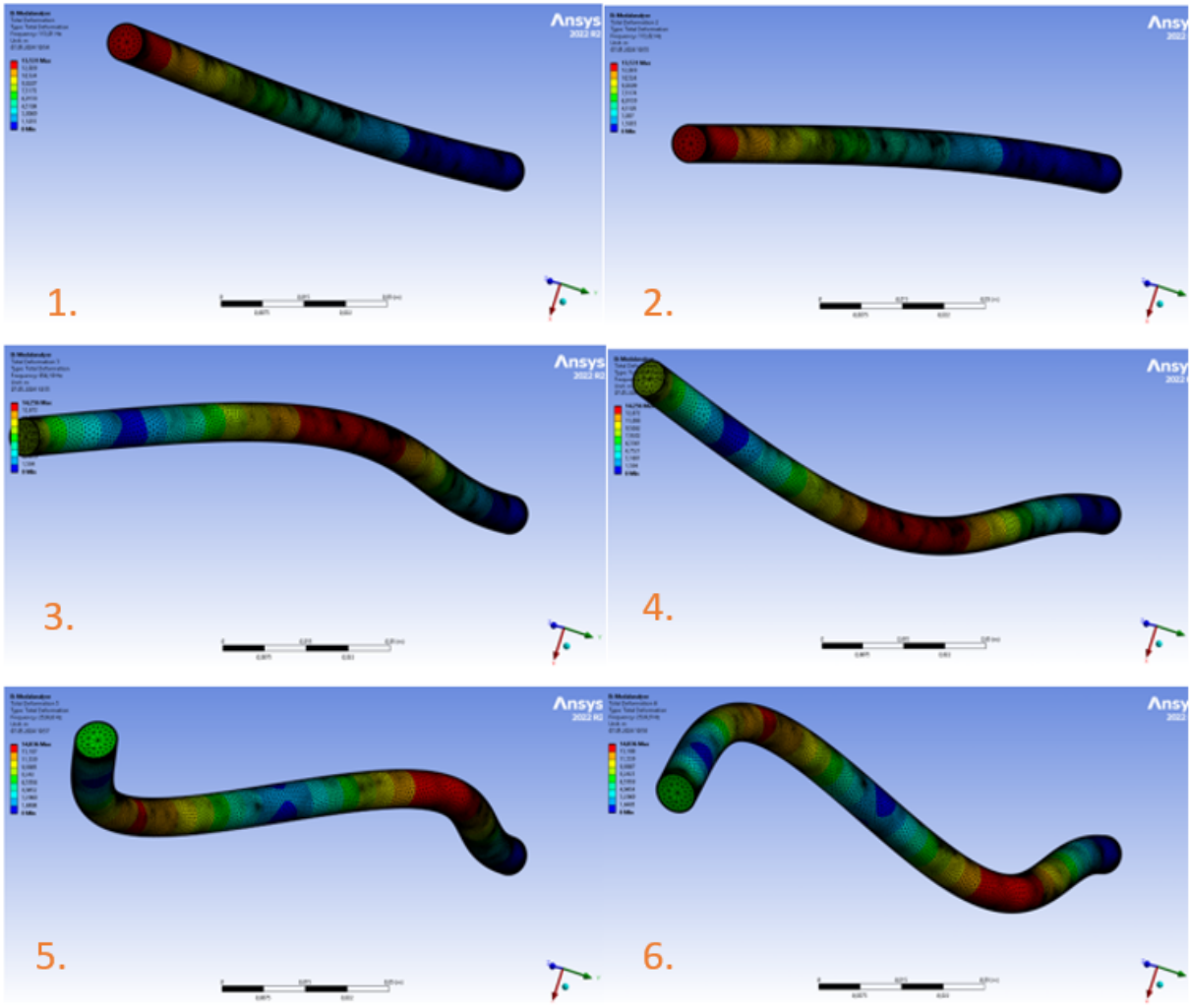

Figure 19: Cylinder mode shapes for the first six vibration modes.

2.2.3 Generation of the ANSYS CFX model and setup

The CFD domain comprises the channel and the outer surface of the cylinder. To carry out the analyses, a hexahedral grid was generated. Mesh studies were not performed, since the same mesh was used for the reduced-order and full-order model computations. Nevertheless, the generated grid was relatively fine and with very high quality, because the

Zonal LES (ZLES) was used. The maximal aspect ratio is 33, the expansion factor is 12 and the minimum orthogonality angle (important for the solver convergence), is significantly larger (42°) than the recommended minimum value of 20° in the OECD/NEA Best Practice Guidelines for the Use of CFD in Nuclear Reactor Safety Applications [19]. The final computational mesh, used for the ANSYS CFX-Mechanical simulations, consisted of 3 million elements (Figure 20). The mesh structure was also created according to the ZLES turbulence model requirements in ICEM CFD: the mesh around the cylinder (LES zone) is fine, while in the URANS region a coarser mesh was used. The flow simulations were carried out with a "High-Resolution" advection scheme, the time discretization was carried out with a second-order scheme.

The CFD simulations are isothermal since all experiments were performed at a constant temperature of 25 °C. At the channel inlet a mass flow rate of 2.78 kg/s was specified along with medium turbulence intensity. At the outlet, constant pressure was applied. The chosen time step size of 2.2×10^{-4} s resulted in a CFL ~0.53. The convergence criteria for the CFD solver were set to RMS $<10^{-5}$.

Two simulations were performed: a full-order model (FOM) and a reduced-order model (MOR). Both simulations had the same fluid domains. The structural models used for the FOM and the modal analysis were based on the same mesh and boundary conditions. The FOM calculation was performed with the System Coupling (SYSC) service, which is part of ANSYS tools. In the FOM calculation, 3 staggered iterations per time step were carried out, this means that ANSYS CFX and Mechanical exchanged results three times within each time step. This number proved to be sufficient for the convergence of the FSI run. In the MOR simulation, data exchange takes place at the end of the time step.

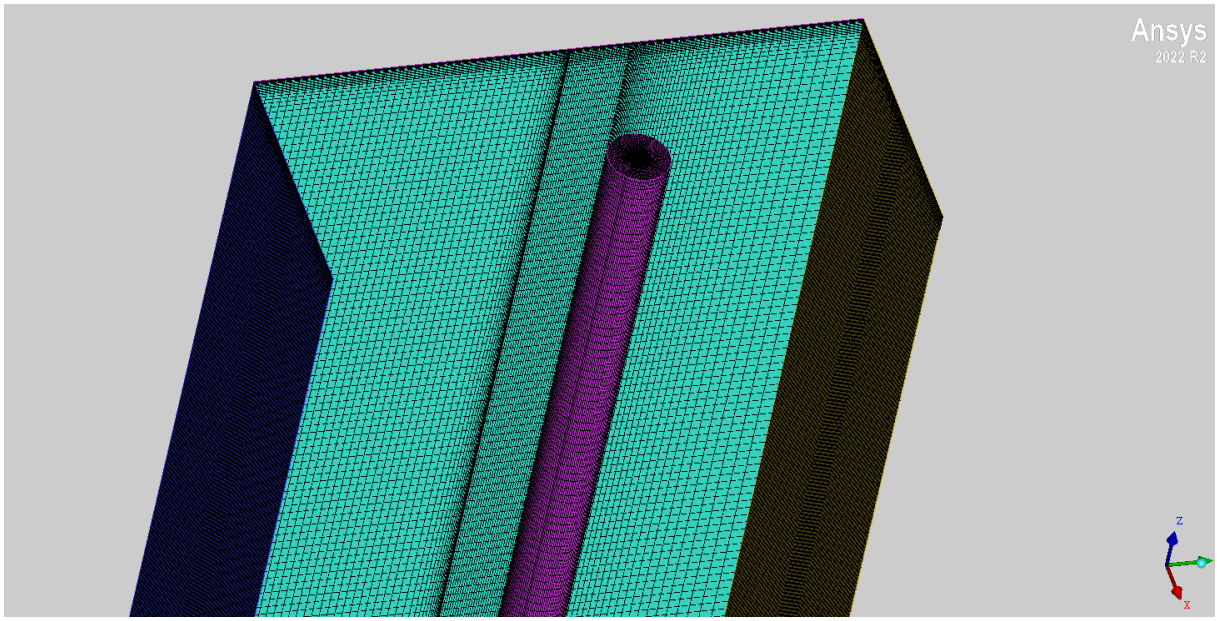

Figure 20: Hexahedral mesh representing the flow channel.

2.2.4 Generation and implementation of the MOR model in ANSYS CFX

As already mentioned before, a modal analysis with 6 modes was performed with the cylinder to obtain the fundamental vibration mode shapes and frequencies. Six files were generated, and these were used as an input for the MOR approach in the ANSYS CFX-MOR calculation. These files contain the fundamental frequency for each vibration mode together with the initial X, Y, Z coordinates and the total mesh displacement for each node of the defined FSI interface (see Figure 21). In the current case, the FSI interface comprises the side and top cylinder surfaces.

```
[Name]
WallFluid01

[Parameters]
Ncompt = 3
Nnodes = 11206
Mass = 1.35814579E-002 [kg]
Frequency = 113.00616 [Hz]
Maximum Displacement = 13.531087 [m]

[Spatial Fields]
Initial X [m], Initial Y [m], Initial Z [m]

[Data]
Initial X [m], Initial Y [m], Initial Z [m], meshdisptot x [m], meshdisptot y [m], meshdisptot z [m], node
 1.45959014E-002,  0.34764627  ,  0.21800000  ,  -9.1568372  ,  9.9562155  ,  0.14223669  ,  15477
 1.42455714E-002,  0.34689020  ,  0.21800000  ,  -9.1568372  ,  9.9562156  ,  0.17337039  ,  15482
 1.48477379E-002,  0.34680362  ,  0.21800000  ,  -9.1568373  ,  9.9562156  ,  0.21932454  ,  15483
 1.74053328E-002,  0.34994886  ,  0.21800000  ,  -9.1568372  ,  9.9562146  ,  0.16242097  ,  15493
 1.70439427E-002,  0.34874663  ,  0.21800000  ,  -9.1568375  ,  9.9562150  ,  0.22484110  ,  15494
 1.67729589E-002,  0.34949467  ,  0.21800000  ,  -9.1568372  ,  9.9562149  ,  0.15327818  ,  15495
 1.74270205E-002,  0.34916410  ,  0.21800000  ,  -9.1568374  ,  9.9562148  ,  0.22016586  ,  15496
 1.75153699E-002,  0.34802189  ,  0.21800000  ,  -9.1568377  ,  9.9562150  ,  0.30796025  ,  15551
 1.78442734E-002,  0.34853368  ,  0.21800000  ,  -9.1568377  ,  9.9562148  ,  0.29294214  ,  15552
 1.34420380E-002,  0.34810546  ,  0.21800000  ,  -9.1568371  ,  9.9562155  ,  3.31342764E-002,  15591
 1.31438179E-002,  0.34739336  ,  0.21800000  ,  -9.1568371  ,  9.9562155  ,  6.45518256E-002,  15592
 1.26840511E-002,  0.34779175  ,  0.21800000  ,  -9.1568371  ,  9.9562154  ,  5.62046398E-003,  15593
 1.41740459E-002,  0.34823264  ,  0.21800000  ,  -9.1568371  ,  9.9562155  ,  7.23180401E-002,  15594
 1.38818301E-002,  0.34756464  ,  0.21800000  ,  -9.1568371  ,  9.9562155  ,  0.10096773  ,  15595
 1.69205841E-002,  0.35116525  ,  0.21800000  ,  -9.1568366  ,  9.9562147  ,  4.31425788E-002,  15658
 1.74955672E-002,  0.35066819  ,  0.21800000  ,  -9.1568369  ,  9.9562145  ,  0.11675833  ,  15659
 1.65473250E-002,  0.35022298  ,  0.21800000  ,  -9.1568369  ,  9.9562149  ,  8.61243309E-002,  15660
 1.27407903E-002,  0.35065668  ,  0.21800000  ,  -9.1568368  ,  9.9562157  ,  -0.19621857  ,  15690
 1.18578282E-002,  0.35060560  ,  0.21800000  ,  -9.1568350  ,  9.9562151  ,  -0.25082749  ,  15691
 1.20292226E-002,  0.35118932  ,  0.21800000  ,  -9.1568348  ,  9.9562148  ,  -0.28140032  ,  15692
 1.34295972E-002,  0.35183265  ,  0.21800000  ,  -9.1568367  ,  9.9562158  ,  -0.23514502  ,  15693
 1.36297280E-002,  0.35092371  ,  0.21800000  ,  -9.1568369  ,  9.9562156  ,  -0.15671232  ,  15694
 1.28643175E-002,  0.35137405  ,  0.21800000  ,  -9.1568368  ,  9.9562159  ,  -0.23954359  ,  15695
 1.31438179E-002,  0.35260664  ,  0.21800000  ,  -9.1568366  ,  9.9562160  ,  -0.30954653  ,  15697
 1.26840511E-002,  0.35220825  ,  0.21800000  ,  -9.1568368  ,  9.9562160  ,  -0.31130204  ,  15698
 1.46533300E-002,  0.35239443  ,  0.21800000  ,  -9.1568363  ,  9.9562156  ,  -0.19469468  ,  15710
```

Figure 21: Input file for the ANSYS CFX-MOR simulation

In a next step, the MOR model was built and integrated in the ANSYS CFX input deck. This was done with the help of CEL (CFX Expression Language) expressions. Additional variables and expressions are generated for the fluid forces acting on the FSI interface surface, the nodal displacements, the nodal velocities, etc. To calculate the displacement of each node of the FSI surface in X, Y and Z directions, the information provided in the six MOR input files (Figure 21 shows the one for the first vibration mode) is used as six field functions, containing the total mesh displacements from the modal analysis. This information in conjunction with the method of mode-superposition is utilized for the calculation of the three displacement components in X, Y, Z directions, which are provided to the FSI interface surface in ANSYS CFX (Figure 22). The CFD code calculates the new mesh and then performs with the new, deformed mesh its simulation, generating new results for the updated pressure distribution on the FSI surface. This data is then passed back to the MOR, which provides the new nodal displacements to ANSYS CFX. User Defined Routines are called at the end of each time step to store the calculated data, which is also used for the computations in the next time step.

```
mq DISPX = \
  mqpos01new*mqDISPX01+mqpos02new*mqDISPX02+mqpos03new*mqDISPX03+mqpos0\
  4new*mqDISPX04+mqpos05new*mqDISPX05+mqpos06new*mqDISPX06
mq DISPX Wall = mq \
  DISPX*if(citern>0,SetHistory(mqpos01new,mqpos02new,mqpos03new,mqpos04\
  new,mqpos05new,mqpos06new,mqvel01new*1[s],mqvel02new*1[s],mqvel03new*\
  1[s],mqvel04new*1[s],mqvel05new*1[s],mqvel06new*1[s]),1.0)
mq DISPY = \
  mqpos01new*mqDISPY01+mqpos02new*mqDISPY02+mqpos03new*mqDISPY03+mqpos0\
  4new*mqDISPY04+mqpos05new*mqDISPY05+mqpos06new*mqDISPY06
mq DISPY Wall = mq \
  DISPY*if(citern>0,SetHistory(mqpos01new,mqpos02new,mqpos03new,mqpos04\
  new,mqpos05new,mqpos06new,mqvel01new*1[s],mqvel02new*1[s],mqvel03new*\
  1[s],mqvel04new*1[s],mqvel05new*1[s],mqvel06new*1[s]),1.0)
mq DISPZ = \
  mqpos01new*mqDISPZ01+mqpos02new*mqDISPZ02+mqpos03new*mqDISPZ03+mqpos0\
  4new*mqDISPZ04+mqpos05new*mqDISPZ05+mqpos06new*mqDISPZ06
mq DISPZ Wall = mq \
  DISPZ*if(citern>0,SetHistory(mqpos01new,mqpos02new,mqpos03new,mqpos04\
  new,mqpos05new,mqpos06new,mqvel01new*1[s],mqvel02new*1[s],mqvel03new*\
  1[s],mqvel04new*1[s],mqvel05new*1[s],mqvel06new*1[s]),1.0)
```

Figure 22: CEL expressions for the displacements in X, Y, Z directions, provided to ANSYS CFX for the calculation of the new, deformed mesh.

2.3 Results and comparison between FOM and ROM

2.3.1 Flow pattern

Figure 23 shows the velocity distribution in the test channel, calculated by ANSYS CFX-MOR. The mean velocity in front of the cylinder is around 0.46 m/s with Re~1.55x10^4. Zones with higher and lower velocities develop around the cylinder, since the vertical structure leads to local flow acceleration and deceleration. Zones with different pressure levels form on the cylinder's surface that disturb the local boundary layers. The phenomenon leads to local boundary layer detachment that causes the formation of the vortices. These vortices detach from the cylinder surface and stimulate its vibration. The maximal local velocity reached is 0.86 m/s and is found in the small gap between the top cylinder surface and the top channel wall. One can also clearly see the interface between RANS and LES region upstream the cylinder.

Figure 24 shows with the help of velocity vectors flow acceleration, deceleration and recirculation zones as well as formation of von Karman vortex street behind the cylinder. Local negative flow velocities down to -0.2 m/s are observed in the recirculation zones that form behind the cylinder. The observed flow pattern is typical for cylinders exposed to a cross-flow.

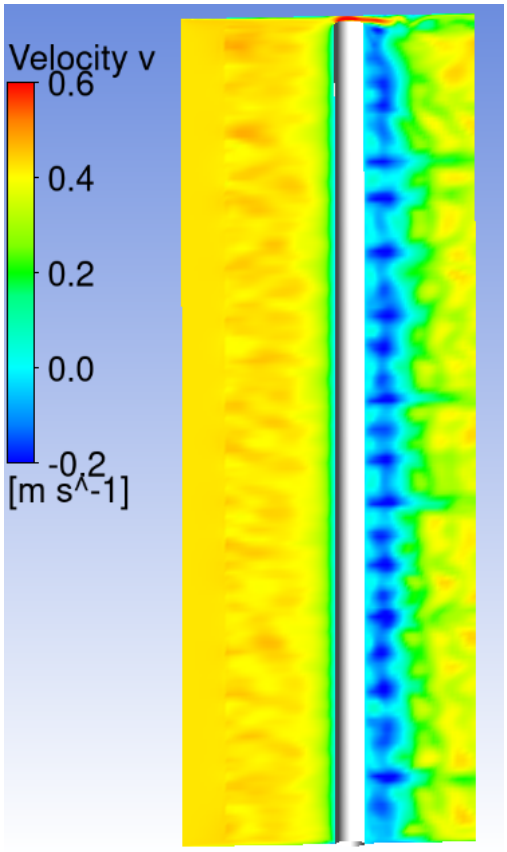

Figure 23: Streamwise velocity distribution in the flow channel.

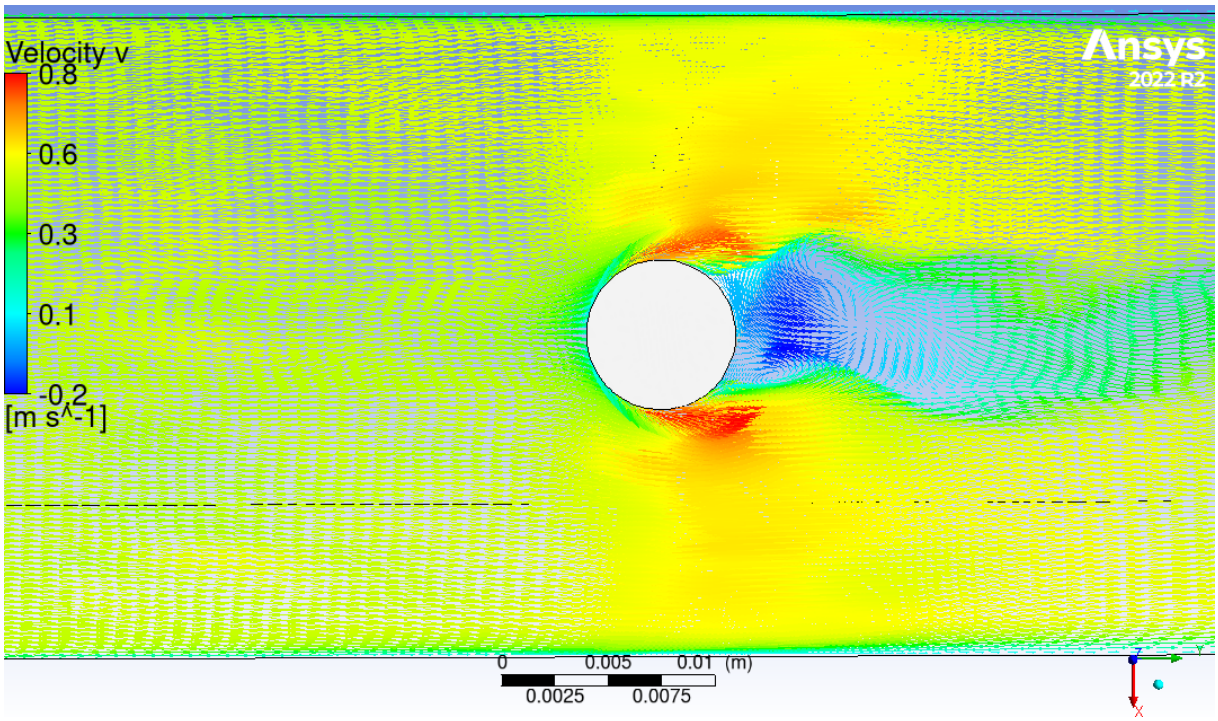

Figure 24: Velocity vectors in XY plane showing flow acceleration, deceleration and recirculation zones as well as the formation of von Karman vortex street behind the cylinder.

Funded by
the European Union

2.3.2 Vibration analysis

The cylinder displacement in transverse (lift) direction, measured at the top of the cylinder, is shown in Figure 25. The first 0.3 s are omitted, in order to exclude the transient phase at the beginning of the coupled calculations. Although not identical, the displacements look similar. By building the RMS values of both signals over the entire simulation time (excluding the first 0.3 s), the following values are obtained:

- System coupling (FOM) RMS displacement = 1.64e^{-6} m
- ANSYS CFX-MOR (ROM) RMS displacement = 1.77e^{-6} m

The ROM overestimates the RMS displacement, predicted by the FOM, by 8%, which can be considered as a good approximation. In this particular case, the ROM appears to provide conservative results.

Figure 25 and Figure 26 show the calculated APSD of the displacements using an FFT analysis. It can be seen that both approaches agree on the same vortex-shedding frequency from the cylinders' surfaces, which is 18.9 Hz.

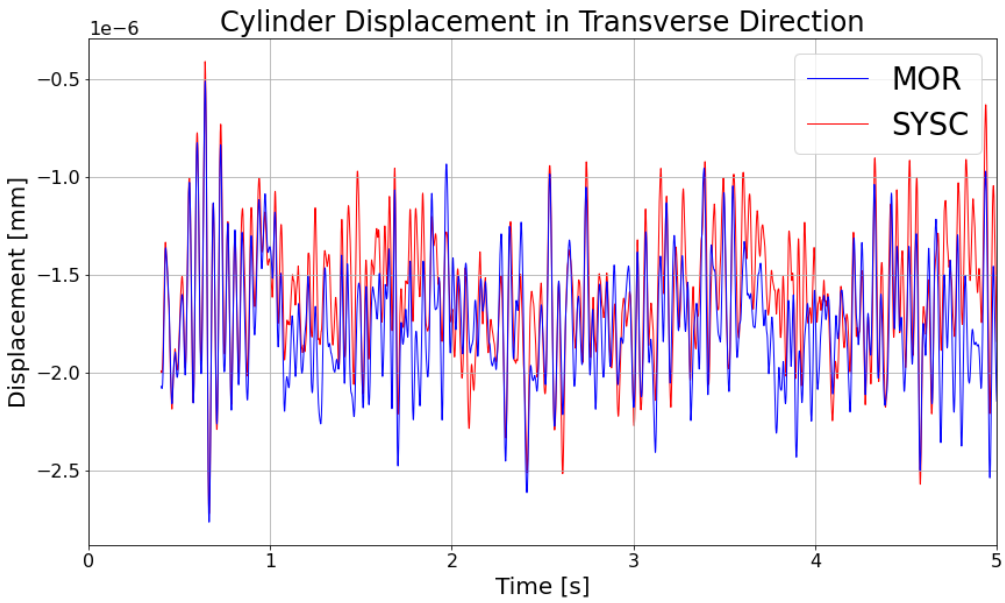

Figure 25: Cylinder displacement in transverse (lift) direction, calculated with full-order and reduced-order FSI models.

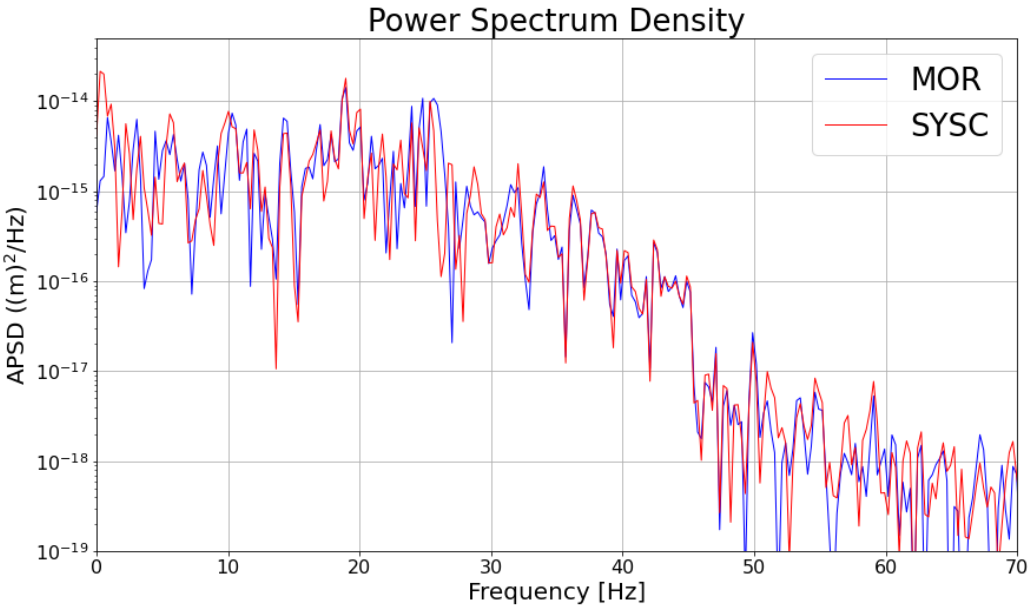

Figure 26: Power spectral density, based on the calculated time-dependent displacements.

2.3.3 Efficiency comparison

The comparison of the analysis efficiency is based on the consumed wall-clock time. Both simulations were performed on 24 parallel cores, distributed on two nodes. The cores were of type Intel(R) Xeon(R) Gold 5220R CPU @ 2.20GHz. The parallelization was realized with Intel MPI, the cluster was equipped with InfiniBand. The simulation with the FOM took 22.8 days, while the one with the ROM – 4.6 days. The advantage of the fast-running method, based on structural ROM is obvious: it is a approx. a factor of 5 faster than the reference FOM. The following has to be considered:

- Although both CFD domains are the same, the higher wall-clock time required by the FOM mainly results from the staggered iterations between ANSYS CFX and Mechanical (3x3 CFX iterations in one time step). In the ROM case, both codes exchange data once after each time step (explicit coupling), which results in totally 3 CFX iterations per time step.

- It is clear that the wall-clock time needed by Mechanical in the FOM calculation also contributes to the total increase of the FOM computational time. However, the higher number of CFX iterations in the FOM case has a stronger impact on the total wall-clock time.

- In the full coupling with SYSC, 90% of the cores are reserved for the CFD process and the rest – for the CSM process. This means that less cores are used for the CFD solution. The user is free to specify how many cores to be used by each code. In the

ROM case, all cores are used by the CFD process. The MOR routines are executed on the master core at the end of each time step.

- Test calculations with higher number of modes (up to 12) showed increase in the CPU time, which is not remarkable. The results did not change, since the influence of the higher modes is negligible in this simulation. This might be different in cases with configurations with multiple vibrating structures (e.g. fuel assembly with many vibrating rods).

- Modal analysis with finer structural grids would lead to larger input files for the MOR approach, thus increasing the CPU time. Still, the CPU time needed by the MOR is negligible in comparison to the one consumed by the CFD code. Therefore, finer grids of the vibrating structure do not remarkably affect the overall wall-clock time of the ANSYS CFX-MOR run.

2.4 Conclusions and further steps

This chapter is dedicated the MOR approach, developed by ANSYS. It first introduced the approach, based on the method of mode-superposition. Further, its implementation for a simplified FIV test case was described. To check the advantages of this method over the FOM, a comparative analysis has been performed. It showed increased efficiency of the ROM method against the original FOM: the wall-clock time of the fast-running method was approx. a factor of five smaller. The accuracy in terms of vibration frequency was perfect, while a small overestimation of the RMS amplitudes by the ROM was observed.

It can be concluded that ANSYS MOR is a promising fast-running method that can provide comparable results to the ones generated with the FOM at a significantly lower computational cost. Further comparative analyses are necessary in order to fully assess the ROM performance. It should be tested for larger systems in terms of mesh elements as well as for ones with multiple vibrating components (e.g. multiple vibrating tubes rods in a tube bundle).

3. Development and application of the Synthetic Turbulence procedure in fast-running FSI

This section describes the main approaches that are used by IPP for one-directional and two-directional FSI, taking into account the reconstruction of the turbulent pulsation field. The main criterion for selecting the used approaches is their speed and sufficient accuracy for engineering practice.

3.1 Introduction

The factual picture of the turbulent pulsation field is generally anisotropic, chaotic in nature and is determined by many geometrical and physical factors. There are two methods to solve such a problem.

The first method is to experimentally study the characteristics of the contact problem between a medium and a wall [20] (using special probes). The general results of such studies are the integral force and resistance coefficients, which take into account both the viscous component and the turbulent effect on the studied wall [21]. This approach is individual and allows one to disseminate the results only within the framework of similarity theory.

The second method is to use computational fluid dynamics. It is believed that the use of DNS methods is capable of completely predicting the real pulsation pattern and giving results that can be selected as reference (in other words, close to the experiment). To date, fundamental research related to turbulence and exchange processes in the boundary layer is carried out only for relatively simple geometries [22]. In relation to practical problems, scale-resolving approaches (SRS) are used, based on turbulence models, which inherently predict the energy spectrum of pulsations. Experience in using such approaches indicates the correct prediction of pulsations not only in the volume, but also on the solid body surface [23]. In general, a number of international test problems indicate the consistency of the SRS method for a whole range of problems in which the target characteristic (for example, the mixing scalar) largely depends on the quality of turbulence prediction [24]. The use of the SRS method requires significant computing resources. Obviously, the process is considered to be exclusively non-stationary (the definition of turbulence as such), therefore, the total duration of the calculation is affected by the initialization. In some cases, incorrect initial conditions (in the sense of being “far” from the true flow pattern, for example, initialization without a pulsation field) can lead to the fact that starting to simulate the “true” flow pattern can take up to 50% of the entire calculation. This circumstance significantly complicates the practical application of this method. The use of initialization using the RANS approach somewhat reduces the recovery time, which allows, at best, to spend up to 20% of the time on restoring the pulsation component.

A modern approach is the creation of a special procedure for reconstructing the pulsation field based on synthetic turbulence [25,43], which, based on RANS, generates a physically based field of turbulent pulsations and is the initial condition for SRS methods. Experience shows that in most cases the generated field is "close" to what is set using only the RANS - SRS approach [26].

For example, on the scale of pressurized water reactors (PWR) , the use of the SRS approach is still very computationally expensive, considering the fact that only some fragments of the internals and reactor pressure vessel (RPV) surfaces are of interest. In this regard, a special procedure for reconstructing the velocity pulsation field based on a synthetic turbulence generator was developed, which is used in conjunction with CFD modeling with the RANS/URANS approach. The results obtained can subsequently serve as a good initialization for CFD calculations using SRS (LES, Detached Eddy Simulation (DES), Scale-Adaptive Simulation (SAS)).

When performing a coupled FSI analysis (one/bi-directional), synthetic pulsations can be taken into account when calculating the corresponding force factors. In this case, a simplified URANS model of turbulence transfer of eddy viscosity is used, which is obtained by combining the equations for the transfer of turbulence kinetic energy and its dissipation, obtained within the framework of the RNG theory.

3.2 One-equation RNG turbulence model

Currently, there is a wide variety of turbulence models of various parametrics, which are widely used both in commercial application software packages, such as ANSYS Fluent,CFX, etc., and in proprietary codes. Herewith, the problem of choosing one or another turbulence model arises. Quite often, when calculating complex flows, a two-parameter RNG *k*-ε model is used. Besides this, empirical one-parameter models with one additional equation are also applied. The presence of only one additional equation (compared to two-parameter ones) speeds up and simplifies the calculation procedure due to a possible loss of calculation accuracy. One of these is a model that contains an additional equation for effective viscosity. Such an empirical model was first proposed in the works [27,28]. Later, a similar empirical model was developed [29,30]. The mentioned models include a number of empirical coefficients and terms, which is their drawback. The one-parameter model of effective viscosity and thermal diffusivity proposed below does not include these coefficients and is based on the RNG *k*-ε model. The main equation of this model [31] of variable effective viscosity has the following final form:

$$\frac{\partial \nu}{\partial \mathrm{t}}+u\frac{\partial \nu}{\partial \mathrm{x}}+v\frac{\partial \nu}{\partial \mathrm{y}}+w\frac{\partial \nu}{\partial \mathrm{z}}=\frac{\partial}{\partial \mathrm{x}}\left(\frac{\nu}{\mathrm{Pr}_K}\frac{\partial \nu}{\partial \mathrm{x}}\right)+\frac{\partial}{\partial \mathrm{y}}\left(\frac{\nu}{\mathrm{Pr}_K}\frac{\partial \nu}{\partial \mathrm{y}}\right)+\frac{\partial}{\partial \mathrm{z}}\left(\frac{\nu}{\mathrm{Pr}_K}\frac{\partial \nu}{\partial \mathrm{z}}\right)+$$
$$+\sqrt{C_v^3}(C_{1\varepsilon}^*+C_{2\varepsilon})S\nu_t-\frac{4C_v^3\nu^2}{S^2\mathrm{Pr}_K}\left(\frac{\partial S}{\partial \mathrm{x}}\right)^2-\frac{4C_v^3\nu^2}{S^2\mathrm{Pr}_K}\left(\frac{\partial S}{\partial \mathrm{y}}\right)^2-\frac{4C_v^3\nu^2}{S^2\mathrm{Pr}_K}\left(\frac{\partial S}{\partial \mathrm{z}}\right)^2 \qquad (30)$$

Where ν,ν_t – effective and turbulent viscosity, respectively; u,v,w – velocity projections onto the corresponding axes of the Cartesian coordinate system; Pr_K – the Prandtl number of kinetic energy of turbulence, which can be obtained from the solution (31) of the differential equation, which is similar to the equation of the form (32).

$$\left|\frac{\mathrm{Pr}_K^{-1}-c}{1-c}\right|^{\frac{c+1}{c+b}}\left|\frac{\mathrm{Pr}_K^{-1}+b}{1+b}\right|^{\frac{b-1}{c+b}}=\frac{\nu_0}{\nu_t} \qquad (31)$$

$$\frac{\partial \mathrm{Pr}_t^{-1}}{\partial \tau} = \frac{1}{\nu}\frac{\partial \nu}{\partial \tau}\left(\frac{d-1}{d}\widetilde{A}_d \frac{1}{1+\mathrm{Pr}_t^{-1}} - \mathrm{Pr}_t^{-1}\right) \tag{32}$$

Where coefficients $c = \frac{1}{2}\left(\sqrt{4\frac{d-1}{d}\tilde{A}_d{}^{-1}+1}-1\right)$, $b = \frac{1}{2}\left(\sqrt{4\frac{d-1}{d}\tilde{A}_d{}^{-1}+1}+1\right)$ and $\tilde{A}_d = \frac{d-1}{2(d+2)}$ in which parameter d defines the dimension of the problem to be solved. For three-dimensional space ($d = 3$) coefficients c and b are equal to 1.3929 and 2.3929 respectively. In a fully developed turbulent flow, the Prandtl number is equal $\mathrm{Pr}_K = 1/1.329 = 0.7179$.

Coefficient C_ν, that relates parameters RNG k-ε turbulence model and turbulent viscosity in general, can be found according to the relationship:

$$C_\nu = \frac{2}{3C_K^2}\left(\gamma\frac{\widetilde{A}_d}{9}\right)^{1/3} \tag{33}$$

Where C_K – Kolgomorov constant, which can be found from the relation:

$$C_K = 1.488 \cdot \gamma^{1/6} \tag{34}$$

The value of the constant γ, which is determined theoretically on the basis of the turbulence energy balance equation for the inertial range [32,33] for the renormalization one-parameter turbulence model is equal to 1.575, then the value of the constant $C_\nu = 0.0847$. The value of the constant $C_{2\varepsilon}$ in equation (30) is equal to 1.68, and the value of the coefficient $C_{1\varepsilon}^*$ is found according to the dependence:

$$C_{1\varepsilon}^* = C_{1\varepsilon} - \frac{\eta_\varepsilon}{1+\beta_\varepsilon \cdot \eta_\varepsilon^3}\left(1-\frac{\eta_\varepsilon}{\eta_{\varepsilon 0}}\right) \tag{35}$$

Where the parameter values are: $C_{1\varepsilon} = 1.42$, $\beta_\varepsilon = 0.014$ and $\eta_\varepsilon = 1/\sqrt{C_\nu}$, and parameter $\eta_{\varepsilon 0}$ is determined by the expression:

$$\eta_{\varepsilon 0} = \sqrt{\frac{C_{2\varepsilon}-1}{(C_{1\varepsilon}-1)C_\nu}} \tag{36}$$

Based on the values of the coefficients that are included in (35), the parameter $C_{1\varepsilon}^* = 0.950825$. In general, the theoretical value of the constant γ may differ from those accepted above, depending on the method used, from those presented in the references [34,35]. The values of the coefficients that are included in equation (30) depending on the model adopted for calculating the constant γ, are summarized in Table 3.

Table 3: The values of the constants included in equation (30), depending on the adopted approach to γ calculation

Reference	C_K	C_v	γ	β_ε	$C^*_{1\varepsilon}$
[32,33]	1.605	0.0847	1.575	0.014	0.950825
[34]	1.436	0.1	4/3	0.027	1.054790
[35]	1.667	0.08	5/3	0.011	0.910666

The last parameter S is determined according to the dependence:

$$S = \sqrt{2 \cdot \left\{ \left(\frac{\partial u}{\partial x}\right)^2 + \left(\frac{\partial v}{\partial y}\right)^2 + \left(\frac{\partial w}{\partial z}\right)^2 \right\} + \left(\frac{\partial u}{\partial y} + \frac{\partial v}{\partial x}\right)^2 + \left(\frac{\partial u}{\partial z} + \frac{\partial w}{\partial x}\right)^2 + \left(\frac{\partial v}{\partial z} + \frac{\partial w}{\partial y}\right)^2} \quad (37)$$

3.3 Synthetic Turbulence Generation Procedure

In general, the velocity field can be represented as a superposition of the averaged velocity and the pulsation component:

$$\{u(r,t), v(r,t), w(r,t)\} = \{U(r), V(r), W(r)\} + \{u'(r,t), v'(r,t), w'(r,t)\} \quad (38)$$

where U, V, W – average velocity, u', v' , w'- pulsation component.

Next, we introduce the concept of a model field of velocity pulsations [36,37], for which the following relations are valid:

- The expected value of each component is zero $M(u_i^*) = 0$.
- The expected value of the product of components (second moment) is equal to the Kronecker symbol $M(u_i^*, u_j^*) = \delta_{ij}$.

The true velocity pulsation field is connected to the model one through a scaling matrix:

$$\begin{pmatrix} u'(r,t) \\ v'(r,t) \\ w'(r,t) \end{pmatrix} = [A] \begin{pmatrix} u^*(r,t) \\ v^*(r,t) \\ w^*(r,t) \end{pmatrix} \quad (39)$$

The scaling matrix $[A]$ must depend on the energy characteristic, which is calculated using RANS. In the general case, when taking into account the anisotropy of the flow, for example, using Reynolds stress models (40) the matrix $[A]$ must satisfy the expansion $[R] = [A][A]^T$.

$$[R] = \begin{pmatrix} -\rho_0\langle u'u' \rangle & -\rho_0\langle v'u' \rangle & -\rho_0\langle w'u' \rangle \\ -\rho_0\langle v'u' \rangle & -\rho_0\langle v'v' \rangle & -\rho_0\langle w'v' \rangle \\ -\rho_0\langle u'w' \rangle & -\rho_0\langle v'w' \rangle & -\rho_0\langle w'w' \rangle \end{pmatrix} \quad (40)$$

Funded by
the European Union

In fact, the RANS approach models the entire spectrum, or rather the integral of the spectral density of kinetic energy over wave numbers. In this case, the Reynolds stress tensor has a diagonal form, and can be represented as the product of the unit matrix and a vector with coordinates in the form of double the turbulence kinetic energy [38]. Thereby, $\sqrt{R_{11}} = \sqrt{R_{22} - A_{21}^2} = \sqrt{R_{33} - A_{31}^2 - A_{32}^2} = \sqrt{\frac{2}{3}k_t(r)}$, $k_t(r)$ - turbulence kinetic energy. It is worth noting that the empirical constants included in the terms,contributors to the process of kinetic energy transfer, are calibrated on the basis of experimental data in such a way as to correctly reproduce the integral value (Figure 27).

$$[A] = \begin{pmatrix} \sqrt{R_{11}} & 0 & 0 \\ \frac{R_{21}}{\sqrt{R_{11}}} & \sqrt{R_{22} - A_{21}^2} & 0 \\ \frac{R_{31}}{\sqrt{R_{11}}} & \frac{R_{32} - A_{21}A_{31}}{A_{22}} & \sqrt{R_{33} - A_{31}^2 - A_{32}^2} \end{pmatrix} \quad (41)$$

The generation of velocity pulsations $\{u', v', w'\}$ is reduced to the generation of a field $\{u^*, v^*, w^*\}$, which is represented in the form of amplitude-modulated Fourier modes. Then, taking into account (39) and the diagonal pulsation stress tensor, the field $\{u', v', w'\}$ can be represented in vector form:

$$\vec{u}'(\vec{r}, t) = 2\sqrt{k_t(\vec{r})} \sum_{n=1}^{N} \sqrt{q_n(\vec{r})} \left(\vec{\sigma}_n cos\left[k_n \vec{d}_n \vec{r} + \varphi_n + s_n \frac{t}{\tau} \right] \right) \quad (42)$$

where, N - number of series terms (number of modes); $q_n(\vec{r})$ - normalized amplitude of one mode, which is determined by the local von Kármán turbulence energy spectrum; k_n - mode wave vector module number *n*; $\vec{\sigma}_n$ - unit vector, which determines the direction of the velocity mode number *n* (actually defines velocity projections); $\vec{d}_n$- unit vector, which determines the direction of the wave number (uniformly distributed over the unit sphere); φ_n - phase of the nth velocity mode; s_n - dimensionless circular frequency; τ - global time scale.

The dimensionless energy spectrum of turbulence [39] taking into account empirical corrections for spectrum distortion near the Kolmogorov scale of turbulence, can be represented in the form (43). The equation (43) considers the rapid drop in the energy spectrum near the wall (Figure 27), which corresponds to large dissipation near the boundary layer (flow laminarization) and the tendency of the turbulence kinetic energy to zero (laminarization as it approaches the wall).

$$E(k) = \frac{\left({}^{k}/_{k_e}\right)^4}{\left[1 + 2.4\left({}^{k}/_{k_e}\right)^2\right]^{17/6}} exp\left(-\left[12\frac{k}{k_\eta} \right]^2 \right) exp\left(-\left[\frac{4\max(k - 0.9k_{cell}, 0)}{k_{cell}} \right]^3 \right) \quad (43)$$

where, k - wave number module, k_e - wave number corresponding to the most energy-carrying vortices of the synthetic turbulence field, k_η - wave number corresponding

to the Kolmogorov scale of turbulence, k_{cell}- maximum resolved wave number on the computational mesh.

To determine the wave number corresponding to the most energy-carrying vortices, the following relation can be used:

$$k_e = \frac{2\pi}{min\left[2d_{wall}, {}^{3\sqrt{k_t}}/_{0.09 \cdot \omega_t}\right]} \tag{44}$$

where, d_{wall} - minimum distance from the point under consideration to a solid wall, k_t - specific value of kinetic energy of turbulence, ω_t - specific rate of kinetic energy dissipation into heat.

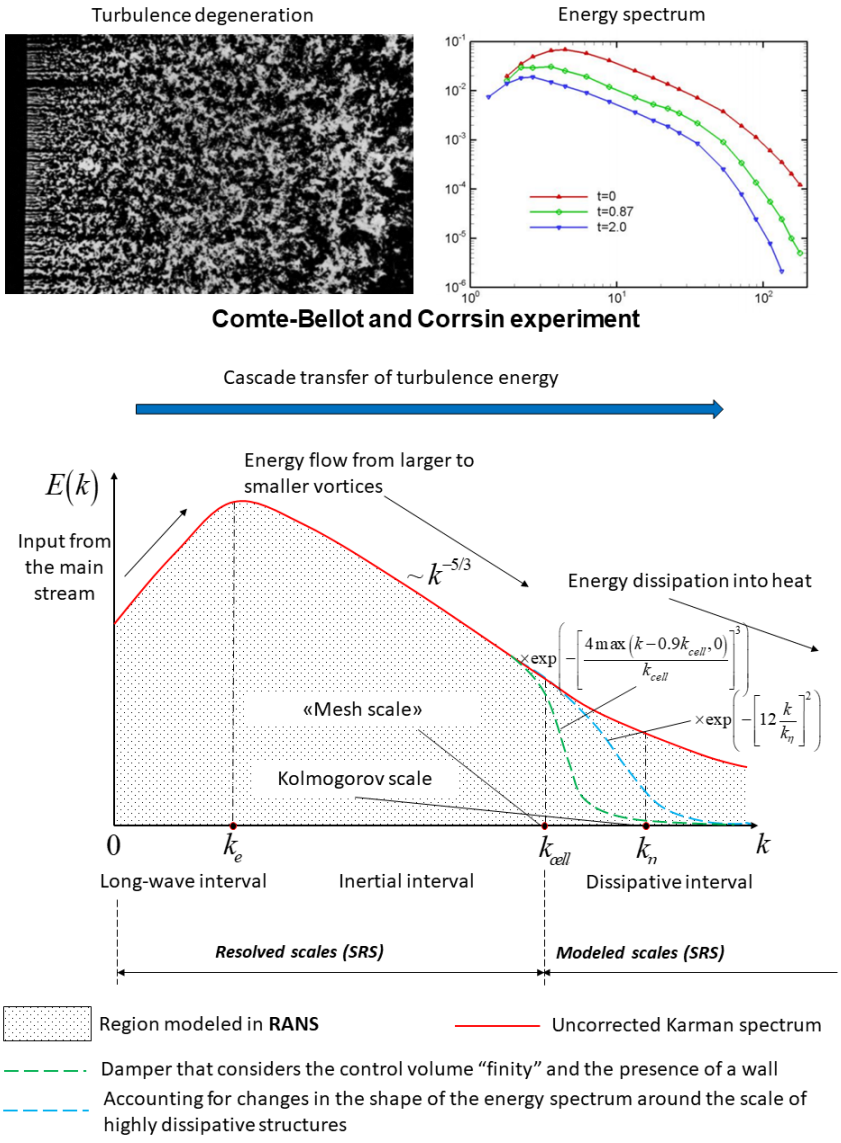

Figure 27: Spectral representation of pulsation energy during turbulence degeneracy [40]

The wave number corresponding to the Kolmagorov scale (the scale of structures dissipating into heat) of turbulence is determined according to the dependence:

$$k_\eta = \frac{2\pi}{\left(\nu^3/\varepsilon\right)^{0.25}} \tag{45}$$

Where, ν - kinematic viscosity, ε - rate of dissipation of turbulence kinetic energy into heat.

The value of the wave number, which corresponds to the size of the control volume, can be estimated according to the dependence:

$$\boldsymbol{k_{cell} = \frac{2\pi}{2min\left\{0.3\sqrt[3]{\frac{12V_{cell}}{\sqrt{2}}} + 0.1d_{wall}, \sqrt[3]{\frac{12V_{cell}}{\sqrt{2}}}\right\}}} \tag{46}$$

Where, V_{cell}- volume of adjacent control volume (assumed close to a regular tetrahedron), d_{wall}- nearest distance to a solid wall from the current node.

Normalized amplitudes $q_n(\vec{r})$ determined based on (43) and can be represented as a discrete set (47) of N values for each spatial point.

$$q_n(\vec{r}) = \frac{\int_{k_n}^{k_{n+1}} E(k)dk}{\int_0^\infty E(k)dk} \approx \frac{E(k_n)\Delta k_n}{\sum_{n=1}^{N} E(k_n)\Delta k_n} \tag{47}$$

To simulate the stochastic nature of turbulence, it is necessary to determine the corresponding unit vectors, which are random variables. Table 4 presents the basic conditions for determining the unit vectors of direction, unit vectors of wave number, phase and angular frequency.

Table 4: Determination of phase quantities and decomposition characteristics

Vector/scalar	Description
$\vec{\boldsymbol{d}}_{\boldsymbol{n}} = \{\boldsymbol{d_{nx}}; \boldsymbol{d_{ny}}; \boldsymbol{d_{nz}}\}$	A unit vector that defines the direction of the wave number, which is the radius vector of a point uniformly distributed over the surface of the unit sphere.
$\vec{\boldsymbol{\sigma}}_{\boldsymbol{n}} = \{\boldsymbol{\sigma_{nx}}; \boldsymbol{\sigma_{ny}}; \boldsymbol{\sigma_{nz}}\}$	A unit vector that determines the direction of the velocity mode at a specific spatial point. The direction is determined by a random, uniformly distributed number in the interval $[0; 2\pi)$ provided that $\vec{d}_n \cdot \vec{\sigma}_n = 0$ (Figure 28)
$\boldsymbol{\varphi_n}$	Phase of mode with number *n*, uniformly distributed in the interval $[0; 2\pi)$.
$\boldsymbol{s_n}$	Dimensionless circular frequency of mode with number *n*, which is a random variable with normal distribution $\mu = 2\pi; \sigma = 2\pi)$

The "synthetic turbulence" time scale τ, which is global for the entire calculation procedure, is defined as:

$$\tau = \frac{2}{U} max\left(\frac{k_e}{2\pi}\right) \quad (48)$$

where, U - determining flow velocity.

The set of wave numbers is preserved for the entire computational domain, and is specified according to a geometric progression (denominator - $q = 1.01 \div 1.05$), and the minimum wave number value corresponds to $\beta min[k_e(r)]$ [41]. The number of calculated modes is estimated based on the assumption that the maximum wave number is equal to $\frac{3}{2} max[k_{cell}(r)]$.

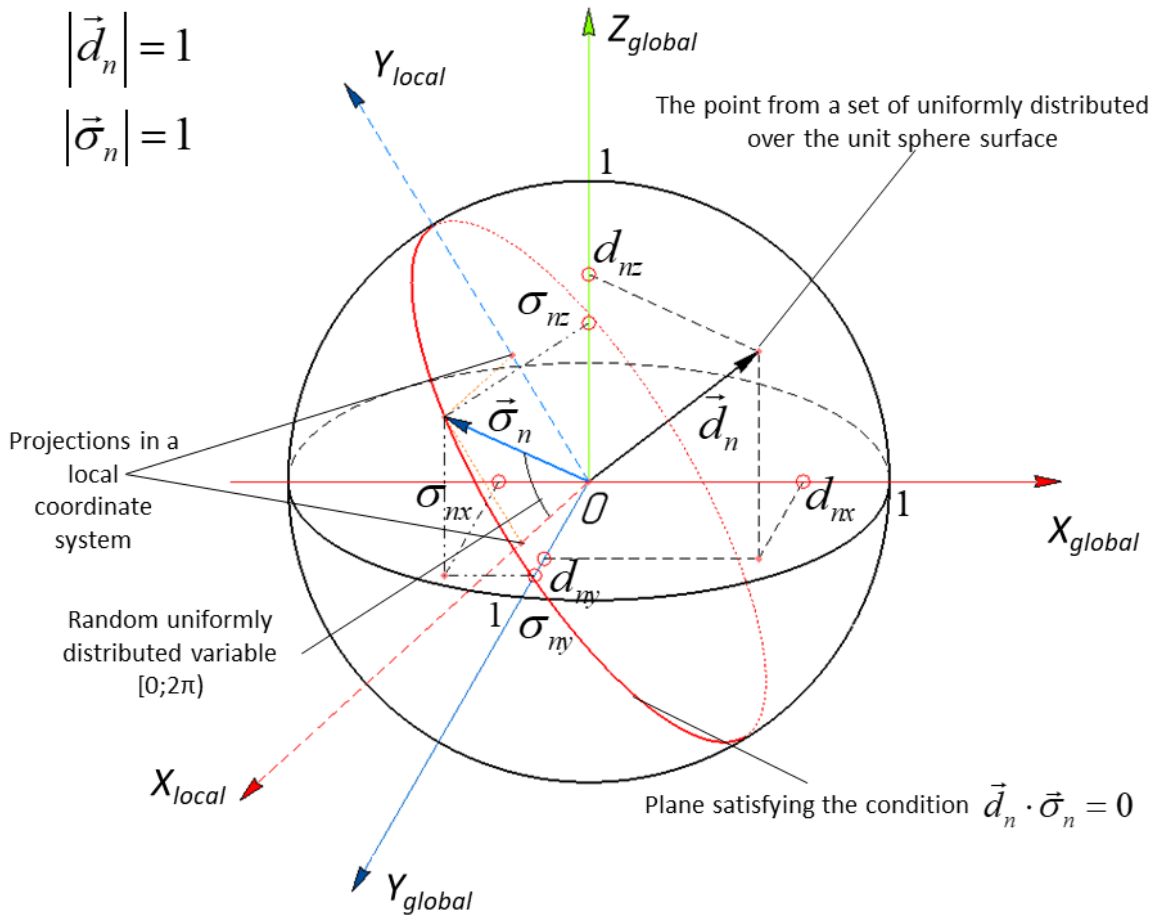

Figure 28: Towards the determination of the wave number unit vectors and projections of the pulsation velocity components

The restoration of the static pressure pulsation field p' can be carried out based on energy considerations. The total energy of turbulence consists of kinetic and potential energy of fluctuations. This conclusion on the basis of the generality of conservation laws for physical processes leads to the fact that $p'(r,t) \sim k_t = \frac{\rho \vec{U}^2(r,t)}{2}$ [42]. On the other hand, pressure pulsation has a nonlinear relationship between pulsations at geometrically close points. In fact, this means that the amplitude value is determined by the double correlations of the pulsations at the corresponding points (by and large, including the velocity). As a result of

research, as well as theoretical generalizations obtained for correlations of velocity and pressure, the field of pressure pulsations can be represented through the field of pulsations of the velocity modulus as [39]:

$$p'(r,t) \sim k_t = C \cdot \rho([u']^2 + [v']^2 + [w']^2) \quad (49)$$

Yuber's experiments [39], indicate that the coefficient C at high Reynolds numbers (developed turbulence in the main flow) tends to $C \approx 0.7 \div 0.8$. The developed procedure assumes that the pressure pulsation corresponds to twice the kinetic energy of turbulence ($C = 1$).

The calculation procedure consists of two stages. At the first stage, the defining parameters in the expansion (42) are calculated and the temporary functions of the velocity projection are formed.

The main difficulty lies in determining the unit vectors $\vec{d}_n$ and $\vec{\sigma}_n$, namely obtaining a uniform distribution over the sphere surface with subsequent orthogonalization of a randomly directed vector $\vec{\sigma}_n$ relative to $\vec{d}_n$. As part of the synthetic turbulence generation procedure, a generator of a random uniformly distributed value was developed based on the Delaunay triangulation algorithm. A virtual triangular mesh consisting of regular triangles of equal area was superimposed on the surface of the sphere, which in fact (within the error of the method) makes it possible to obtain a linear indexed array of *N* evenly distributed points. In this case, the task of obtaining the unit vector actually comes down to playing the number from 1 to *N* (depending on the surface discretization) with a pseudo random number generator. For convenience, when finding the coordinates of the unit vector $\vec{\sigma}_n$ a local coordinate system (LCS) of the plane perpendicular to $\vec{d}_n$ is introduced. The local coordinate system is obtained by rotating the global coordinate system (GCS) around the Oz axis so as to exclude any one projection onto the axis perpendicular to Oz. Then the intermediate coordinate system is rotated around the axis of the intermediate coordinate system with zero projection $\vec{d}_n$ so that $\vec{d}_n$ is actually projected at the starting point of the LCS (Figure 28). Next, an angle is generated in the LCS in the form of a randomly distributed value within $[0; 2\pi]$ and projections of the unit radius vector are found. After this, by matrix rotations of the LCS in the reverse order described above, projections $\vec{\sigma}_n$ in the GCS are restored.

To avoid numerical problems in damping functions $exp\left(-\left[12\frac{k}{k_\eta}\right]^2\right)$ and $exp\left(-\left[\frac{4\max(k-0.9k_{cell},0)}{k_{cell}}\right]^3\right)$ a degree control is introduced, which limits the calculation of the function and replaces it with a number close to 0.0.

At the second stage, a smoothing interpolation function is constructed on a discrete set of input data coordinates, which is subsequently used only for visualization.

The following quantities are used as a set of input data: coordinates of the angles near surfaces or volume, density, dynamic viscosity μ, eddy viscosity μ_t, dissipation rate of kinetic energy of turbulence ε, specific dissipation rate of kinetic energy of turbulence ω, kinetic energy of turbulence k_t, volume of the adjacent control volume V_{cell}, distance to

the nearest wall d_{wall}. The results of comparative analysis with calculations obtained in [26, 41] are showed in Figure 29 - Figure 30.

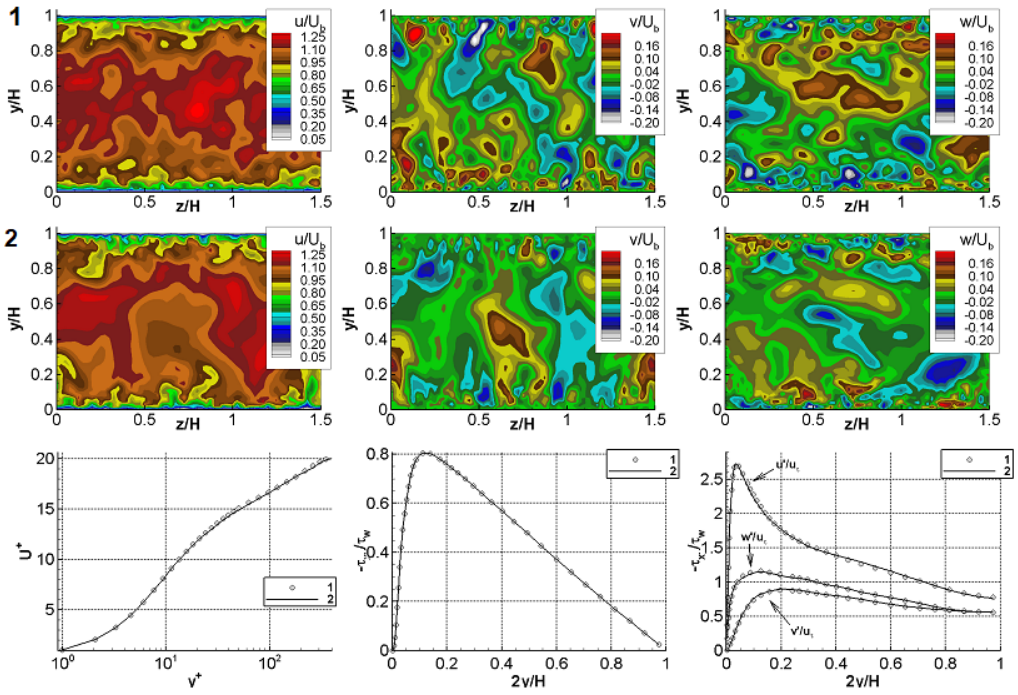

Figure 29: Comparison of the velocity pulsation field generated using the synthetic turbulence method (1) with that calculated using the SRS method (2) [41]

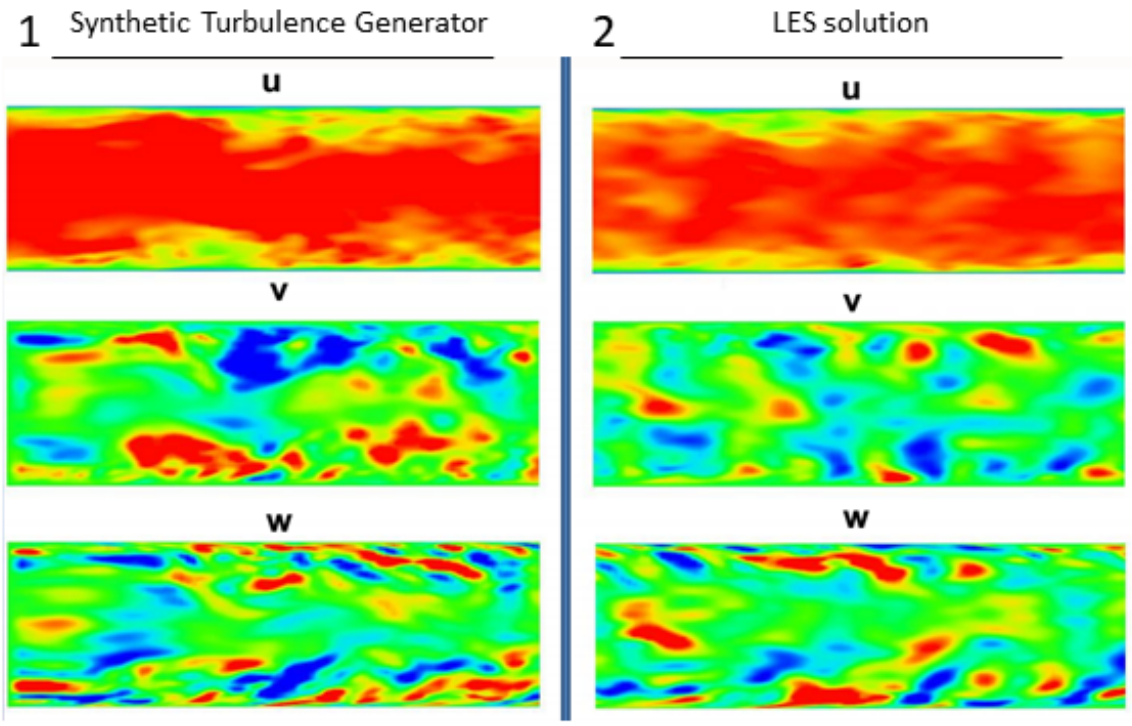

Figure 30: Velocity pulsation field in a flat channel obtained using the synthetic turbulence method (1) and using LES (2) [26]

Also, as an example of the synthetic turbulence procedure application, an analysis of the results obtained for the VVER-1000 reactor downcomer could be presented. The time step for the formation of a discrete output data set of the pressure pulsation field was taken equal to 0.25 from the minimum cyclic frequency in the velocity field expansion. The generated volume of pulsation field data corresponds to 1 m/s. The determining velocity U included in (48) is defined as the average mass value in the cold leg of the main circulation circuit (MCC), and is taken equal to 9.8 m/s. Coefficient β, which determines the minimum wave number, is taken equal to 0.5, and the denominator of the geometric progression is equal to 1.025.

The procedure for reconstructing the pressure pulsation field based on synthetic turbulence was used for the external/internal cylindrical surfaces of the core barrel and the reactor pressure vessel.

The time dependence of the normalized maximum pressure pulsations is shown in Figure 31.

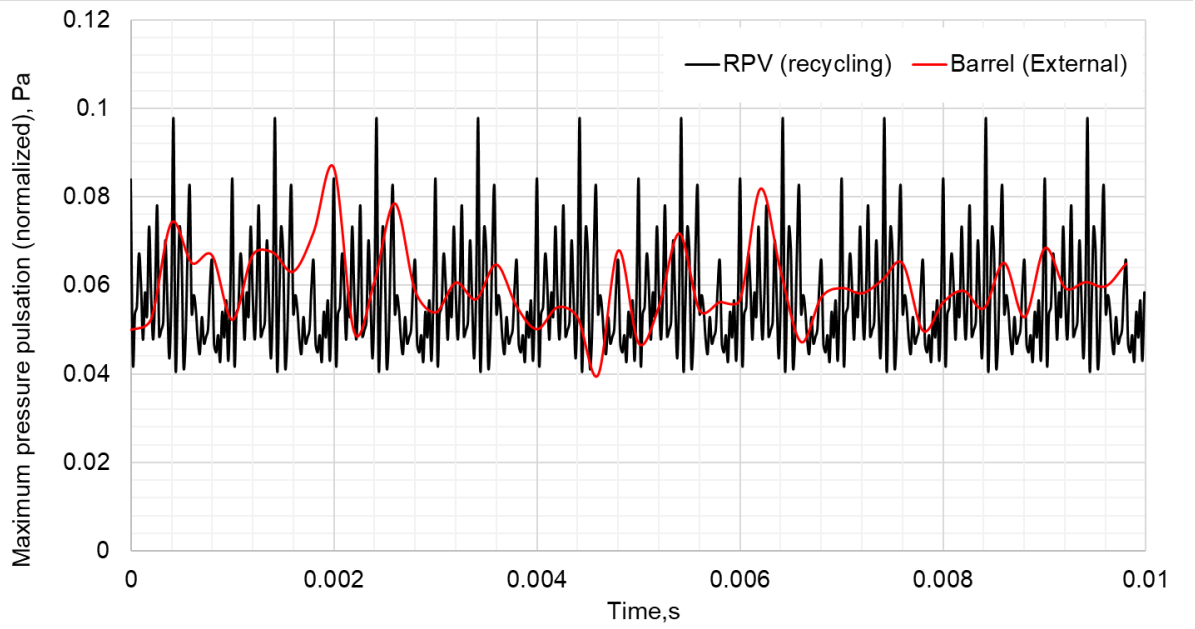

Figure 31: Change in the maximum value of pressure pulsation normalized to the dynamic pressure at the reactor inlet (cold leg of the MCC) over time

The root mean square value of the generated maximum pressure pulsations (normalized) in the downcomer corresponds to ~0.015, while according to experimental data [44] taking into account the equality of the inlet velocity to ~10 m/s it corresponds to a value of ~0.011. According to the amplitude values, considering that, approaching the wall, the speed decreases, experiments on a cylindrical surface [42] give a pulsation value from 0 to 2-4 kPa with an undisturbed flow. Using the synthetic turbulence procedure, values in the downcomer region are predicted to be ~3.4 kPa. Even such a non-rigorous comparison of the results indicates a high degree of physicality of the results obtained.

3.4 Definition of oscillators and forces calculation method

To estimate both vertical and transverse displacements, two methods of specifying oscillators are considered. Two-dimensional approximation is considered by default. In the first case, this is a concentrated mass on an ideal spring suspension, which in general can consist of n ideal springs with different stiffnesses. The second type of primitive oscillators are the so-called angular oscillators (Figure 32). Note that each of these simple oscillator types are available in commercial CFD packages that support the **Rigid Body** approximation.

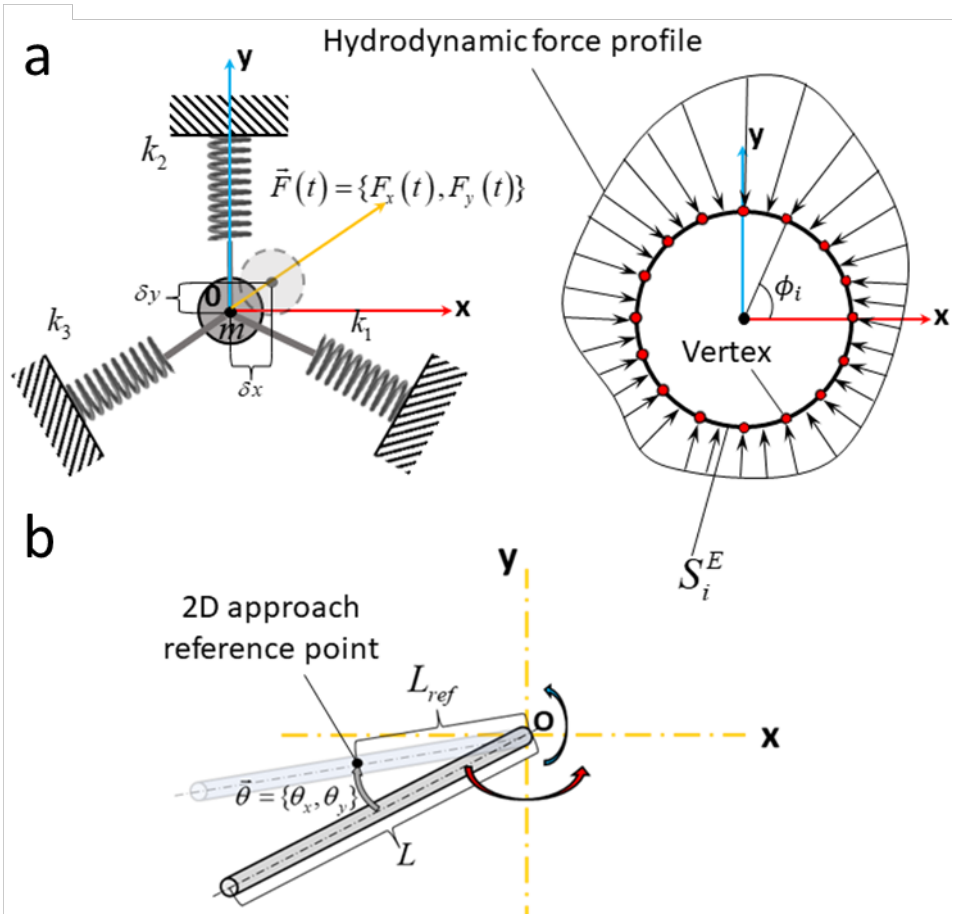

Figure 32: Method for determining oscillators (a – spring oscillator, b – angular oscillator)

To determine the displacements using the example of a three-spring oscillator with damping, a system of equations is used:

$$\begin{cases} m\dfrac{d^2(\delta x)}{dt^2}+\sum_{i=1}^{n}\left[\left(k_i\delta x+\beta\dfrac{d(\delta x)}{dt}\right)cos^2(a_i)+\left(k_i\delta y+\beta\dfrac{d(\delta y)}{dt}\right)sin(a_i)cos(a_i)\right]=F_x(t) \\ m\dfrac{d^2(\delta y)}{dt^2}+\sum_{i=1}^{n}\left[\left(k_i\delta x+\beta\dfrac{d(\delta x)}{dt}\right)cos(a_i)sin(a_i)+\left(k_i\delta y+\beta\dfrac{d(\delta y)}{dt}\right)sin^2(a_i)\right]=F_y(t) \end{cases} \quad (50)$$

where m – concentrated mass, kg; k – spring stiffness, N/m; β – equivalent damping factor, N·s/m; F_x and F_y – resultant hydrodynamic (disturbing) forces.

To determine displacements using a simple angular oscillator model (Figure 32 b) equation (51) with a single resultant force is applied. Where, the displacement in chosen direction is defined as (52).

$$J\frac{d^2\theta}{dt^2} + J\left(\frac{d\theta}{dt}\right)^2 + (2\pi f_0)^2 J\theta = F * L_{ref} \tag{51}$$

$$\delta = \theta * L_{ref} \tag{52}$$

In each case, force effects are calculated in two ways. In the first case, the concept of braking speed in the form of dynamic pressure is used. There, forces are determined using the equation:

$$F(t) = \begin{Bmatrix} F_x(t) \\ F_y(t) \end{Bmatrix} = \sum_{i=1}^{m} (p + 0.5\rho[u^2 + v^2]) S_i^E \begin{bmatrix} \cos(\phi_i) \\ \sin(\phi_i) \end{bmatrix} \tag{53}$$

Where, m – the number of calculated points along the selected perimeter, S_i^E – an elementary area.

$$F(t) = \begin{cases} F_x = \sum_{i=1}^{m} \left(-p \cdot \cos(\phi_i) + \mu \left[2\frac{\partial u}{\partial x}\cos(\phi_i) + \left(\frac{\partial u}{\partial y} + \frac{\partial v}{\partial x}\right)\sin(\phi_i) \right] \right) S_i^E \\ F_y = \sum_{i=1}^{m} \left(-p \cdot \sin(\phi_i) + \mu \left[\left(\frac{\partial u}{\partial y} + \frac{\partial v}{\partial x}\right)\cos(\phi_i) + 2\frac{\partial v}{\partial y}\sin(\phi_i) \right] \right) S_i^E \end{cases} \tag{54}$$

To consider synthetic turbulence fields in the force factors, a pulsating pressure component is added for equations (53) and (54). It is assumed that the velocity fluctuations are damped in the boundary layer. If there is fastening in one of the cross-section directions, the corresponding force is assumed to be zero

3.5 Various methods of implementing calculations

IPP considers several options for using the described approaches, which can be adapted depending on the specifics of the problem being solved. The simplest method is based on the use of a commercial CFD package (ANSYS CFX, Fluent) with the concept of **Rigid Body.** This approach is preferred unless there are special flow or solid body conditions. Also, results using a commercial package can be used for cross-validation/verification of own procedures. The second option is the coupled use of external procedures for generating synthetic turbulence and an oscillator with a CFD code (ANSYS CFX). This method makes it possible to take into account the presence of turbulent pulsations in force factors. The schematic diagram for calculating one iteration at a global time step Δt is shown in Figure 33. It should be noted that in this method of implementing coupling, the concept of three time steps is introduced. The first of them is the global time step of iterations, the second

is the local step of solving equation (50) or (51), which is taken to be several times (approximately 10 times) smaller than the global one. In this case, the solution of (50) or (51) is sought implicitly in the interval from Δt_{i-1} to Δt_i under initial conditions in the form of displacements and their velocities. The third time step concerns the update of the turbulent pulsation field, which can be controlled independently of the two previous types. The calculation of forces in this case is carried out using the relations (53). Despite the fairly simple implementation, flexibility of settings, as well as the ability to implement special models and non-local relationships, the proposed method has a drawback associated with the non-optimal distribution of computing resources. The most time-consuming is updating synthetic turbulence fields (their calculation and reinitialization), which in some cases can take 30÷50% of the total calculation time per global time step.

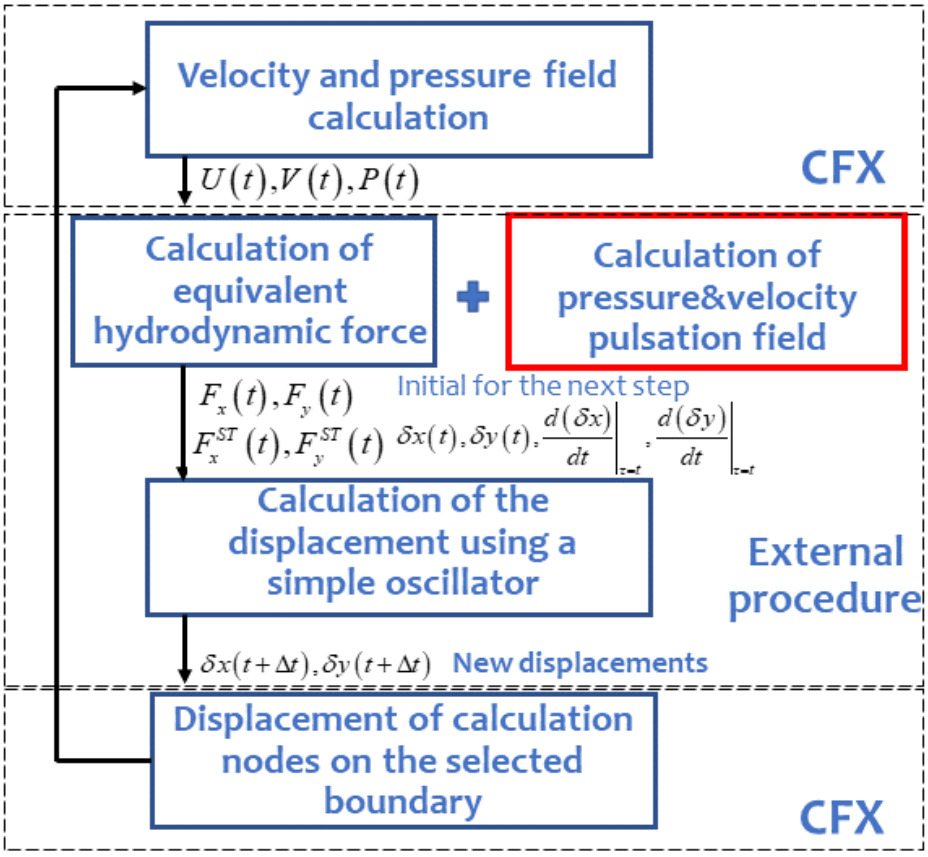

Figure 33: Scheme of organizing one computational cycle for a global time step

The third option for organizing calculations considers our own procedure, which solves the isothermal system (55) in a two-dimensional incompressible approximation.

$$\begin{cases} \dfrac{\partial U}{\partial x} + \dfrac{\partial V}{\partial y} = 0 \\ \dfrac{\partial U}{\partial t} = \alpha U + \beta U_0 + \gamma U_{00} + U\dfrac{\partial U}{\partial x} + V\dfrac{\partial U}{\partial y} = -\dfrac{1}{\rho}\dfrac{\partial p}{\partial y} + \mu_{eff}\left(\dfrac{\partial U^2}{\partial x^2} + \dfrac{\partial U^2}{\partial y^2}\right) - gn_x \\ \dfrac{\partial V}{\partial t} = \alpha V + \beta V_0 + \gamma V_{00} + U\dfrac{\partial U}{\partial x} + V\dfrac{\partial U}{\partial y} = -\dfrac{1}{\rho}\dfrac{\partial p}{\partial y} + \mu_{eff}\left(\dfrac{\partial V^2}{\partial x^2} + \dfrac{\partial V^2}{\partial y^2}\right) - gn_y \end{cases} \quad (55)$$

Where α, β, γ – time derivative discretization coefficients (implicit, second order), which are determined by (56) for the adaptive time step, n_x and n_y – projection of gravity onto the coordinate axes.

$$\alpha = \frac{2\Delta t + \Delta t_0}{\Delta t(\Delta t + \Delta t_0)}; \beta = \frac{\Delta t + \Delta t_0}{\Delta t \Delta t_0}; \gamma = \frac{\Delta t}{\Delta t(\Delta t + \Delta t_0)} \quad (56)$$

Where Δt – current time step, Δt_0- previous time step.

The effective viscosity is calculated using the one-parameter RNG turbulence model, in which, for simplicity, the turbulent Prandtl number Pr_t is taken as a constant value equal to 1.0.

The solution (55) is based on the Finite-Element Method (FEM). In this case, velocities are described by the second order and pressure by the first/second order. The shape function is chosen in the form of a geometric polynomial. A nonlinear solution is constructed in the form of "lagging" coefficients with preservation of gradient values. The iterative procedure tracks the convergence of the fields by calculating the average and maximum deviations. Velocity and pressure fields are solved without segregation, which for a two-dimensional case is a fairly reliable method when using FEM.

The computational mesh is structured anisotropic with the presence of moving areas and an algorithm for dynamic blocks re-meshing (Figure 34). When the geometry changes (the movement of the nodes of which, according to the procedure settings, is estimated at the end of the iterative cycle in space or at the end of the time step), the data is strictly associated to the node indices. Consequently, the structure of the matrix remains similar, and updating is only necessary for the values of the corresponding cells, which helps speed up calculations. The calculation procedure provides for the possibility of thickening the computational mesh near solid walls.

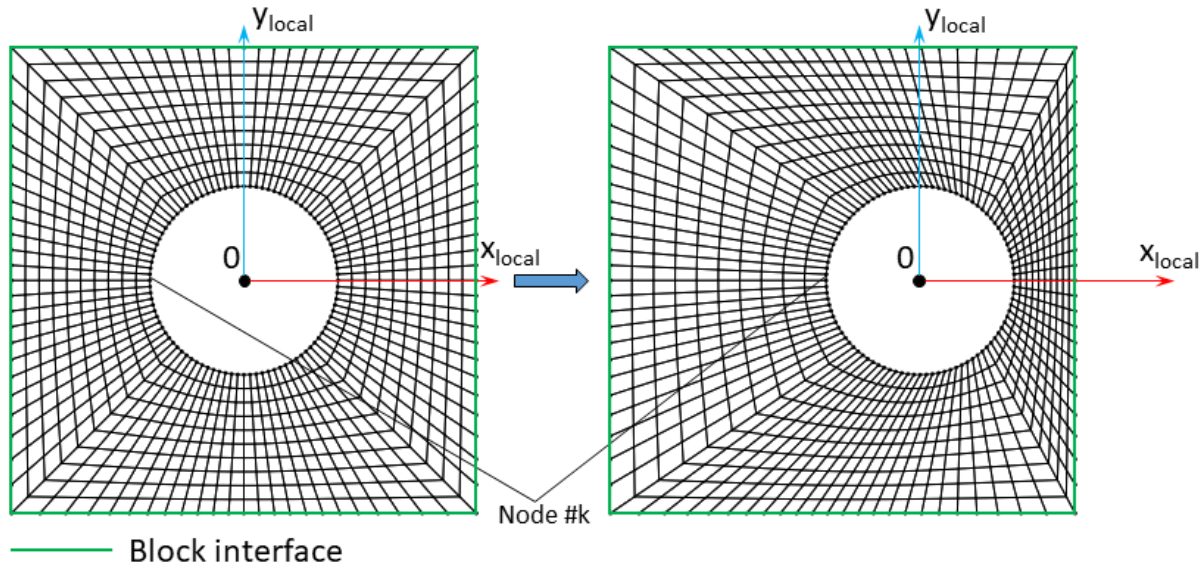

Figure 34: Dynamic mesh block

At each node, the pulsating components of the velocity and pressure fields can be calculated. To do this, it is necessary to determine the matrix coefficients (41). Since the RNG 1-eq. model operates with effective viscosity, the calculation of matrix coefficients (kinetic energy of turbulence) can be carried out in two ways. In the first case, it is considered that turbulence is in equilibrium, which allows us to assume that the specific kinetic energy is equal to its dissipation. Otherwise, if we assume that dissipation is not equalized with generation, then it is necessary to use an additional parameter (scale of turbulence). Thus, the coefficients of matrix (41) are calculated using (57).

$$\sqrt{R_{11}} = \sqrt{R_{22} - A_{21}^2} = \sqrt{R_{33} - A_{31}^2 - A_{32}^2} = \begin{cases} I: \sqrt{\dfrac{2\nu_t}{3C_D}};\ \varepsilon = \dfrac{\nu_t}{C_D} \\ II: \sqrt{\dfrac{2}{3}\dfrac{\nu_t}{l}};\ \varepsilon = \dfrac{1}{l} C_d^{-0.5} \nu_t^{1.5} \end{cases} \tag{57}$$

Where $C_D = 0.08$, l – turbulence scale.

To calculate the distance to the wall, the Poisson equations with zero Dirichlet conditions are solved. The field that characterizes the distance to the wall is calculated using the dependence (58).

$$\begin{gathered} \nabla^2 \varphi = -1 \\ d_{wall} = |\nabla\varphi| + \sqrt{|\nabla\varphi|^2 + 2\varphi} \end{gathered} \tag{58}$$

3.6 Conclusions and further work

This section provides a brief description of the approaches used by IPP to calculate coupled vibrations in a simplified formulation. To generate turbulent pulsations, which can be taken into account when determining the resultant force, the synthetic turbulence procedure is used. The proposed procedure is simplified, since it is based on local parameters that take into account only the averaged flow history. In this case, the turbulent characteristics (correlations of velocity pulsations) are considered as isotropic. Despite significant simplifications compared to procedures that consider the transfer of pulsation characteristics, preliminary tests showed a good degree of agreement between the qualitative picture of the synthetic turbulence generator and the application of the SRS method, which is satisfactory for engineering practice. The pulsation component of pressure is calculated based on a simple algebraic relationship, where it is assumed that pressure pulsation is a dynamic consequence of velocity pulsation. The main approaches for organizing the calculation procedure, as well as the method for calculating the resultant force, are briefly outlined. In order to organize more efficient calculations, a one-parameter turbulence model of effective kinematic viscosity transfer was proposed, which is obtained by combining two k-ε RNG equations. To achieve this, it became necessary to express the kinetic energy of turbulence and its dissipation through eddy viscosity.

Different variants of developed methods implementation are described, which are promising fast methods for coupled FSI analysis. Subsequent work will be aimed at applying and testing the developed and proposed approaches on test cases.

4. Projection based fluid model for fast running FSI

This chapter presents the fast-running fluid-structure interaction (FSI) model development by TU Delft on construction of a reduced order fluid model using the projection of the fluid response onto the structural modes. The chapter describes the theory of the projection based reduced order model (ROM) as well as some alternatives for reducing the computational effort of FSI simulations required to build the ROM model.

4.1 Introduction

For the development of a fast-running FSI model, the problem of vibration of rod (bundles) in axial flow is taken as focus point. This type of problem is characterized by small vibration amplitudes compared to the length of the rod, a steady mean flow condition (i.e. there is no large scale vortex shedding as in cases with rods in cross flow) and Turbulence Induced Vibration (TIV) that contributes significantly to the vibration amplitude of the rod.

To predict the amplitude of the rod vibration, it is essential to accurately capture all physical mechanisms that feed or dissipate energy into the structural system. The structure itself can dissipate energy through material damping, for linear structure properties proportional to the vibration velocity. Energy can be transferred from the fluid to the structure as well, due to wall shear and pressure loads on the structure. The energy transfer can be both positive, i.e. leading to an increase in the structure's vibration energy (increase of vibration amplitude) or negative (leading to a damping of the structural vibration).

When the fluid is modelled through direct numerical simulation (DNS) or large eddy simulation (LES), the effect of the fluid when flowing around a deformable object is captured, including the resolved (large) turbulence fluctuations. Since even LES is a computationally demanding simulation technique, in particular when also including the coupling to a structure, often the dynamics of the fluid are resolved in an ensemble-averaged manner, unsteady Reynolds-Averaged Navier-Stokes (URANS), where the unsteady effect on the mean flow is resolved, but only turbulence statistics are resolved using a turbulence model.

A direct FSI simulation of a URANS model coupled to a structure model tends to underpredict the vibration amplitude of the rod, due to the lack of the turbulence forcing that is averaged out in the URANS approach. Methods like the ones described in Chapter 1 and Chapter 3 of this report, aim to re-introduce the turbulence fluctuations which causes energy being transferred from the turbulence fluctuations into the vibration. This turbulence forcing can also be obtained from surface pressure fluctuations sampled through e.g. an a-priori LES simulation around a static rod, or from experimental data. However, a significant amount of computational effort is required for an FSI simulation of a URANS and a structural model.

Since the structure can be efficiently represented by a reduced set of vibration modes, while still capturing the most important modes for predicting the vibration amplitude, here we will create a ROM for the (mean) fluid response to those vibration modes. This would allow the URANS fluid model to be replaced by the developed ROM and should include the fluid dynamic effects in terms of added mass, damping and stiffness effects. Building the

ROM requires sampled responses of the fluid model to a pre-determined interface perturbation. Alternative methods to improve the computational speed further are also investigated.

In section 4.2 the components of an FSI system are introduced. Section 4.3 then describes the methodology of sampling and projecting the fluid response onto structural modes including alternatives for building the ROM basis. Section 4.4 focuses on the specific implementation into Ansys/CFX. Results on a single rod configuration are presented in Section 4.5 and Section 4.6 closes the chapter with conclusions and an outlook for future work.

4.2 FSI system

The case under consideration is the flow induced vibration of long, slender (fuel) rods in axial flow conditions. For these type of rods the diameter *d* is much smaller than the rod length *L* and the amplitude of the vibrations is much smaller than the diameter *d*. With these properties, the structure dynamics are considered linear for the small displacements from its undeformed state. For axial flow conditions, the flow is considered steady (apart from turbulence fluctuations) for the undeformed state and responding linearly to the structure dynamics.

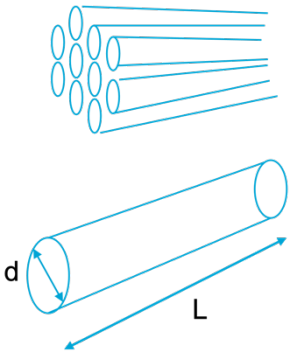

To simulate such a system a FSI approach is required. The main components of a fluid-structure interaction model are:

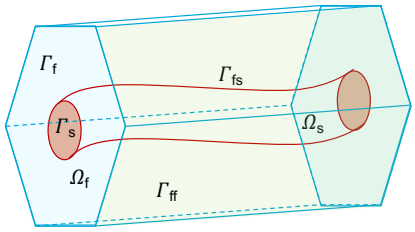

1. Structure domain Ω_s: governing equations for the structure dynamics, with boundary conditions on Γ_s
2. Fluid domain Ω_f: governing equations for the fluid dynamics, with boundary conditions on Γ_f and (periodic) conditions on Γ_{ff} when bundles are considered
3. Fluid-structure interface Γ_{fs}: kinematic and dynamic conditions to satisfy to have continuity of motion and equality of stresses on the interface

Solving both fluid and structure dynamics, together with satisfying the boundary and interface conditions, is often referred to as a monolithic approach. However, here preference is given to a partitioned approach, where different solvers are used to discretize and solve the governing equations of the fluid domain and structure domain. The challenge for partitioned solvers is satisfying the kinematic and dynamic interface conditions.

To represent the FSI system in a discretized form, we use a finite element model (FEM) to represent the structure dynamics

$$M\ddot{\boldsymbol{x}} + D\dot{\boldsymbol{x}} + K\boldsymbol{x} = \boldsymbol{F}$$

where *M*, *C*, *K* are the mass, damping and stiffness matrices, ***x*** is the state vector of the structure including all its degrees-of-freedom, and ***F*** is the discretized load on the structure (e.g. the action of the fluid onto the structure). For the computational fluid dynamics (CFD) model, a finite volume URANS model in an arbitrary Langrangian-Eulerian (ALE) formulation is used

$$\frac{d}{dt}\iiint_{V(t)} \boldsymbol{W} dV + \oiint_{S(t)} \left(\boldsymbol{E} - \boldsymbol{W}\frac{d\vec{x}}{dt}\right)\vec{n}dS = \iiint_{V(t)} \boldsymbol{J} dV$$

where ***W*** is the fluid state vector of conserved quantities within the volume *V* which contains e.g. the mass, momentum, turbulence model parameters, ***E*** contains the fluid dynamics define the change in e.g. momentum due to the action of convection through the boundary *S* or the action of pressure and shear stresses on the boundary S, $\frac{d\vec{x}}{dt}$ is the velocity of the boundary *S* and represents the effect of the motion/deformation of the control volume *V* in time and ***J*** contains any volume source terms. When the fluid model does not resolve but models turbulence, the fluid state contains ensemble-averaged quantities e.g. velocity $\bar{u}$ and pressure $\bar{p}$ and a statistical representation of the turbulence, e.g. turbulence kinetic energy k, whereas a single realization would contain fluctuations due to turbulence u', p'. The ensemble averaged and fluctuation of a quantity φ are defined as

$$\bar{\varphi}(x,t) = \lim_{N\to\infty} \frac{1}{N}\sum_{i=1}^{N} \varphi_i(x,t)$$

$$\varphi_i'(x,t) = \bar{\varphi}(x,t) - \varphi_i(x,t)$$

For a proper prediction of TIV, these fluctuations p' are essential. Obtaining these by simulating a single realization with e.g. DNS or LES is computationally expensive, and since we focus here on fast running methods, we assume that a turbulence pressure fluctuation realization can be reconstructed from the mean flow (e.g. using the PFM model from Chapter 1).

Within the computational framework, there is one additional step that can be seen as a third domain or field that needs to be solved for: the deformation of the fluid mesh. Within the ALE framework the fluid domain is not stationary, and a method is required to deform the interior part of the fluid mesh based on the deformation of its boundary: for FSI simulations this is typically the deformation of the fluid-structure interface for which the structure model provides the magnitude of the deformation.

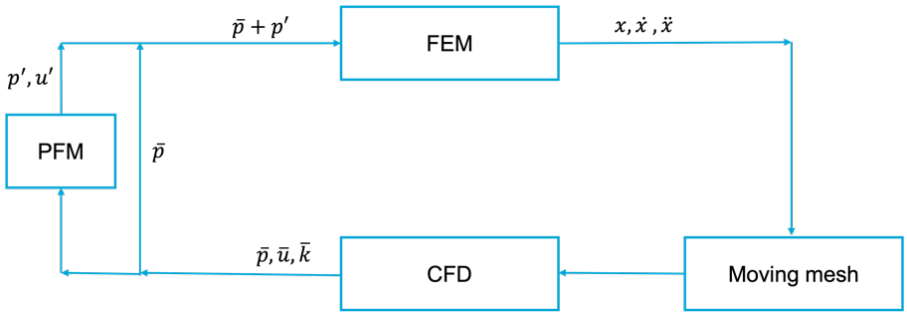

Figure 35: Full model FSI framework

Within the flow diagram, we can identify the structural domain, indicated by FEM, that solves for the structure dynamics (of the fluid-structure interface) in terms of displacement, velocity and acceleration. To satisfy the kinematic condition on the fluid-structure interface, the fluid mesh is moved accordingly and the (URANS) fluid dynamics are solved in the CFD block. This provides the ensemble averaged flow quantities: part of this provides a load on the fluid-structure interface which can be seen as the "deterministic" load $\bar{p}$ (for brevity only pressure is indicated, but wall shear stresses can be treated in the same way), and the "stochastic" load p', which can be obtained from the mean flow quantities and turbulent statistics through a PFM model.

Within this model, each block FEM, Moving mesh, CFD and PFM can still take substantial computational time. To reduce computational costs, we focus in particular on reducing the computational effort of the Moving mesh and CFD by replacing that by a ROM that predicts the (deterministic) dynamic fluid response to a given kinematic state of the fluid-structure interface.

4.3 Methodology

To build the fluid ROM, we start by decomposing the structure dynamics into decoupled modal vibrations. This gives a motivation to build a fluid response model to a reduced set of interface modes. Next the fluid response model is discussed: which interface kinematics to sample and how it can be seen as a pseudo-structural response model. Finally some alternatives for building the response model are discussed that can reduce computational efforts even further.

4.3.1 Structural vibration modes

Starting with the general dynamics for the structure

$$M\ddot{\boldsymbol{x}} + D\dot{\boldsymbol{x}} + K\boldsymbol{x} = \boldsymbol{F}$$

and the assumption that Rayleigh damping is applied (D is a linear combination of M and K), the system with N degrees of freedom, can be written as a system of N decoupled harmonic oscillator equations by projecting it onto the structural eigenmodes $\boldsymbol{\phi}_i$. The structure state is therefore defined by a constant mode shape $\boldsymbol{\phi}_i$ and a modal amplitude $a_i(t)$:

$$\boldsymbol{x}(t) = \sum_{i=1}^{N} \boldsymbol{\phi}_i a_i(t)$$

and its time derivates simply follow from the time derivatives of $a_i(t)$:

$\dot{\boldsymbol{x}}_i(t) = \sum_{i=1}^{N} \boldsymbol{\phi}_i \dot{a}_i(t)$ and $\ddot{\boldsymbol{x}}(t) = \sum_{i=1}^{N} \boldsymbol{\phi}_i \ddot{a}_i(t)$

The property of the mode shapes $\boldsymbol{\phi}_i$ is that they are orthogonal, that they diagonalize *M* and *K* (and hence also *D* since it is assumed a linear combination of *M* and *K*), and with the appropriate scaling, satisfy $\boldsymbol{\phi}_i^T M \boldsymbol{\phi}_i = 1$, and $\boldsymbol{\phi}_i^T K \boldsymbol{\phi}_i = \omega_i^2$, and therefore the structure dynamics can be seen as *N* decoupled scalar equations:

$$\ddot{a}_i + d_i \dot{a}_i + \omega_i^2 a_i = \boldsymbol{\phi}_i \boldsymbol{F}(t) = f_i(t)$$

which represent the dynamics *a(t)* of a specific mode given a (external) modal forcing $f_i(t)$. This shows that the dynamics of each structural mode, can be regarded as the response of a (damped) harmonic oscillator with a certain damping d_i and natural radial frequency ω_i to an external forcing $f_i(t)$. Note that the modes can be ordered in increasing frequency. Since for harmonic motions, for a given force magnitude, the amplitude, velocity and acceleration scale with $1/\omega_i^2$, $1/\omega_i$ and 1 respectively: the low frequency modes tend to have larger amplitudes and the higher frequency modes a larger damping. Therefore, although including all *N* modes allows the perfect representation of the original problem, very often only the first *M* modes are taken into account, as they would represent the most significant contributions to the resulting vibration amplitude.

The modal forcing $f_i(t)$ is obtained from spatially filtering the external forcing **F**(t). From a continuous perspective, this could be seen as computing the inner product between the continuous mode shape and a continuous forcing. Suppose we take the rod as example, the external force from the fluid onto the rod's surface (Γ_{fs}) is the surface integral of the distributed fluid loads (pressure and wall shear stress), multiplied by the mode shape, i.e.

$$f_i(t) = \oiint_{\Gamma_{fs}} \phi(x)(-p + \bar{\bar{\tau}})\vec{n} dS$$

The properties of a harmonic oscillator under external harmonic forcing are well known: the amplitude of the resulting vibration motion when $F(t) = \sin \omega t$ depends on the frequency ratio ω/ω_i: when the ratio is close to 1, resonance occurs and the resulting amplitude gets very large, depending on the structural damping that is present.

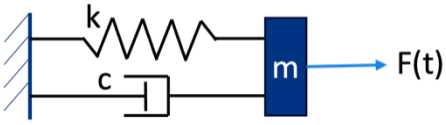

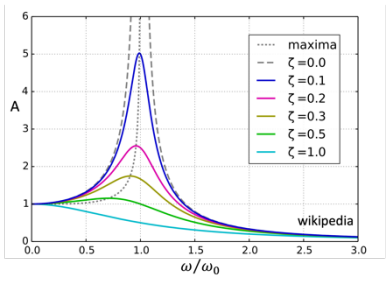

This is in particular important for the forcing due to pressure fluctuations from turbulence, as turbulence scales operate over a broad spectrum and can therefore contain a forcing close to the natural frequency for which the energy transfer from flow to structure is very effective.

Although the turbulence pressure fluctuations *p'* may be treated as a constant external forcing to the structure, the interaction between the mean (deterministic) flow and the vibration of the structure mode is more direct and will be discussed in the next section.

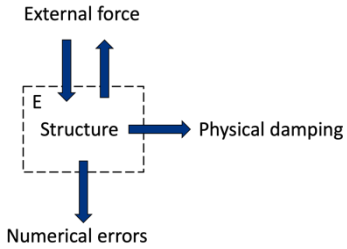

As a result, if the amplitude of the structural motion is sought, we need to accurately determine the mechanisms that feed or dissipate energy from (each of) the structural modes. When the structure includes physical damping, this provides a means of dissipating energy. Solving the structure numerically can introduce numerical dissipation (for now this will be ignored and assumed to be much smaller than the physical damping). Lastly, energy can be added or removed through the external forcing, which in this case comes from the pressure and wall shear stress that the fluid exerts onto the structure. This fluid dynamic load has two contributions: the one from the mean/deterministic loads (resolved by URANS) and the one from the turbulence pressure fluctuation model. The latter one could be analyzed by spatially filtering the fluctuations for each structural mode and temporally filtering the modal forcing to the content close to resonance as it is this energy content that will feed effectively into the vibration mode.

4.3.2 Fluid response model

In the previous section it was discussed that in order to get a good prediction of the vibration amplitude, it would be sufficient to include a subset of the first *M* vibration modes. Secondly, the response of the mean fluid on those vibration modes needs to be determined as well. Within the FSI framework this means that we can represent the coupling diagram as below.

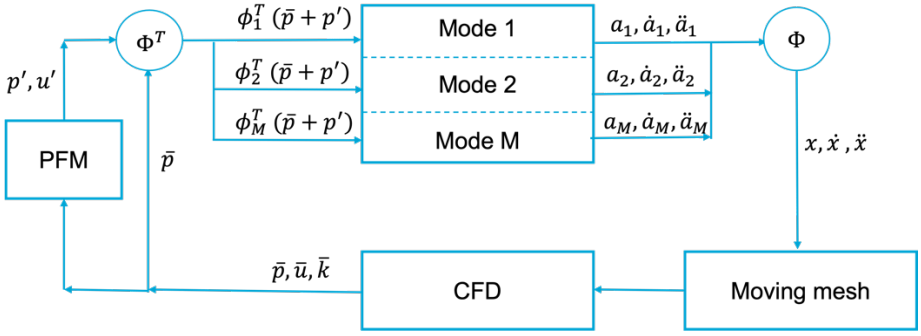

Figure 36: Reduced model FSI framework

The diagram shows that the output of the CFD is projected onto each mode $\boldsymbol{\phi}_i$ that is included and which will cause the each mode to obtain a state $a_i, \dot{a}_i, \ddot{a}_i$. Multiplying the modal states by their mode shape $\boldsymbol{\phi}_i$ results again in the dynamics of the fluid-structure interface $x_i, \dot{x}_i, \ddot{x}_i$. When using a regular approach, the Moving mesh can be applied to deform the fluid domain and the CFD block can be used to solve for the new fluid state. Although the structure part has been simplified, the computational intensive parts of moving the mesh and solving the URANS equations is still present. Also, the FSI coupling may require multiple sub-iterations if the coupling between flow and structure is strong,

adding to the computational work. We intend to replace the large amount of work of solving flow on a deforming domain, by a simplified response model.

To build the response model, we take the approach sketched in the diagram below.

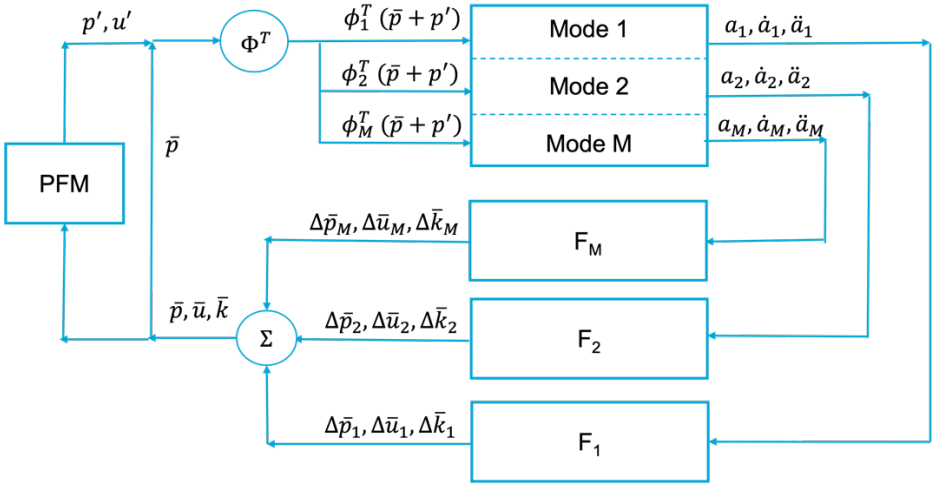

Figure 37: Reduced order fluid response model FSI framework

We intend to find response functions to a modal excitation of the fluid-structure interface and have the response depend on the modal amplitude, velocity and acceleration. An interpretation of these dependencies is that the response to a modal amplitude is how the fluid responds when it experiences a change in the interface shape/location: this is analogous to the reaction of a spring in a harmonic oscillator. The response of the fluid to a modal velocity is analogous to the reaction of a damper in a harmonic oscillator and the response of the fluid to a modal acceleration represents the added mass effect that the fluid has. The responses to the modes can then be summed up to get a prediction of the change of the mean flow properties due to the interaction with the structure. In this diagram we still consider the pressure fluctuations to come from e.g. a PFM model, which could take into account the changed mean flow conditions and turbulence statistics, but it may not be required if the changes in these quantities are small enough such that the main characteristics of the turbulence do not change.

To illustrate the collection of information for the response model, we consider the rod to be oriented along the *x*-axis and that the mode shape only has displacement in *y*-direction. The mode shape will therefore be just a scalar function in *x*. To build the information required for the response model, we impose the kinematics of the interface according to

$$\delta y_i(x,t) = A_y \phi_i(x) g_\tau(t/\tau)$$

where δy is the imposed interface displacement in *y* and g_τ is some function in time and A_y is a scaling of the amplitude of the imposed displacement. Note that the modal amplitude, velocity and acceleration are related to g_τ in this way:

$$a(t) = A_y g_\tau\left(\frac{t}{\tau}\right), \qquad \dot{a}(t) = \frac{A_y}{\tau}\dot{g}_\tau\left(\frac{t}{\tau}\right), \qquad \ddot{a}(t) = \frac{A_y}{\tau^2}\ddot{g}_\tau\left(\frac{t}{\tau}\right)$$

which shows that ratios between amplitude, velocity and acceleration are determined by the time scale τ, and the maximum amplitude by A_y. A large time scale presents a more pseudo-steady motion, where the amplitude is more dominant than velocity or acceleration, and a small time scale represent a very dynamic motion, where the acceleration is more dominant. Then, a simulation is run, starting from the reference steady state with the URANS ALE solver (CFD with Moving mesh) using this imposed motion. This will provide the full fluid response $\Delta\bar{p}_i(\vec{x},t)$, $\Delta\bar{\vec{u}}_i(\vec{x},t)$, … etc. to a perturbation in the kinematics of mode *i*, e.g.

$$\Delta\bar{p}_i(\vec{x},t) = \bar{p}_i(\vec{x},t) - \bar{p}(\vec{x},0)$$

where $\bar{p}(\vec{x},0)$ is the reference (steady state) solution at t = 0, and $\bar{p}_i(\vec{x},t)$ the sampled pressure for a perturbation in mode *i*. The response of the fluid is "full" in the sense that its response, when projected onto a mode shape *j*, can result in a forcing of that mode. Therefore, even though the structure dynamics result in a decoupled system, a coupling between modes is reintroduced through the action of the fluid.

Next, we want to approximate the observed responses with a simplified model based on the modal amplitude, velocity and acceleration, i.e. correlate the response to g_τ, $\dot{g}_\tau$ and $\ddot{g}_\tau$. The prototype model is

$$\Delta\bar{p}_i(\vec{x},t) \approx \Delta\bar{p}_{M,i}(\vec{x})\ddot{a}_i(t) + \Delta\bar{p}_{D,i}(\vec{x})\dot{a}_i(t) + \Delta\bar{p}_{K,i}(\vec{x})a_i(t)$$

where the subscripts *M*, *D* and *K* refer to pseudo mass, damping and stiffness effects. Since the solution fields are sampled using $N_{\Delta t}$ time steps, the coefficients $\Delta\bar{p}_{M,i}$, $\Delta\bar{p}_{D,i}$ and $\Delta\bar{p}_{K,i}$ can be obtained from the overdetermined system:

$$\begin{bmatrix} \ddot{a}(t_1) & \dot{a}(t_1) & a(t_1) \\ \ddot{a}(t_2) & \dot{a}(t_2) & a(t_2) \\ \vdots & \vdots & \vdots \\ \ddot{a}(t_{N_{\Delta\tau}}) & \dot{a}(t_{N_{\Delta\tau}}) & a(t_{N_{\Delta\tau}}) \end{bmatrix} \begin{bmatrix} \Delta\bar{p}_{M,i}(\vec{x}) \\ \Delta\bar{p}_{D,i}(\vec{x}) \\ \Delta\bar{p}_{K,i}(\vec{x}) \end{bmatrix} = \begin{bmatrix} \Delta\bar{p}_i(\vec{x},t_1) \\ \Delta\bar{p}_i(\vec{x},t_2) \\ \vdots \\ \Delta\bar{p}_i(\vec{x},t_{N_{\Delta\tau}}) \end{bmatrix}$$

Note that for each location $\vec{x}$ (or each cell of the mesh), a least-squares system can be defined to determine the local $\Delta\bar{p}_{M,i}(\vec{x})$, $\Delta\bar{p}_{D,i}(\vec{x})$ and $\Delta\bar{p}_{K,i}(\vec{x})$

$$\begin{bmatrix} \langle\ddot{a},\ddot{a}\rangle & \langle\ddot{a},\dot{a}\rangle & \langle\ddot{a},a\rangle \\ \langle\dot{a},\ddot{a}\rangle & \langle\dot{a},\dot{a}\rangle & \langle\dot{a},a\rangle \\ \langle a,\ddot{a}\rangle & \langle a,\dot{a}\rangle & \langle a,a\rangle \end{bmatrix} \begin{bmatrix} \Delta\bar{p}_{M,i}(\vec{x}) \\ \Delta\bar{p}_{D,i}(\vec{x}) \\ \Delta\bar{p}_{K,i}(\vec{x}) \end{bmatrix} = \begin{bmatrix} \langle\ddot{a},\Delta\bar{p}_i(x)\rangle \\ \langle\dot{a},\Delta\bar{p}_i(x)\rangle \\ \langle a,\Delta\bar{p}_i(x)\rangle \end{bmatrix}$$

were the notation <a,b> is used to denote the inner-product of two vectors. Within the forced response simulation, this inner product can also be seen as a representation of the integral over the time interval of two functions, i.e. $\langle a,b\rangle \approx \frac{N_{\Delta t}}{\tau}\int_0^\tau a(t)b(t)dt$. Now, with specific choices for $g_\tau(t/\tau)$, some simplifications can be made:

1. Desire $\int_0^\tau g_\tau(t/\tau)dt = 0$: this makes the inner product of any constant with g_τ to be equal to zero $\langle g_\tau, c\rangle = 0$ for any constant *c*. Consequently, the contribution of the constant solution $\bar{p}(\vec{x},0)$ is zero and hence $\langle a,\Delta\bar{p}_i(x)\rangle = \langle a,\bar{p}_i(x)\rangle$.

2. For a similar reason, require $\int_0^\tau \dot{g}_\tau(t/\tau)dt = 0$, and $\int_0^\tau \ddot{g}_\tau(t/\tau)dt = 0$.
3. Have $g_\tau(0) = g_\tau(1) = \dot{g}_\tau(0) = \dot{g}_\tau(1) = 0$: this ensures that $\langle a, \dot{a}\rangle = \langle \dot{a}, \ddot{a}\rangle = 0$.
4. For scaling purposes, we want the maximum $|g_\tau|$=1.
5. For smooth perturbations from the steady state, we require also $\ddot{g}_\tau(0) = \ddot{g}_\tau(1) = \dddot{g}_\tau(0) = \dddot{g}_\tau(1) = 0$

Without going into much detail, we can obtain such a function as a 9th order polynomial:

$$g(\xi) = \sum_{i=4}^{9} c_i \xi^i$$

with $c_4 = 1230.1875, c_5 = 7381.125, c_6 = 17222.625, c_7 = 19683, c_8 = 11071.6875$ and $c_9 = 2460.375$. Below the resulting $g(\xi), \dot{g}(\xi)$ and $\ddot{g}(\xi)$ are shown:

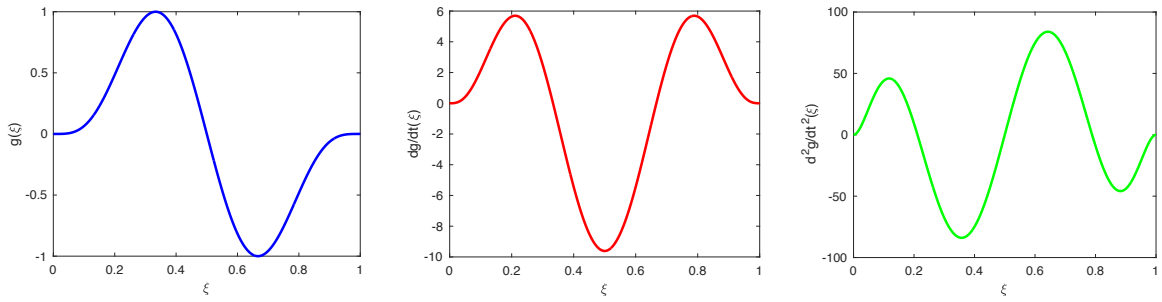

Figure 38: Temporal forcing function g(ξ), ġ(ξ) and g̈(ξ)

Using the properties of the forcing function, the least squares system that needs to be solved for is simplified to:

$$\begin{bmatrix} \Delta\bar{p}_{M,i}(\vec{x}) \\ \Delta\bar{p}_{D,i}(\vec{x}) \\ \Delta\bar{p}_{K,i}(\vec{x}) \end{bmatrix} = \begin{bmatrix} \langle\ddot{a},\ddot{a}\rangle & 0 & \langle\ddot{a},a\rangle \\ 0 & \langle\dot{a},\dot{a}\rangle & 0 \\ \langle a,\ddot{a}\rangle & 0 & \langle a,a\rangle \end{bmatrix}^{-1} \begin{bmatrix} \langle\ddot{a},\bar{p}_i(x)\rangle \\ \langle\dot{a},\bar{p}_i(x)\rangle \\ \langle a,\bar{p}_i(x)\rangle \end{bmatrix}$$

which has the advantage that the inverse can be expressed as

$$\begin{bmatrix} \langle\ddot{a},\ddot{a}\rangle & 0 & \langle\ddot{a},a\rangle \\ 0 & \langle\dot{a},\dot{a}\rangle & 0 \\ \langle a,\ddot{a}\rangle & 0 & \langle a,a\rangle \end{bmatrix}^{-1} = \frac{1}{A_y^2 N_{\Delta t}} \begin{bmatrix} a\tau^4 & 0 & b\tau^2 \\ 0 & c\tau^2 & 0 \\ b\tau^2 & 0 & d \end{bmatrix}$$

with *a*, *b*, *c* and *d* constant values:

$$\begin{aligned} a &= 1.144063107029098 \cdot 10^{-3} \\ b &= 7.452753954361003 \cdot 10^{-2} \\ c &= 4.216689737335880 \cdot 10^{-2} \\ d &= 7.601809033448315 \cdot 10^{0} \end{aligned}$$

Therefore, the fluid response coefficients $\Delta\bar{p}_{M,i}(\vec{x})$, $\Delta\bar{p}_{D,i}(\vec{x})$ and $\Delta\bar{p}_{K,i}(\vec{x})$ can be obtained by computing three averaged solution fields during the transient simulation, weighted with a, $\dot{a}$ and $\ddot{a}$, and multiplying by the inverse least-squares matrix. It is shown here for the pressure field, but all other fluid state variables can be processed in a similar way as well. For each (structural) mode that we want to include the response to, an additional simulation needs to be run with a forced excitation of that mode and constructing the fluid response by determining the averaged solutions when weighted with a, $\dot{a}$ and $\ddot{a}$.

A schematic representation of the resulting reduced order response model of the fluid is given below:

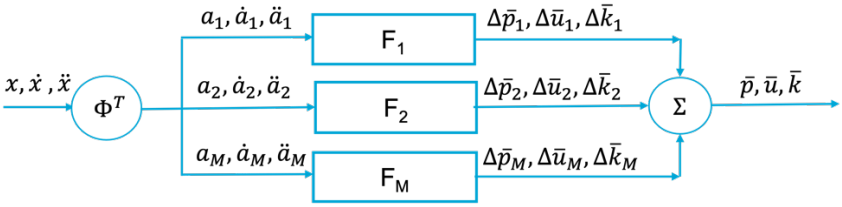

Figure 39: Reduced order fluid response model

For any given fluid-structure interface state $(x, \dot{x}, \ddot{x})$, this is projected onto the basis that was chosen to construct the response model, which gives the modal states $(a_i, \dot{a}_i, \ddot{a}_i)$, for which the response in the fluid field was obtained from the forced excitation test. The contribution of all modal responses is summed up to obtain a resulting fluid state. In principle, this model would be usable to replace the moving mesh and CFD part in a coupled simulation. Even if the structure properties would change, the fluid model should give a proper response, as long as the mode shapes for which the response model was built are a good enough basis to represent the modes of the new structure.

An additional step is to construct the information of the coupled system: a structure system represented by *M* modes, and a fluid response system obtained for those *M* modes: in that situation, the output of the fluid response model is projected again on the structure modes to obtain the modal forcing from the fluid to the structure. In this way the coupled problem can be written as a new structure model which has the effect of the fluid incorporated into added mass, damping and stiffness.

A direct way to obtain this information is to project the mean fluid response on the fluid-structure interface (i.e. the tractions acting on the interface from the pressure and wall shear stress), immediately onto the structural modes, i.e. when the interface is forced in mode *i*, the modal forcing in mode *j* is

$$\bar{f}_{j,i}(t) = \oiint_{\Gamma_{fs}} \phi_j(x)(-\bar{p}_i + \bar{\bar{\tau}}_i)\vec{n}dS$$

Here, $\bar{f}$ denotes the modal forcing from the mean (URANS) flow, to make it distinct from the modal forcing contribution that comes from e.g. the turbulent pressure fluctuations and that is denoted by f'. Using the same approach as when constructing the full fluid response model, the response $\bar{f}_{j,i}(t)$ is going to be represented by terms related to the displacement, velocity and acceleration of the forced excitation:

$$\bar{f}_{j,i}(t) \approx \hat{m}_{j,i}\ddot{a}_i + \hat{d}_{j,i}\dot{a}_i + \hat{k}_{j,i}a_i$$

for which the coefficients $\hat{m}_{j,i}$, $\hat{d}_{j,i}$ and $\hat{k}_{j,i}$ can be obtained from a least-squares fit of the data and represent added mass, damping and stiffness. Note that these can have coupling from one mode to the other and effectively result in matrices $\widehat{M}, \widehat{D}$ and $\widehat{K}$, which can be combined with the decoupled structure dynamics equations

$$\ddot{a}_j + d_j\dot{a}_j + \omega_j^2 a_j = \sum_{i=1}^{M} \bar{f}_{j,i} + f_j'$$

Or, when writing this in a matrix form

$$\begin{bmatrix} 1 & & \\ & \ddots & \\ & & 1 \end{bmatrix}\ddot{\boldsymbol{a}} + \begin{bmatrix} d_1 & & \\ & \ddots & \\ & & d_M \end{bmatrix}\dot{\boldsymbol{a}} + \begin{bmatrix} \omega_1^2 & & \\ & \ddots & \\ & & \omega_M^2 \end{bmatrix}\boldsymbol{a} = \widehat{M}\ddot{\boldsymbol{a}} + \widehat{D}\dot{\boldsymbol{a}} + \widehat{K}\boldsymbol{a} + \boldsymbol{f}'$$

which gives the vibration dynamics of a rod with the effect of the mean fluid response included. The response of this system to a turbulent pressure fluctuation field *p'* can be analyzed through

$$\left(\begin{bmatrix} 1 & & \\ & \ddots & \\ & & 1 \end{bmatrix} - \widehat{M}\right)\ddot{\boldsymbol{a}} + \left(\begin{bmatrix} d_1 & & \\ & \ddots & \\ & & d_M \end{bmatrix} - \widehat{D}\right)\dot{\boldsymbol{a}} + \left(\begin{bmatrix} \omega_1^2 & & \\ & \ddots & \\ & & \omega_M^2 \end{bmatrix} - \widehat{K}\right)\boldsymbol{a} = \boldsymbol{f}'$$

Note that when the turbulence statistics are considered independent of the mean flow variation, and e.g. a PFM model is used to construct different realizations for the turbulence fluctuations, this turbulence forcing can be regarded as an external forcing for which the dynamic response of the coupled fluid-structure interaction system can be obtained by solving a reduced order system of size *M*x*M* (with *M* the number of modes for which the fluid response model was built)

4.3.3 Fluid response model alternatives

In this section, two alternatives for constructing the fluid response model are presented. One of the assumptions made for allowing simplification is that the vibration amplitudes are very small compared to the diameter and length of the rod. Therefore, it is assumed that the geometric changes of the surface of the rod when vibrating (i.e. the changes in the wall normal) can be modeled by a "transpiration flux", which forces the flow to follow the same curvature as when the mesh would be deformed. This effectively eliminates the use of a moving mesh, reducing the computational cost. The other method relies on the assumption that the interaction between the flow and the structure is mainly through pressure, and that wall shear has a negligible effect. The motivation for that assumption is that the wall shear stress is acting in the axial direction mostly and that in this direction the displacement of the vibration of the rod is virtually zero (and therefore the work done by friction forces is virtually zero). Pressure, on the other hand is, is mostly acting perpendicular to the rod's axis, and therefore acting in the direction of the largest displacements (so the work done by pressure is large). To obtain an accurate variation in

the pressure, it can be sufficient to use an inviscid model (and/or use slip-wall boundary conditions).

Transpiration flux

The schematic representation how the transpiration flux replaces the mesh deformation is shown below:

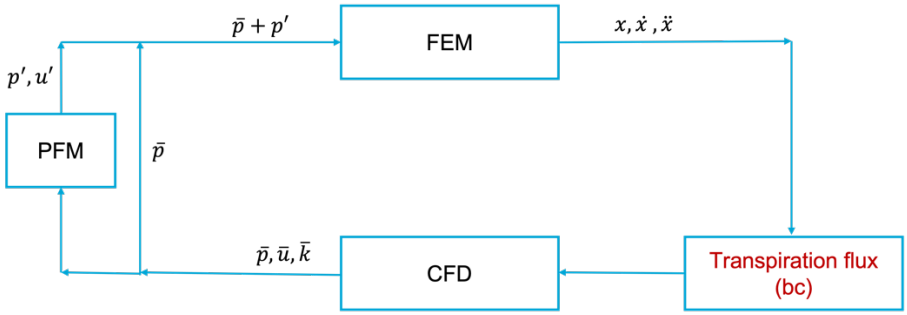

Figure 40: Replacing mesh motion by transpiration flux in the FSI framework

The transpiration flux is incorporated as a wall boundary velocity that adds/removes mass through the boundary. The magnitude of the transpiration flux is obtained by assuming that the curvature of the streamline when it follows the shape of the deformed structure, can be obtained by imposing that the flow direction U_y/U_x should be equal to the direction of the deformed wall, i.e. $\partial\delta_y/\partial x$.

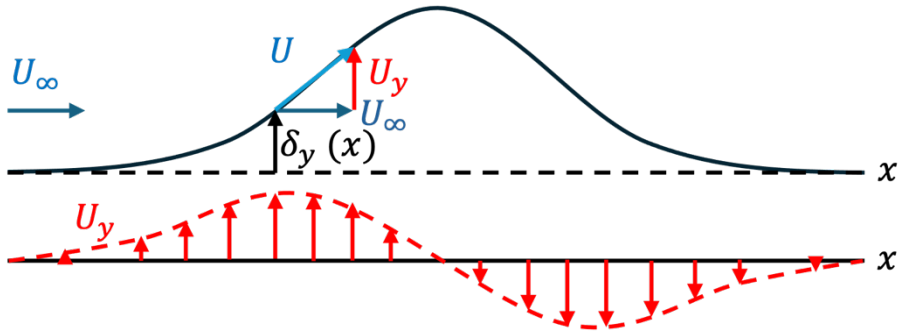

Figure 41: Definition of the transpiration flux velocity U_y

To obtain the transpiration flux velocity U_y, it is assumed that the horizontal velocity component $U_x \approx U_\infty$, so that

$$U_y(x) = U_\infty \frac{\partial \delta_y}{\partial x}$$

Inviscid modeling using a Vortex Particle/Panel Method

Instead of using the transpiration boundary condition within the (URANS) CFD simulation, the fluid model could also be modelled by a potential flow model using e.g. a vortex particle/panel method (VPM). This may also give a good prediction of the change in pressure on the surface for a deforming structure and can replace the forced modal excitation sampling using the URANS solver as explained in the previous section. The flow

diagram for the sampling/construction of the fluid response model using a VPM method is shown below.

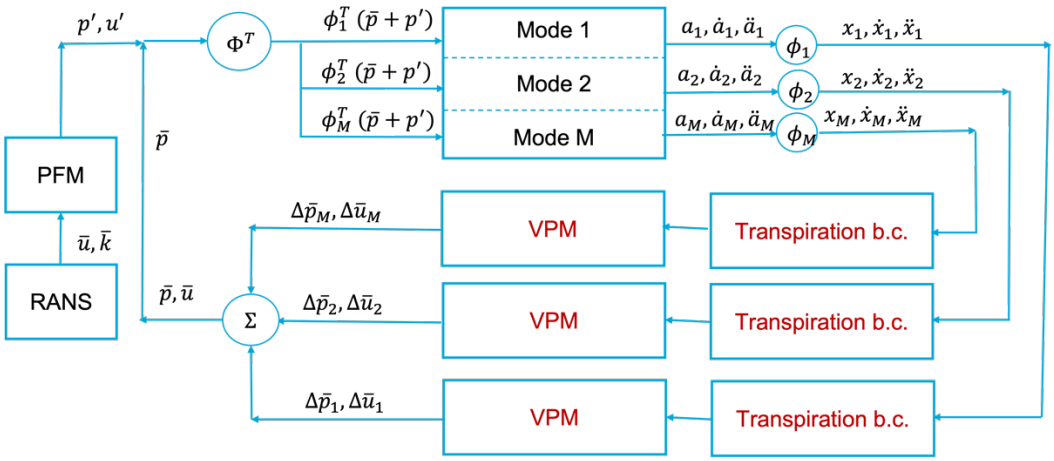

Figure 42: Using transpiration flux and VPM to construct fluid response model

Note, that the VPM model is capable of predicting the response in pressure and velocity, but it does not provide any information about the turbulence/viscous effects. However, the turbulence fluctuations can still be predicted from e.g. a pressure fluctuation model applied to the RANS solution for the static rods.

4.4 Implementation into ANSYS CFX

This section describes the practical implementation of obtaining the flow response to a modal excitation.

The first thing that is required is a chosen basis of modes for which the flow response is going to be sampled. This could be obtained from an eigenmode analysis from a structure solver, or in principle any other orthogonal basis. However, a basis that is close to the first eigenmodes of the structure that is going to be coupled to the flow response model is desirable, as these modes are expected to contribute the most to the amplitude of the vibration. In the results obtained in this report, the modes are obtained from a Matlab script that approximates

$$m\ddot{y} + k\frac{\partial^4 y}{\partial x^4} = 0$$

with clamped conditions at *x*=0 and x=1: $y(0) = 0, y'(0) = 0, y(1) = 0, y'(1) = 0$ using a finite difference approach to obtain

$$M\ddot{\boldsymbol{y}} + K\boldsymbol{y} = \boldsymbol{0}$$

Then, the eigenmodes of the system are found and ordered from smallest eigenvalue to largest. The first four eigenvalues that are used to test the methodology are shown in the figure below.

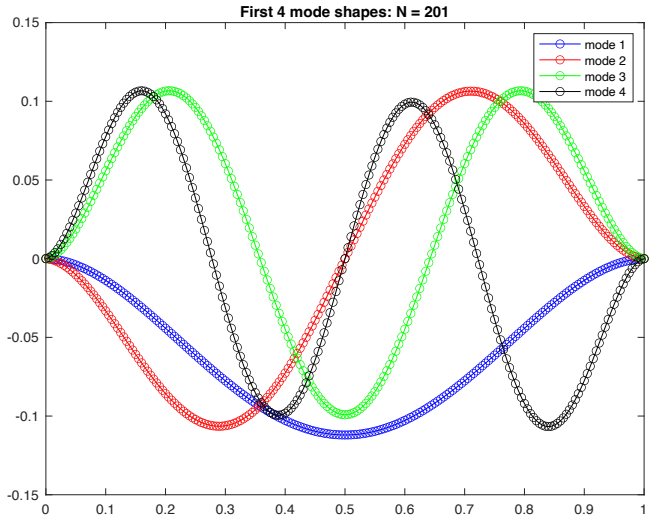

Figure 43: First four mode shapes

These mode shapes are then added to CFX as a tabulated interpolation User Function. This provides a continuous representation of the modes $\phi_i(x)$. Also, the amplitude forcing function $g_\tau(t/\tau)$ is added as an expression, as well as its derivatives $\dot{g}_\tau(t/\tau)$ and $\ddot{g}_\tau(t/\tau)$

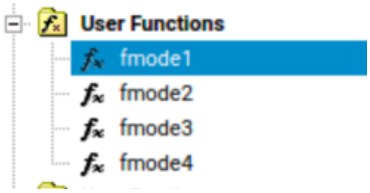

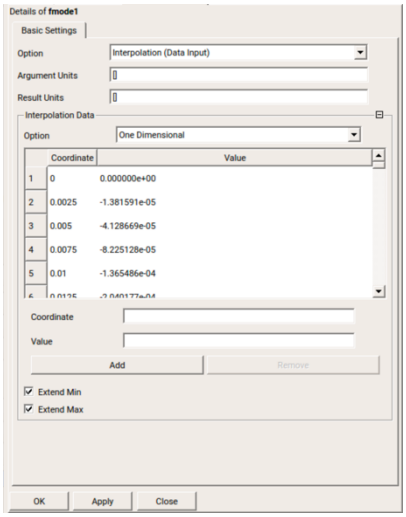

To obtain the fluid response field, "Additional Variables" and expressions are defined for each flow variable for which we want to obtain a Δ-response. As example the expressions and additional variables used for computing the $\Delta\bar{p}_{M,i}(\vec{x})$ field are given (i.e. the response of the mean pressure due to the acceleration in mode *i*). The additional variable "Fmode{j}" represent the modal force response $\bar{f}_{j,i}(t)$, the variables {P|U}field{M|D|K} represent the inner-product between the modal acceleration (M), velocity (D) and displacement (K) and the pressure (P) or velocity (U) field. For "PfieldM", the dimension is therefore [Pa m s^-2] and is defined as "Pressure*fd2Adt2*Ay/Tsim^2" (i.e. $\bar{p}_i(x)\ddot{g}A_y/\tau^2$). While running the simulation for the imposed motion, the mean of "PfieldM" is computed. This will then represent $\langle\ddot{a}, \bar{p}_i(x)\rangle = \langle\ddot{a}, \Delta\bar{p}_i(x)\rangle$ (for the specific construction of $g_\tau(t/\tau)$ and when averaged over the whole time interval $t = [0, \tau]$). The last step is defining the additional variables "d{u|p}{M|D|K}" which represent the fluid

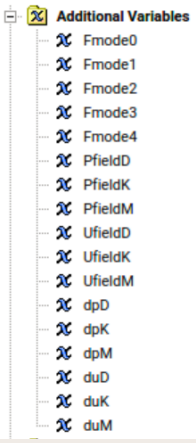

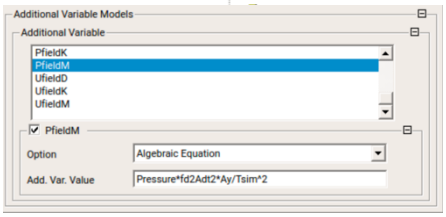

modal response in the velocity (u) or pressure (p) field for a excitation in the modal acceleration (M), velocity (D) or displacement (K). For "dpM", i.e. representing $\Delta\bar{p}_{M,i}(\vec{x})$, the dimension is [Pa m^-1 s^2], and it is defined by the expression "dpMexpr", which uses the averaged flow field information and the (precomputed) inverse components of the correlation matrix.

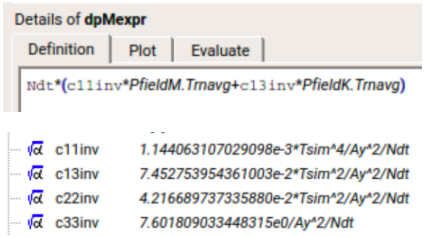

The simulation that is run is defined by these parameters: the *M* modes that are included, the mode that is excited *i*, the amplitude of the excitation A_y, the simulation time τ and the number of time steps $N_{\Delta t}$. For each simulation, we obtain the modal response loads on all modes *j*, i.e. $\bar{f}_{j,i}(t)$, and the Δ-responses for all selected variables.

4.5 Results of building fluid ROM

4.5.1 Fluid response model alternatives

First the alternatives for obtaining forced response results are investigated for both the transpiration flux option and the use of a VPM approach. The rod is deformed in some predefined shape (here: $\delta y_i(x,t) = A_y\frac{1}{2}(1-\cos 2i\pi\, x)\sin\omega_y t$). For the results shown in this section *i* = 2.

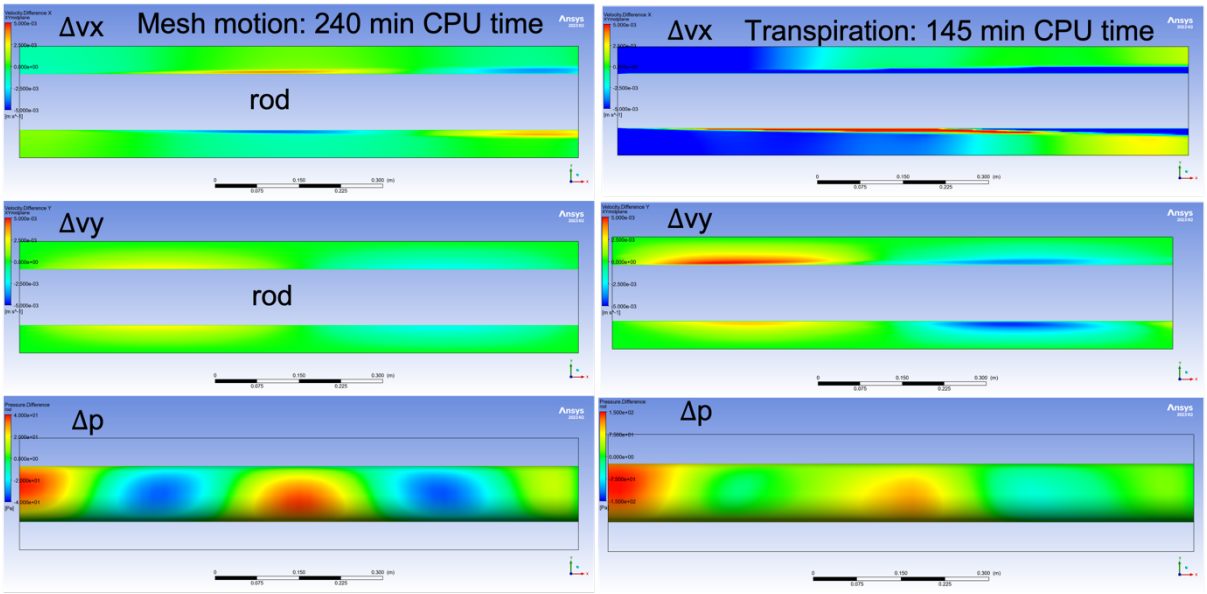

Figure 44: Comparing transpiration flux vs. mesh motion using no-slip wall condition

Using the transpiration flux compared to the full mesh motion for the case with no-slip wall, shows that the transpiration flux has difficulty representing the same effects as encountered with mesh motion by introducing a flux through the boundary. Since the walls have a no-slip condition, the assumption that the axial velocity component close to the wall can be set equal to the undisturbed inflow velocity may not be valid. As a consequence, the prediction of changes in velocity and pressure are not very reliable. However, the effect of not having to deform the mesh is also clearly visible as the simulation time reduced from 240 minutes with mesh motion, to about 145 minutes using transpiration flux.

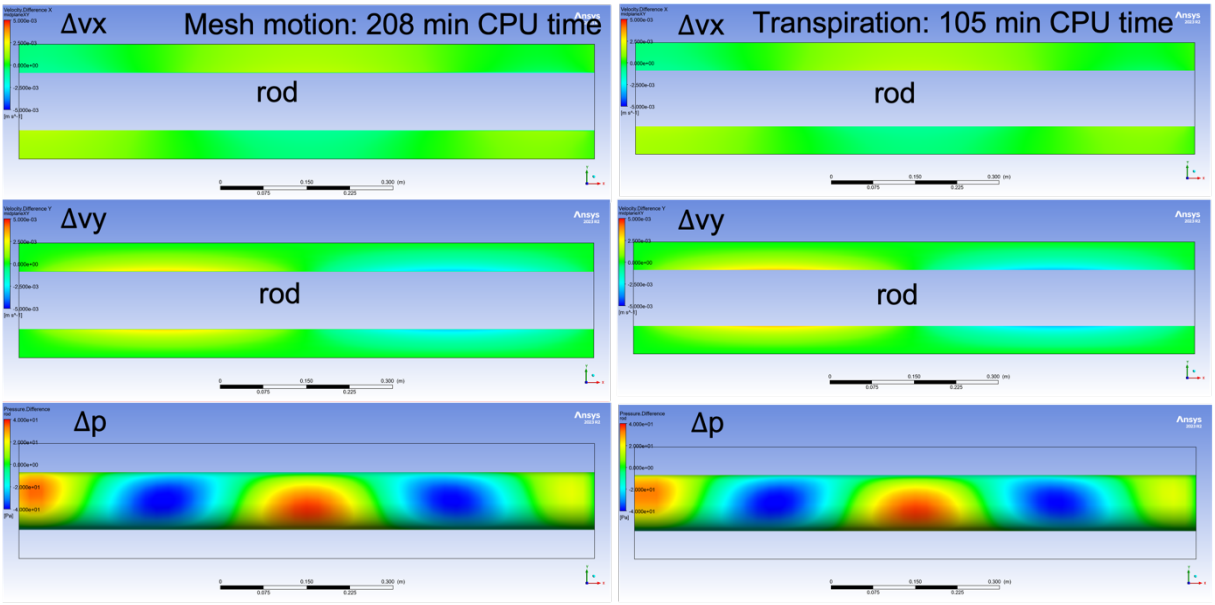

Figure 45: Comparing transpiration flux vs. mesh motion using slip wall condition

Using the transpiration flux compared to the full mesh motion for the case with slip wall, shows that the transpiration flux has almost identical results to the case with mesh motion. Both cases show also very similar effects on the wall pressure compared to the case with mesh motion and no-slip walls in the previous figure. The fact that no boundary layer needs to be resolved close to the rod already reduced the computational time from 240 minutes (mesh motion, no-slip walls) to 208 minutes (mesh motion, slip walls) and about halves the computational effort to 105 minutes for the case with transpiration flux and slip walls. Therefore, when perturbations in wall shear stresses are insignificant to the fluid response in pressure loads, using slip-walls and transpiration flux may be a viable, cost-effective alternative.

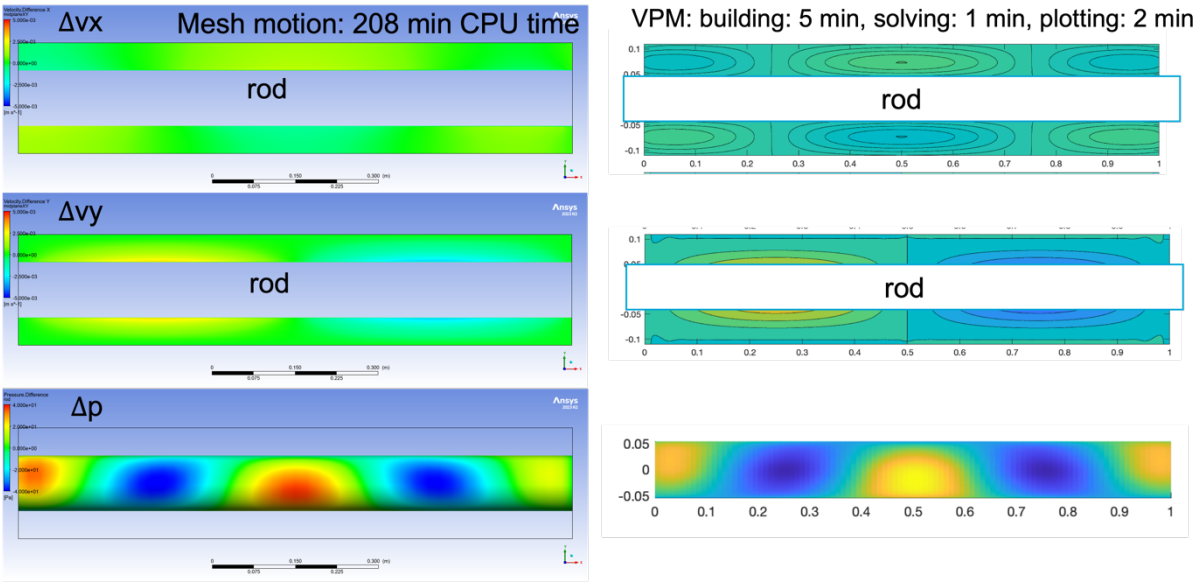

Figure 46: Comparing VPM vs. mesh motion using slip wall condition

The last alternative considered is using a VPM approach to simulate the fluid response to the imposed mode excitation. This method shows, at least qualitatively, very similar

patterns in the response compared to slip wall case with mesh motion. The computational work is with 8 minutes for a single run significantly faster than the CFD approach. The current VPM approach assumes a constant geometrical shape and uses the concept of transpiration flux to represent the motion of the rod. In the current implementation, a large portion of the work is building the system matrices and the LU-matrix decomposition to solve for the panel/particle strengths. Therefore, the building process is relatively expensive, taking 5 minutes to setup. The actual simulation of the time steps is only taking 1 minute, and creating the plots, for which the induced velocity and the pressure fields need to be reconstructed takes even longer with 2 minutes.

4.5.2 Fluid modal response model

The results shown in this section use the four mode shapes as shown in Figure 43. The kinematics of their excitation that is imposed is governed by the amplitude A_y and the time duration τ.

First, a reduced order model is constructed for the modal forcing by determining the coefficients $\hat{m}_{j,i}$, $\hat{d}_{j,i}$ and $\hat{k}_{j,i}$ from the modal response force $\bar{f}_{j,i}(t)$ (note that *i* represents the mode that is imposed and *j* the mode that is excited by the fluid response). Different values of A_y and τ are taken and it is investigated whether the response model that was obtained with one setting, can be used to predict the fluid response for another setting. Note that the kinematic function $g_\tau(t/\tau)$ in these first results is slightly different than the one reported in the methodology section: here the imposed motion is only an S-shape curve, of a 5-th order polynomial using the conditions $g_\tau(0) = \dot{g}_\tau(0) = \ddot{g}_\tau(0) = \dot{g}_\tau(1) = \ddot{g}_\tau(1) = 0$ and $g_\tau(1) = 1$. Although it does not satisfy the conditions to obtain the full flow field Δ-responses through the methodology described in the previous section, it does allow training the ROM for the modal forcing/response.

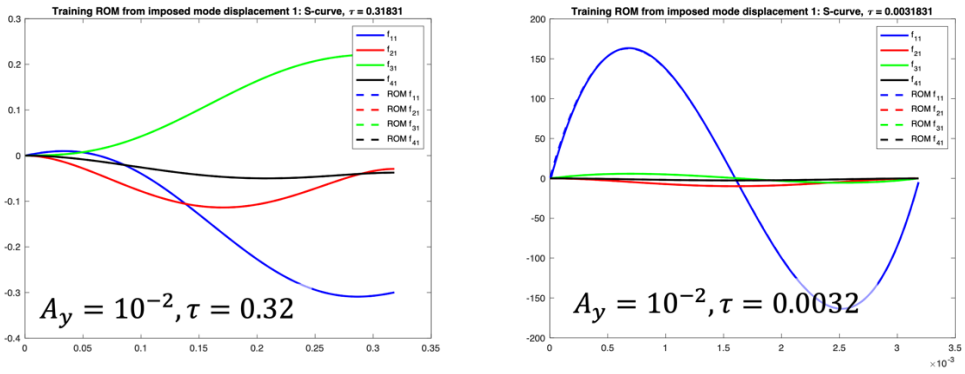

Figure 47: Constructing modal response ROM and testing on same dataset for forced excitation of mode 1

First the ROM (i.e. $\hat{M}, \hat{D}$ and $\hat{K}$) is constructed by fitting a curve that depends on the modal displacement, velocity and acceleration through the measured modal response. The constructed ROM is evaluated by plotting it's interpolated data together with the training data: the actual response and ROM results are almost undistinguishable, showing that the response can be well-captured in terms of added mass, damping and stiffness effects. As can be seen in the figure, for the forced excitation of mode 1, the fluid response and effect

on all 4 modes can be seen. For the larger value of τ (more quasi-steady kinematics), the response to mode 1 is strongest, but the fluid response also shows a strong coupling effect to mode 3. The smaller τ means stronger dynamics effects of velocity and in particular acceleration and the response to the excitation of mode 1 is very strong in mode 1 as well. The question remains how well the ROM would behave when trained for one τ and applied to another one.

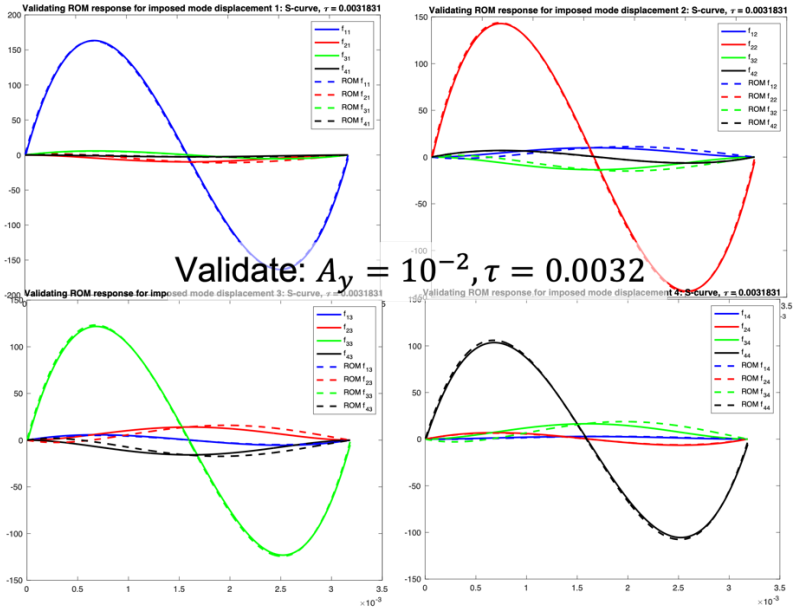

Figure 48: Validation of ROM trained for $\tau = 0.32$ and applied to data for $\tau = 0.0032$

When the ROM is obtained from the larger τ value, and applied to predict the response to an excitation with the smaller τ value, more differences between the ROM and the actual response can be observed, although the differences are not so large.

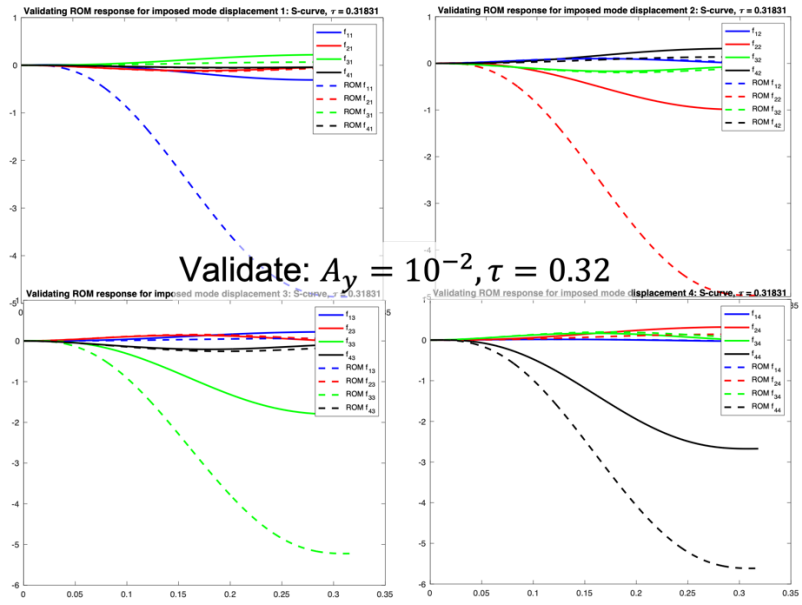

Figure 49: Validation of ROM trained for $\tau = 0.0032$ and applied to data for $\tau = 0.32$

When the ROM is trained with data from the smaller τ value and used to predict the response for the larger τ value, much larger discrepancies can be observed: the training data for the smaller τ is very much dominated by acceleration, especially compared to the displacement. This seems to lead to the "added stiffness" effects $\widehat{K}$ not to be presented very reliably and therefore the prediction is very much off, when these effects are more dominant. Therefore, we could use the data from the two different ROMs, i.e. use $\widehat{K}$ and $\widehat{D}$ from the ROM trained with more quasi-steady kinematics (a larger value of τ), and use $\widehat{M}$ from the ROM trained with more dynamic (acceleration dominated) kinematics (a smaller value of τ). Using this approach the ROM is performing well for a range of τ values.

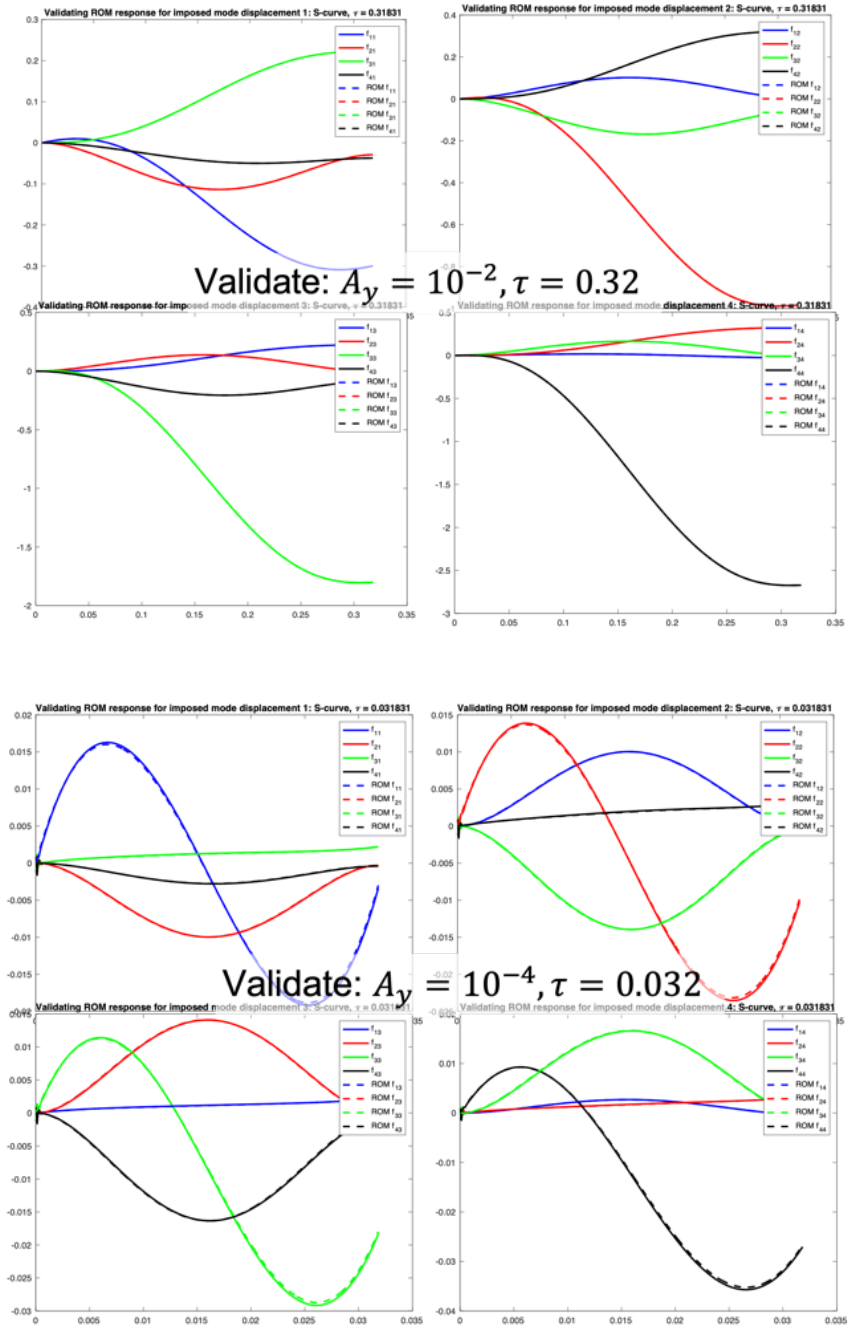

Figure 50: Validation of ROM ($\widehat{M}$ trained for $\tau = 0.0032$, $\widehat{K}$ and $\widehat{D}$ trained for $\tau = 0.32$)

The fluid response model seems to be well-capable of predicting the modal (coupling) in the presence of a vibrating structure. This would allow the ROM to be used together with the structural model to predict the coupled (FSI) dynamics of the mean flow. An analysis of the coupled system's response to e.g. turbulence fluctuations can then be conducted at a much lower cost compared to running actual coupled CFD-FEM simulations.

Finally, the pressure response fields for modes $i = 1 \ldots 4$ are shown in the following figures for the response to modal acceleration $\Delta\bar{p}_{M,i}(\vec{x})$, response to modal velocity $\Delta\bar{p}_{D,i}(\vec{x})$ and response to modal displacement $\Delta\bar{p}_{K,i}(\vec{x})$.

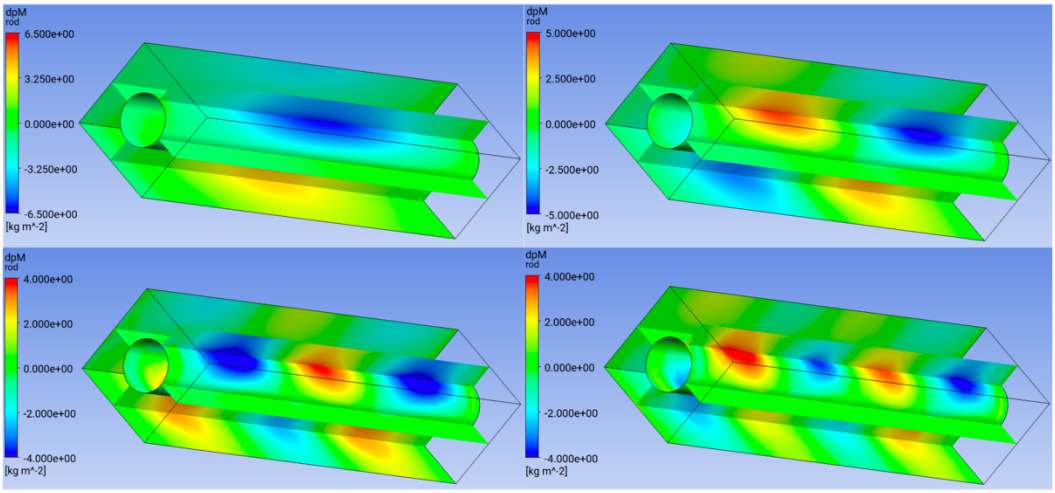

Figure 51: Pressure response to modal acceleration $\Delta\bar{p}_{M,i}(\vec{x})$

The pressure response due to acceleration $\Delta\bar{p}_{M,i}(\vec{x})$ can be interpreted as an added mass term: the mode shapes are clearly visible in the variation of the pressure. Since mode shape 1 has negative displacements (see Figure 43), a positive acceleration of the mode, means a negative displacement of the rod. This results in an increased pressure on the lower side of the rod and a reduced pressure on the upper side of the rod, resulting in an opposing force, similar to an inertial force.

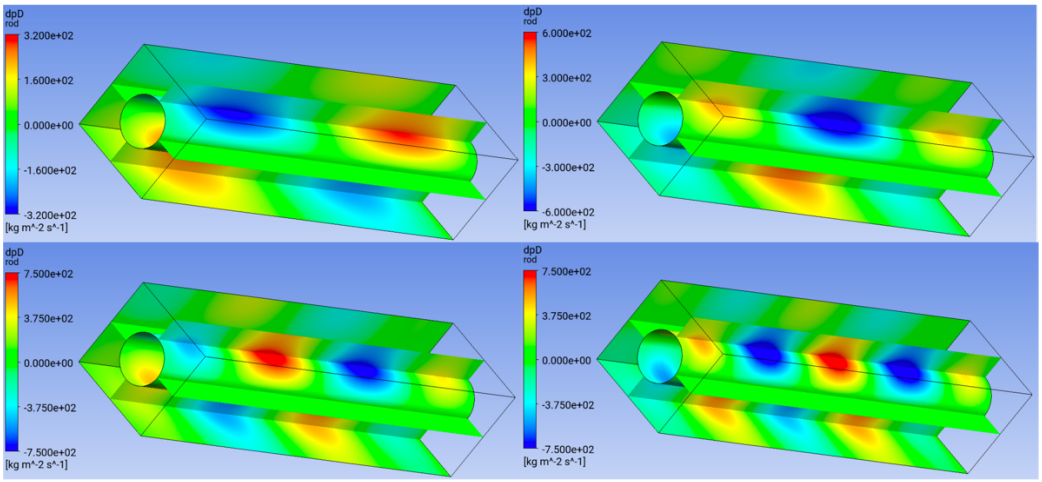

Figure 52: Pressure response to modal velocity $\Delta\bar{p}_{D,i}(\vec{x})$

The pattern of pressure response to modal velocity $\Delta\bar{p}_{D,i}(\vec{x})$ has a different pattern compared to the mode shape. Its largest effects are at the locations where the mode shape has its largest gradient. At these locations the rate of change in flow direction is directly related to the modal velocity and has the largest added damping contribution.

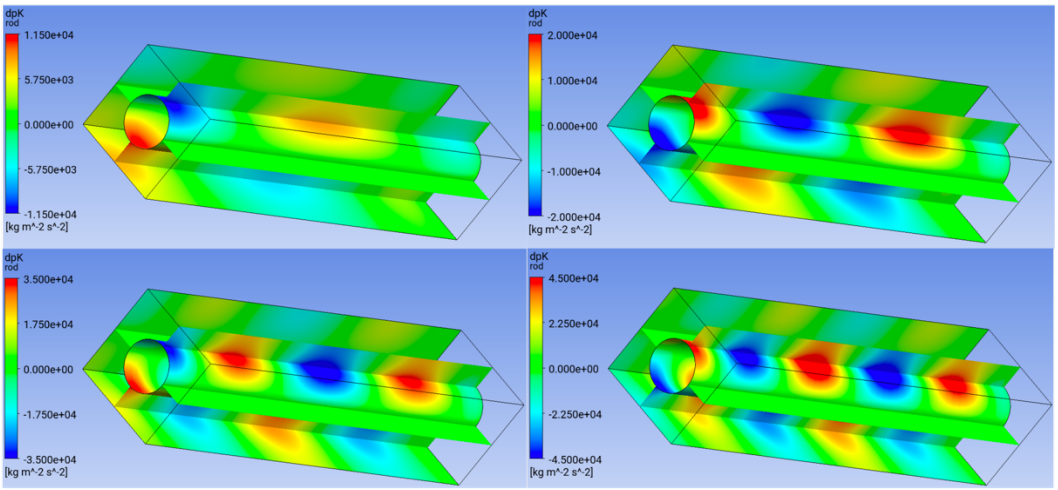

Figure 53: Pressure response to modal displacement $\Delta\bar{p}_{K,i}(\vec{x})$

Finally, the pressure response due to modal displacement $\Delta\bar{p}_{K,i}(\vec{x})$ shows a pattern close to the mode shape, but with a perturbation at the inlet. This may be due to the boundary conditions imposed at the inlet and outlet. The action of the pressure response for the first mode seems to suggest that the flow acts as a spring with a negative stiffness: when the modal displacement is positive, the rod deflects downwards and the pressure difference that is generated is amplifying this downward shift. This may result in a lower apparent stiffness of the structure, and with the higher apparent mass, a lower natural frequency for which resonance can occur.

Similar information can be constructed for the fluid response in its velocity field $\Delta\vec{\bar{u}}_i(\vec{x})$, or its turbulence quantities, e.g. $\Delta k_i(\vec{x})$. In a similar way, the fluid response on the side faces is known as well, which, for bundle simulations, would be interfaces between fluid domains. In a similar manner as finding the fluid response to a rod mode shape excitation, one could also define a basis that can represent the deformation of the fluid-fluid interface Γ_{ff}, and determine the fluid response for a perturbation in that interface mode. This leads to loads on the other interfaces and loads in the rod. Assuming linear perturbations, these can be added by superposition to obtain a reduced order model of a bundle system.

4.6 Conclusions and future work

A method to construct a reduced order fluid response model was presented. This model targets the application in axial flow configurations, in which turbulence induced vibration may be taken into account using a-priori LES/DNS simulations or experimental data of the spectrum, or alternatively, use a synthetic turbulence generator and pressure fluctuation model to obtain relevant pressure fluctuations based on the turbulence statistics obtained from e.g. a (U)RANS simulation. The model provides information about the fluid response in the whole fluid domain for any desired fluid quantity like pressure or velocity. Using a reduced set of modes, the data can be obtained by running a single simulation per mode

with forced modal kinematics. Apart from the fluid response field data, the direct action of the fluid onto the selected modes can also be determined as modal forcing. These lead to a ROM consisting of added mass, damping and stiffness matrices for the fluid of the size of the number of modes that is included in the analysis. It is proposed to use kinematics on a small time scale to train the ROM for added mass effects and use kinematics on a large time scale to train the ROM for added damping and stiffness effects. Preliminary tests show that this approach allows the fluid response model built for one set of kinematic coefficients is able to accurately predict the response for another set of kinematic coefficients.

Some additional computational effort may be saved by reducing the complexity of the modal excitation simulations. One could think of using slip wall boundary conditions in combination with a transpiration flux that would roughly half the simulation time due to the absence of the mesh deformation. Pressure responses are qualitatively and quantitatively in line with the no-slip wall, mesh deformation simulations.

For future work the focus will be on the validation of the methodology for a single (cantilever) rod case, and a further development of the methodology for bundle simulations.

Conclusion

In this work package, fast-running methods are identified that improve computational speed for such cases by reducing computational complexity. Each of the methods described in this report, aims to reduce the computational complexity by simplifying a specific part of the flow induced vibration problem. Two methods target in particular the effect of turbulence and turbulence pressure fluctuations: by introducing a synthetic turbulence model, the goal is to retrieve turbulence pressure fluctuations to similar accuracy as LES/DNS but at a much lower computational cost. Two other approaches use the decomposition of the structure dynamics into decoupled modes and rely on the use of these modes to build reduced order models for the structure or the fluid response within a coupled FSI simulation.

In Chapter 1, a new pressure fluctuation model, called AniPFM is described. This model allows for the prediction of pressure fluctuations when using a URANS approach, which can be useful in particular for turbulence-induced vibration prediction. Several aspects of the AniPFM were adjusted with respect to the previous PFM of Kottapalli et al., namely the energy spectrum cut-off filter, the replication of anisotropic Reynolds stresses, and the method for time correlation. AniPFM was validated for pure flow-only cases, comparing velocity and pressure fluctuations statistics with available experimental data. This was done for both a Homogeneous Isotropic Box and a Turbulence Channel flow. With satisfactory results found when comparing with reference experimental and numerical data, attention was switched to a first application to an FIV test case. The test case under consideration is that of a flexible brass beam in turbulent water, as performed by Chen & Wambsganss in 1975. Results for URANS FSI simulations showed a good match for the natural frequency with the experimental one, though an over-prediction in the damping ratio. This latter is in line with what was observed previously with the numerical framework used. Next, results for FSI simulations involving AniPFM were compared with experimental data and other numerical results. Differences in RMS amplitudes of about 30-40% were found, which is a significant improvement from the previous PFM.

Chapter 3 provides a brief description of the approaches used by IPP to calculate coupled vibrations in a simplified formulation. To generate turbulent pulsations, the synthetic turbulence procedure is used. The proposed procedure is simplified, since it is based on local parameters that take into account only the averaged flow history. In this case, the turbulent characteristics (correlations of velocity pulsations) are considered as isotropic. Despite significant simplifications compared to procedures that consider the transfer of pulsation characteristics, preliminary tests showed a good degree of agreement between the qualitative picture of the synthetic turbulence generator and the application of the SRS method, which is satisfactory for engineering practice. The pulsation component of pressure is calculated based on a simple algebraic relationship, where it is assumed that pressure pulsation is a dynamic consequence of velocity pulsation. In order to organize more efficient calculations, a one-parameter turbulence model of effective kinematic viscosity transfer was proposed, which is obtained by combining two k-ε RNG equations. To achieve this, it became necessary to express the kinetic energy of turbulence and its dissipation through eddy viscosity. These methods are promising fast methods for coupled FSI analysis.

Chapter 2 described the theory of the MOR approach, developed by ANSYS, which is based on the method of mode-superposition. Further, its implementation for a simplified FIV test case was described. The advantages of this method over the FOM follow from a comparative analysis. It showed increased efficiency of the ROM method against the original FOM: the wall-clock time of the fast-running method was approx. a factor of five smaller. The accuracy in terms of vibration frequency was perfect, while a small overestimation of the RMS amplitudes by the ROM was observed. It can be concluded that ANSYS MOR is a promising fast-running method that can provide comparable results to the ones generated with the FOM at a significantly lower computational cost.

In Chapter 4 a method to construct a reduced order fluid response model was presented. The model provides information about the fluid response in the whole fluid domain for any desired fluid quantity like pressure or velocity. Using a reduced set of modes (obtained from a structural mode decomposition), the data can be obtained by running a single simulation per mode with forced modal kinematics. Apart from the fluid response field data, the direct action of the fluid onto the selected modes can also be determined as modal forcing. These lead to a ROM consisting of added mass, damping and stiffness matrices for the fluid of the size of the number of modes that is included in the analysis. It is proposed to use kinematics on a small time scale to train the ROM for added mass effects and use kinematics on a large time scale to train the ROM for added damping and stiffness effects. Preliminary tests show that this approach allows the fluid response model built for one set of kinematic coefficients is able to accurately predict the response for another set of kinematic coefficients. Some additional computational effort may be saved by using slip wall boundary conditions in combination with a transpiration flux that would roughly half the simulation time due to the absence of the mesh deformation. Pressure responses are qualitatively and quantitatively in line with the no-slip wall, mesh deformation simulations.

Funded by
the European Union

Bibliography

1. S. Kottapalli, S. Sharma, A. Shams, A.H. Zuijlen, and M.J.B.M. Pourquie, "Numerical Simulation of Turbulence Induced Vibrations from URANS models using the Pressure Fluctuation Model.", NURETH-17, Xi'an, China (2017).
2. S. Kottapalli, A. Shams, A.H. van Zuijlen, M.J.B.M. Pourquie, "Numerical investigation of an advanced U-RANS based pressure fluctuation model to simulate non-linear vibrations of nuclear fuel rods due to turbulent parallel-flow," *Annals of Nuclear Energy*, **128** (2019).
3. M. Billson, L.-E. Eriksson and L. Davidson, "Jet Noise Modeling Using Synthetic Anisotropic Turbulence," in 10th AIAA/CEAS Aeroacoustics Conference, American Institute of Aeronautics and Astronautics (2004).
4. M. L. Shur, P. R. Spalart, M. K. Strelets and A. K. Travin, "Synthetic Turbulence Generators for RANS-LES Interfaces in Zonal Simulations of Aerodynamic and Aeroacoustic Problems," *Flow, Turbulence and Combustion*, **93**(5), pp. 63–92 (2014).
5. D. C. Wilcox, Turbulence modelling for CFD, DCW Industries (1993).
6. G. Alzetta, "The deal.II library, version 9.0". Journal of Numerical Mathematics (2018).
7. H.-J. Bungartz, et al. "preCICE – a fully parallel library for multi-physics surface coupling". *Computers and Fluids*, **141**, pp. 250–258 (2016).
8. J. Degroote, K. Bathe, and J. Vierendeels. "Performance of a new partitioned procedure versus a monolithic procedure in fluid-structure interaction", *Computers & Structures*, **87**(11), pp. 793–801 (2009).
9. S.C.G. Comte-Bellot, and S. Corrsin, "Simple Eulerian time correlation of full-and narrow-band velocity signals in grid-generated, 'isotropic' turbulence", J. Fluid Mech. 48, 273-337 (1971).
10. D.F.T. Gotoh, and D. Fukayama, "Pressure spectrum in homogeneous turbulence", Phys. Rev. Lett. 86, 3775-3778 (2000).
11. H.G. Weller, G. Tabor, H. Jasak, C. Fureby, "A tensorial approach to computational continuum mechanics using object-oriented techniques", Comput. Phys. 12, 6 (1998)
12. H. Abe, H. Kawamura, and Y. Matsuo. "Direct numerical simulation of a fully developed turbulent channel flow with respect to the Reynolds number dependence", J. Fluids Eng. 123, 382-393 (2001)
13. S.S. Chen and M. W. Wambsganss. "Parallel-flow-induced vibration of fuel rods", *Nuclear Engineering and Design*, **18**(2), pp. 253–278 (1972).
14. J. De Ridder, J. Degroote, K. Van Tichelen, P. Schuurmans, and J. Vierendeels, "Modal characteristics of a flexible cylinder in turbulent axial flow from numerical simulations", *Journal of Fluids and Structures*, **43**, pp. 110–123 (2013).
15. T. Nazari, A. Rabiee, and H. Kazeminejad, "Two-way fluid-structure interaction simulation for steady-state vibration of a slender rod using URANS and LES turbulence models", *Nuclear Engineering and Technology*, **51**(2), pp. 573–578 (2019).
16. J. Chouchoulis, "An advanced fluid-structure interaction software package for industrial problems in nuclear reactor applications", Master's thesis, TU Eindhoven (2018).
17. J. Einzinger and Ch. Frey, "Bi-directional fluid-structure interaction with model order reduction", ANSYS FSI training material (2014).
18. ANSYS CFX 2021R2 User's Manuals, ANSYS, 2021.
19. OECD/NEA, "Best practice guidelines for the use of CFD in nuclear reactor safety application - revision." NEA/CSNI/R(2014)11, (2015).

20. B.A.W. Smith and D.D. Derksen. "Measurement of steady and unsteady hydrodynamic loads on a nuclear fuel", *Journal of Fluids and Structures*, 12, pp. 475-489 (1998).

21. A. Mohany and M. Hassan. "Modelling of fuel bundle vibration and the associated fretting wear in a CANDU fuel channel", *Nuclear Engineering and Design*, 9, pp.1-9 (2012).

22. R.Violette, E.de Langre and G.E. Karniadakis. "Computation of vortex-induced vibrations of long structures using a wake oscillator model: Comparison with DNS and experiments", Computers & Structures, 11, pp.1134-1141 (2007).

23. Xuan Zhang. "Numerical and experimental investigations on vibration of simulated CANDU fuel bundles subjected to turbulent fluid flow", Thesis of a candidate of technical sciences, Toronto, pp.1-123 (2011).

24. F.R. Menter. Best Practice: Scale-Resolving Simulations in ANSYS CFD Version 2.00 (2015).

25. R. Rogallo. "Numerical experiments in homogeneous turbulence", Tech. rep.:NASA (1981).

26. A.S Kozelkov, V.V. Kurulin, E.S. Tjatjushkina et al. "RANS-LES zonal approach based on an algebraic model of Reynolds stresses", *The All-Russian Scientific Research Institute of Experimental Physics (VNIIEF)*, Sarov, Russia (2017). (In Russian)

27. P. Nee and L.S.G. Kovasznay. "Simple phenomenological theory of turbulent shear flow", Phys. Fluids, 12(3), pp. 473-484 (1969).

28. P.R. Sparalt and S.R. Allmaras. "A one-equation turbulence model for aerodynamic flows", AIAA, Paper 92-4039, p.16 (1992).

29. P.R. Sparalt and S.R. Allmaras. "A one-equation turbulence model for aerodynamic flows", La recherche aerospatiate, 1, p. 5-21 (1994).

30. A.A. Avramenko, B.I. Basok and A.V Kuznecov. "Theoretical one-parameter model of turbulent viscosity and thermal diffusivity", Industrial Heat Engineering, 26(5), pp.10-13 (2004). (In Russian)

31. A.A. Avramenko, B.I. Basok et al. "Renormalization group analysis of turbulence", National Academy of Sciences of Ukraine, p.300 (2013). (In Russian)

32. R.H. Kraichnan. "Inertial-range transfer in two- and three-dimensional turbulence", J. Fluid Mech., 57(3), pp. 525-535 (1971).

33. D.C. Leslie. "Developments in the theory of turbulence", Oxford: Clarendon Press, p.380 (1973).

34. S.H. Lam. "On the RNG theory of turbulence", Phys. Fluids A., 4(5), pp. 1007-1017 (1992)

35. V.M. Canuto and M.S. Dubovikov. "A new approach to turbulence", Int. J. Modern Phys., 12(18), pp. 3121-3152 (1997).

36. P. Batten, U. Goldberg and S. Chakravarthy. "Interfacing Statistical Turbulence Closures with Large-Eddy Simulation", *AIAA Journal*, 42(3), pp. 485–492 (2004)

37. N. Jarrin, R. Prosser, J. Uribe et al. "Reconstruction of turbulent fluctuations for hybrid RANS/LES simulations using a Synthetic-Eddy Method", International Journal of Heat and Fluid Flow, 30(3), pp. 435–442 (2009).

38. M. S. Grickevich. "Calculation of turbulent near-wall flows using the zonal RANS-LES approach with a volumetric source of turbulent pulsations", Thesis of a candidate of physical and mathematical sciences, Saint-Petersburg, pp.1-120 (2014). (In Russian)

39. I. Hince. "Turbulence", *State Publishing House of Physico-Mathematical Literature*, Moscow, pp.1-680 (1963). (In Russian)

40. A. V. Garbaruk, M. H. Strelec and M. L. Shur. "Turbulence modeling in complex flow simulations", Publishing House of the Polytechnic University, Saint-Petersburg, pp.1-88 (2012). (In Russian)

41. D. Ju. Adam'jan. "Method for generating synthetic turbulence at inlet boundaries for calculating turbulent flows within the framework of eddy-resolving approaches", Thesis of a candidate of physical and mathematical sciences, Saint-Petersburg, pp.1-142 (2011). (In Russian)

42. V. V. Perevezencev. "Random hydrodynamic loads, vibrations and damping of oscillations of fuel rod bundles of VVER reactor fuel assemblies in a turbulent coolant flow", Abstract of a thesis for the degree of Doctor of Technical Sciences, Moscow, pp.1-33 (2012). (In Russian)

43. R. Kraichnan. "Diffusion by a random velocity field", *Physics of Fluids*, 13(1), pp. 22–31 (1970).

44. Hirokazu Sugiura, Shigeyuki Watanabe and Akihisa Iwasaki. "Development of structural integrity assessment method for flow -induced vibration of reactor internals in PWR", Pressure Vessels & Piping Conference (2018).